Localised general vertical coordinates for quasi-Eulerian ocean models: the Nordic overflows test-case

Diego Bruciaferri[1], Catherine Guiavarc'h[2], Helene Theresa Hewitt[2], James Harle[3], Mattia Almansi[4], and Pierre Mathiot[5]

[1]Met Office Hadley Centre
[2]Met Office
[3]National Oceanography Centre, Southampton
[4]National Oceanography Centre
[5]Univ. Grenoble Alpes/CNRS/IRD/G-INP, Institut des Geosciences de l'Environnement

June 25, 2023

Abstract

A generalised methodology to deploy different types of vertical coordinate systems in arbitrarily defined time-invariant local areas of quasi-Eulerian numerical ocean models is presented. After detailing its characteristics, we show how the novel localisation method can be used to improve the representation of the Nordic Seas overflows in the UK Met Office NEMO-based eddy-permitting global ocean configuration. Three z*-levels with partial steps models localising different types of terrain-following vertical coordinates in the proximity of the Greenland-Scotland ridge are developed and compared against a control. Experiments include a series of idealised and realistic numerical simulations where the skill of the models in computing pressure forces, reducing spurious diapycnal mixing and reproducing observed properties of the Nordic Seas overflows are assessed. Numerical results prove that the localisation approach proposed here can be successfully used to embed terrain-following levels in a global geopotential levels-based configuration, provided that the localised vertical coordinate chosen is flexible enough to allow a smooth transition between the two. In addition, our experiments show that deploying localised terrain-following coordinates via the multi-envelope method allows the crucial reduction of spurious cross-isopycnal mixing when modelling bottom intensified buoyancy driven currents, significantly improving the realism of the Nordic Seas overflows simulations in comparison to the other models. Important hydrographic biases are found to similarly affect all the realistic experiments and a discussion on how their interaction with the type of localised vertical coordinate affects the accuracy of the simulated overflows is provided.

Localised general vertical coordinates for quasi-Eulerian ocean models: the Nordic overflows test-case

Diego Bruciaferri[1], Catherine Guiavarc'h[1], Helene T. Hewitt[1], James Harle[2], Mattia Almansi[2*], Pierre Mathiot[3]

[1]Met Office Hadley Center, Exeter, UK
[2]National Oceanography Centre, Southampton, UK
[3]Université Grenoble Alpes, CNRS, IRD, Grenoble INP, Grenoble, France

Key Points:

- A generalised methodology to embed distinct types of vertical coordinates in local time-invariant targeted areas of quasi-Eulerian ocean models
- Three different types of terrain-following coordinates are localised in the Nordic overflows region of a geopotential-levels based global model
- Local multi-envelope terrain-following levels reduce spurious diapycnal mixing and improve the accuracy of the simulated Nordic overflows

*now at B-Open Solutions srl, Rome, Italy

Corresponding author: Diego Bruciaferri, `diego.bruciaferri@metoffice.gov.uk`

Abstract

A generalised methodology to deploy different types of vertical coordinate system in arbitrarily defined time-invariant local areas of quasi-Eulerian numerical ocean models is presented. After detailing its characteristics, we show how the novel *localisation* method can be used to improve the representation of the Nordic Seas overflows in the UK Met Office NEMO-based eddy-permitting global ocean configuration. Three z*-levels with partial steps models localising different types of terrain-following vertical coordinates in the proximity of the Greenland-Scotland ridge are developed and compared against a control. Experiments include a series of idealised and realistic numerical simulations where the skill of the models in computing pressure forces, reducing spurious diapycnal mixing and reproducing observed properties of the Nordic Seas overflows are assessed. Numerical results prove that the localisation approach proposed here can be successfully used to embed terrain-following levels in a global geopotential levels-based configuration, provided that the localised vertical coordinate chosen is flexible enough to allow a smooth transition between the two. In addition, our experiments show that deploying localised terrain-following coordinates via the multi-envelope method allows the crucial reduction of spurious cross-isopycnal mixing when modelling bottom intensified buoyancy driven currents, significantly improving the realism of the Nordic Seas overflows simulations in comparison to the other models. Important hydrographic biases are found to similarly affect all the realistic experiments and a discussion on how their interaction with the type of localised vertical coordinate affects the accuracy of the simulated overflows is provided.

Plain Language Summary

Numerical ocean models are arguably one of the most advanced tools the scientific community can use to study the role of the worlds oceans. However, the ability of an ocean model to realistically simulate ocean currents depends on some of the numerical techniques it employs. One such example concerns the type of vertical coordinate system employed. Ocean models usually implement a single type of vertical coordinate throughout the entire model domain, which is typically unable to accurately represent the vast variety of physical processes driving the oceans. In this study, we propose a new method that allows different types of vertical coordinates in selected regions of the same model domain. Our method targets a particular class of ocean models (known as quasi-Eulerian), improving the way they represent the important influence the sea floor exerts on ocean currents. After introducing our novel approach, we present the results of a series of numerical experiments where we test its skill for improving the representation of the Nordic Seas overflows, an important type of ocean current located at depth in the proximity of the Greenland-Scotland ridge.

1 Introduction

The governing equations of modern numerical ocean models are typically formulated in terms of a generalised vertical coordinate (GVC) $s = s(x, y, z, t)$ (e.g., Bleck (2002); Adcroft & Campin (2004); Shchepetkin & McWilliams (2005); Leclair & Madec (2011); Griffies (2012); Petersen et al. (2015); Adcroft et al. (2019)), where the only constraint for s is to be a strictly monotone function of the depth z (e.g., Kasahara (1974); Griffies (2004)). In general, GVCs usually employed in numerical ocean models can be divided in three main groups, depending on the type of the time-stepping algorithm used to solve the oceanic equations (e.g., Adcroft & Hallberg (2006); Leclair & Madec (2011); Griffies et al. (2020)): quasi-Eulerian (QE; e.g., Kasahara (1974)), quasi-Lagrangian (QL; e.g., Bleck (2002)) and Arbitrary Lagrangian Eulerian (ALE; e.g., Hirt et al. (1974)) coordinates.

QE coordinates 'breath' with the barotropic motion of the ocean and diagnose the vertical advective velocities from mass continuity. Examples of this type of GVCs are the rescaled geopotential z^*-coordinate (Stacey et al. (1995); Adcroft & Campin (2004)), the various flavours of terrain-following σ-coordinates (e.g., Phillips (1957); Song & Haidvogel (1994); Shchepetkin & McWilliams (2005)) and subsequent hybridisation of these two ($z^*-\sigma$ coordinates; e.g., Dukhovskoy et al. (2009); Bruciaferri et al. (2018); Wise et al. (2021)).

The second type of GVCs are the QL coordinates; they take advantage of vertical Lagrangian-remap methods to evolve with the flow whilst retaining a grid able to provide an accurate representation of the ocean state, as in modern isopycnal models (e.g., Bleck (2002); Adcroft et al. (2019)).

Lastly, and providing the most general framework, are the ALE coordinates, such as the $\tilde{z}$-coordinate proposed by Leclair & Madec (2011) and Petersen et al. (2015) or the adaptive terrain-following γ-coordinates of Hofmeister et al. (2010). This class of GVCs employs vertical ALE methods to modify the computational grid in time with a motion that typically does not strictly mimic the oceanic flow (i.e., in a Lagrangian sense), but can follow any prescribed algorithm.

In the continuous limit, oceanic equations formulated in different GVCs are of course completely equivalent. However, numerical discretisation can introduce errors specific to the type of GVC employed that can seriously undermine the ability of a numerical model to accurately represent some aspects of the oceanic dynamics, especially on climatic scales (e.g., Haidvogel & Beckmann (1999); Griffies, Böning, et al. (2000)). One such example is the inevitable truncation errors that arise the tracer advection schemes, causing substantial spurious diapycnal mixing in the ocean interior of QE models. This leads to a modification of water masses and potentially significant climatic model drifts (Griffies, Böning, et al., 2000; Griffies, Pacanowski, & Hallberg, 2000). It has been demonstrated that the same type of numerical mixing can be greatly reduced when using QL or ALE vertical coordinates (e.g., Adcroft et al. (2019); Megann et al. (2022)).

The choice of GVC also dictates the way an ocean model resolves the bottom topography, hence affecting its ability to simulate the critical interactions between flow and topography. In the case of QE geopotential coordinates, the step-like nature of the sea floor in the ocean model can compromise the accuracy of the simulated large scale ocean dynamics (e.g., Penduff et al. (2007); Ezer (2016)). In addition, it also has the potential to introduce significant spurious mixing when simulating gravity current flows (e.g., Winton et al. (1998); Legg et al. (2006, 2009); Colombo et al. (2020)). With an improved representation of the sea floor, as in the case of QE terrain-following coordinates, flow-topography interactions are more naturally simulated and such deficiencies can be substantially reduced (e.g., Willebrand et al. (2001); Käse (2003); Ezer (2005, 2016); Schoonover et al. (2016)). However, employing QE terrain-following coordinates in regions of steep topography can introduce significant errors in the computation of horizontal pressure forces, making their use in global configurations challenging (e.g., Lemarié et al. (2012)). The use of isopycnal coordinates has been proven to be effective in reducing spurious mixing in idealised (Legg et al., 2006) and realistic simulations of the Nordic Seas overflows (Megann et al., 2010; Wang et al., 2015; Guo et al., 2016). However, such models suffer from the outcropping of coordinate interfaces in weakly stratified regions and detrainment from a mixed layer into the ocean interior (e.g., Megann et al. (2022)).

Ocean models typically implement one single type of vertical coordinate throughout the model domain. However, it is evident that a perfect vertical coordinate suitable for *any* oceanic regime does not exist and a hybrid approach, combining the best features of each vertical coordinate system within a single framework, is currently an active area of research. In one such example, Bleck (2002, HYCOM) and subsequently Adcroft et al. (2019, MOM6) tried to alleviate some of the drawbacks of isopycnal models using a QL hybrid isopycnal-z^* vertical coordinate. Adcroft et al. (2019) reports that issues still remain with the dense high latitude overflows and concludes that more research is needed to determine a robust vertical grid algorithm suitable for the World Ocean. On paper, generalised ALE coordinates appear to be the most attractive framework for evolving in time the vertical grid according to a *dynamical* algorithm that seeks the optimal coordinate configuration for the various oceanic regimes of the model domain. However, the practical realisation of such an *optimal* ALE is non-trivial, and active research is currently on-going (e.g., Hofmeister et al. (2010); Gibson (2019)).

To better represent some features of the ocean dynamics such as flow-topography interactions, an algorithm that defines time-invariant target areas of the model domain where the vertical grid smoothly transitions into another more appropriate GVC may be sufficient. This was the concept behind the local-sigma vertical coordinate of Colombo (2018): to improve the representation of Nordic Seas overflows in a global model, terrain-following coordinates were employed only in the proximity of the Greenland-Scotland ridge, whilst standard z^*-coordinates with partial steps were used everywhere else. However, the development of such a mesh is non-trivial, especially when defining the transition zone between the two vertical coordinates. Consequently, their approach resulted in an ad hoc methodology not easily generalizable and applicable to different scenarios.

Building on the study of Colombo (2018), the aim of this paper is to (i) introduce a general methodology that enables QE numerical ocean models to localise (i.e., embed) various GVCs configurations within a model domain and (ii) assess the ability of the new method to improve the representation of the Nordic Seas overflows in eddy-permitting global ocean simulations. Two different types of numerical experiments are conducted in this study. At first, a series of idealised numerical experiments is carried out to test the accuracy of localised GVCs in computing horizontal pressure forces and reproducing gravity currents. After, realistic global simulations are run to test the skill of the localised vertical coordinates in reproducing observed properties of the Nordic Seas overflows when compared with the traditional approach of employing z^*-coordinates with partial steps.

The Nordic Seas overflows consist of dense cold waters formed in the Nordic Seas and the Arctic Ocean and flowing south via the Greenland-Scotland ridge in the form of strong gravity currents that form the lower limb of the Atlantic Meridional Overturning Circulation (AMOC; e.g. Dickson & Brown (1994); Johnson et al. (2019); Østerhus et al. (2019)). Several physical processes combine to generate such dense water masses, including i) open ocean convection in the Greenland sea, ii) cascading from the Arctic shelves and iii) transformation of North Atlantic Water (NAW) recirculating within a cyclonic boundary current along the Icelandic basin and the Irminger Sea topography (e.g. Hansen & Østerhus (2000)).

The Nordic Seas overflows include the Denmark Strait Overflow Water (DSOW) and the Iceland-Scotland Overflow Water (ISOW). The DSOW flows south via the Denmark Strait (see Fig. 1), cascading along the continental slope of the western Irminger Sea (Dickson & Brown, 1994). While descending, the DSOW entrains and mixes with the ambient water encountered along its path, resulting in an approximately doubled transport within a few hundred kilometres downstream of the Denmark Strait sill (Dickson et al., 2008). In the proximity of Cape Farewell, the DSOW turns westward and enters the Labrador Sea as the densest part of the Deep Western Boundary Current (DWBC) (e.g. Hopkins et al. (2019)).

The path of the ISOW is more complex (see also Fig. 1 for the locations). It crosses the Greenland-Scotland ridge primarily via the Faroe-Shetland channel and the Faroe-Bank channel, although secondary contributions via the Wyville Thomson ridge and the Iceland-Faroe ridge are also important (Østerhus et al., 2019). Once the main branch has passed the Faroe-Bank channel, the ISOW descends along the Iceland-Faroe slope, mixing with waters spilling from the Iceland-Faroe ridge. After, the ISOW proceeds southwestward into the Icelandic basin, flowing along the eastern flank of the Reykjanes ridge and mixing with the surrounding ambient fluid. While early observational studies indicated a reduced importance of mixing and dilution in comparison to the DSOW (Saun-

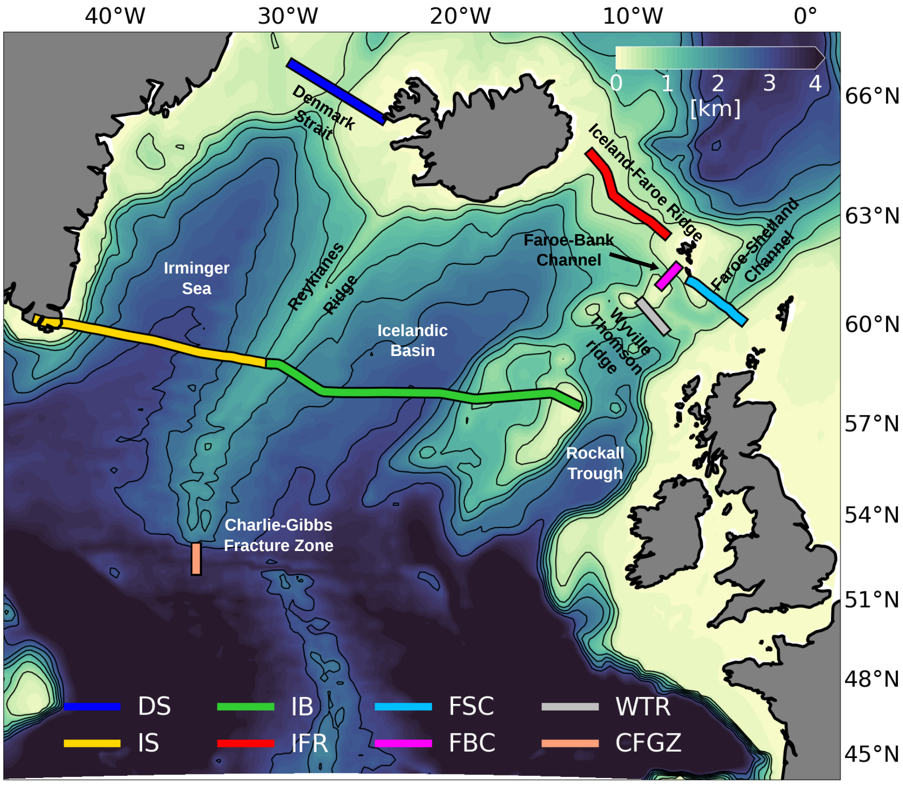

Figure 1. Bathymetry of the Nordic overflows region at 1/4° of resolution showing the location of the main geographical features of the area and the position of the observational cross-sections analysed in the realistic experiments - see Sec. 5 and Tab. 1 for the details. The thin black lines are selected isobaths ranging from 500 m to 3000 m with a discretisation step of 500 m.

ders, 1996), recent estimates appear to suggest that entrainment contributes in doubling the ISOW transport (Johns et al., 2021). The modified ISOW leaves the Icelandic basin through multiple pathways (e.g., Hopkins et al. (2019); S. M. Lozier et al. (2022)): on the one side, the dense water descending the Icelandic basin directly flows into the Irminger Sea via various gaps in the Reykjanes ridge; on the other side, after flowing through the Charlie-Gibbs Fracture Zone, the modified ISOW either continues westward spreading towards the Labrador Sea or enters the Irminger sea as a deep boundary current that flows cyclonically around the continental slope of the Irminger basin and rides above the DSOW to form the lightest part of the DWBC.

The manuscript is organised as follows. Section 2 describes the details of the localisation method proposed in this study. Section 3 introduces the Nordic overflows test-case, describing the global ocean model used in our integrations and the three localised QE vertical coordinates developed and tested in our experiments. Sections 4 and 5 describe and discuss the set-up and the results of the idealised and realistic numerical experiments conducted in this work, respectively. Finally, Sec. 6 summarise our conclusion and discuss future perspectives. For the reader convenience, a list of the acronyms used in this paper is given in Appendix D.

2 Localised quasi-Eulerian vertical coordinates

The intent of developing localised GVCs is to provide ocean models with the capability of arbitrarily varying the vertical coordinate system in targeted areas of the model domain. Although the broad idea of changing/adapting the vertical grid within an ocean model is not new (e.g., Beckers et al. (2002); Colombo (2018); Adcroft et al. (2019)), the approach proposed here combines three specific attractive features:

1) it uses a generalised, simple and fully reproducible algorithm to define time-invariant limited areas of the model domain where local-GVCs will be employed;
2) it allows one to have full control on the definition of the areas where local-GVCs will be employed as well as on the final set-up of the vertical grid;
3) it is simple and efficient, allowing for minimal modifications to the original code of an oceanic model;

Some of these properties follow from the fact that the method introduced here targets QE GVCs, exploiting some key features of this specific class of vertical coordinates. In the next two sections, first the QE approach is summarised (Sec. 2.1) and after the details of the localisation algorithm are described (Sec. 2.2).

2.1 The quasi-Eulerian approach to vertical coordinates

The QE approach applies to any GVCs where the vertical coordinate transformation can be expressed as a direct function of the ocean free-surface $\eta(x, y, t)$. The evolution in time of QE coordinate interfaces is importantly controlled by the prognostic thickness equation. In the case of an incompressible Boussinesq ocean, the continuous thickness equation can be written in terms of a GVC $s = s(x, y, z, t)$ and in conservation form as (e.g., Bleck (1978); Burchard et al. (1997); Griffies et al. (2020))

$$\frac{\partial h}{\partial t} + \nabla_s \cdot (h\,\mathbf{u}) + \frac{\partial w}{\partial s} = 0, \tag{1}$$

where $h(x, y, s, t) = \partial_s z$ is the Jacobian of the coordinate transformation, $\nabla_s = (\partial_x|_s, \partial_y|_s, 0)$ is the lateral gradient operator acting along surfaces of constant s, $\mathbf{u}(x, y, s, t)$ is the horizontal flow vector and $w(x, y, s, t) = h\,D_t s$ is the dia-surface velocity (with D_t the material time derivative operator; see Griffies (2004) for the details).

When moving to a discrete level, the transformed vertical domain can be divided into N layers $k = 1, ..., N$, so that the k^{th} generic model layer is bounded by generalised coordinate interfaces $s_{k+\frac{1}{2}}$ at the top and $s_{k-\frac{1}{2}}$ at the bottom, respectively. In such a framework, the thickness $h_k(x, y, t)$ of the discrete layer k is given by

$$h_k = \int_{s_{k-\frac{1}{2}}}^{s_{k+\frac{1}{2}}} h(x, y, s, t)\,ds = z_{k+\frac{1}{2}} - z_{k-\frac{1}{2}}, \tag{2}$$

where $z_{k\pm\frac{1}{2}}(x, y, t) = z\Big(x, y, s_{k\pm\frac{1}{2}}, t\Big)$ and $z_{k+\frac{1}{2}} > z_{k-\frac{1}{2}}$. This definition ensures that $\int_{s(z=-H)}^{s(z=\eta)} h\,ds = \sum_{k=1}^{N} h_k = H + \eta$, with $H(x, y)$ the ocean bottom topography and $z_{\frac{1}{2}} = -H(x, y)$ at the bottom boundary and $z_{N+\frac{1}{2}} = \eta(x, y)$ at the free surface. Consequently, the layer integrated thickness equation reads

$$\frac{\partial h_k}{\partial t} + \nabla_s \cdot (h_k\,\mathbf{u}_k) + w_{k+\frac{1}{2}} - w_{k-\frac{1}{2}} = 0, \tag{3}$$

where $\mathbf{u}_k(x, y, t) = h_k^{-1} \int_{s_{k-\frac{1}{2}}}^{s_{k+\frac{1}{2}}} h\mathbf{u}\, ds$ is the layer averaged horizontal flow vector and $w_{k\pm\frac{1}{2}}(x, y, t) = w\Big(x, y, s_{k\pm\frac{1}{2}}, t\Big)$.

The QE algorithm includes two steps to integrate equation 3. At first, the thickness tendency is deduced from a prescribed functional relationship of the type $\partial_t h_k \propto \partial_t \eta$, sometimes referred to as the *coordinate equation* (e.g., Leclair & Madec (2011)) since it completely depends on the analytical formulation of the coordinate transformation. Subsequently, once $\partial_t h_k$ is known, the thickness equation 3 is used to diagnose the dia-surface velocity w.

Introducing a time-invariant model layer thickness $h_k^0(x, y)$ defined for an unperturbed ocean at rest (i.e., when $\eta = 0$) allows one to express the layer thickness as

$$h_k = h_k^0 + \alpha_k \eta, \tag{4}$$

where $0 \leq \alpha_k \leq 1$ represents the fraction of $\eta(x, y, t)$ assigned to each $h_k(x, y, t)$. While in general this parameter depends on the type of QE vertical coordinate employed, a useful and attractive approach is to develop numerical ocean model code that implements vertical coordinate transformations sharing the same formulation for α_k. In such a way, QE ocean models can be equipped with a general and relatively simple dynamical core that can be used consistently with different types of QE GVCs. This latter property is particularly useful for the localisation method proposed in this paper, as will be explained in the next section.

Modern ocean models typically use an α_k function of $h_k^0\, H^{-1}$ (e.g., Adcroft & Campin (2004); Shchepetkin & McWilliams (2005); Leclair & Madec (2011); Petersen et al. (2015)), resulting in a QE coordinate equation written as

$$\frac{\partial h_k}{\partial t} = \frac{h_k^0}{H}\frac{\partial \eta}{\partial t} = -\frac{h_k^0}{H}\nabla_s \cdot \int_{s(z=-H)}^{s(z=\eta)} h\,\mathbf{u}\, ds = -\frac{h_k^0}{H}\nabla_s \cdot \sum_{m=1}^{N} h_m\,\mathbf{u}_m, \tag{5}$$

where the free-surface equation (neglecting fresh water sources for simplicity) is used to obtain the second equation.

2.2 The localisation algorithm

The localisation method proposed in this paper permits one to embed distinct *local* QE vertical coordinates in different targeted areas of the same model domain Ω, which otherwise employs the *global* Ω^V QE coordinate system. Figure 2 presents an explanatory sketch for the case of two local areas, although there are no restrictions on the total number P of local areas that can be implemented. Here, the red regions Λ_1 and Λ_2 are two *localisation* areas where the model uses Λ_1^V and Λ_2^V QE coordinates, respectively. In addition, the green areas T_1 and T_2 represent *transition* zones where T_1^V and T_2^V vertical coordinates result from a smooth relaxation of the local Λ_1^V and Λ_2^V towards the global Ω^V.

While it is desirable to have complete freedom in choosing the localisation areas, it is preferable to apply a generalised algorithm to define the transition areas. For this work we propose a simple method as described in Appendix A.

Once the transition regions have been identified, the following function is used in this study to compute the relaxation weights in the generic transition area T_p (where $1 \leq p \leq P$):

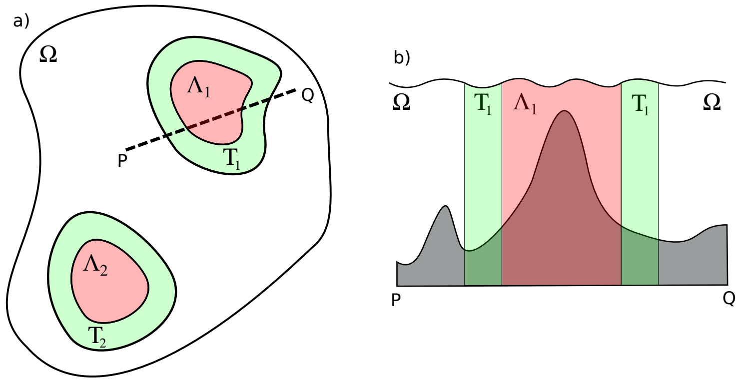

Figure 2. Explanatory sketch of the QE localisation method for the case of two localisation areas - a) is a planar view while b) is a vertical cross-section through line PQ. In the white area Ω the model employs the *global* Ω^V QE GVC, while in the two red regions Λ_1 and Λ_2 the *localised* Λ_1^V and Λ_2^V QE coordinates are used. In the green *transition* zones T_1 and T_2 the vertical coordinates T_1^V and T_2^V are computed via equation 7.

$$w_p = \frac{1}{2} + \tanh\left(a\frac{D_p - d_p}{D_p + d_p}\right)\Big[2\tanh(a)\Big]^{-1}. \tag{6}$$

Here, $a = 1.7$ is a tunable coefficient while D_p and d_p are the minimum Euclidean distances of a particular point of the transition zone T_p from its outer and inner boundaries, respectively. Finally, the thickness $h_{k,p}$ of a particular model grid cell included in the area T_p is computed as

$$h_{k,p} = w_p h_{k,\Omega} + (1 - w_p) h_{k,\Lambda_p}, \tag{7}$$

where $h_{k,\Omega}$ and h_{k,Λ_p} are the model cell thicknesses consistent with Ω^V or Λ_p^V GVCs, respectively.

Equation 4 allows QE ocean models to compute h_k in terms of h_k^0, α_k and η. Typically, the calculation of h_k^0 is conducted at the very beginning of a model simulation, either as an 'off-line' pre-processing step or as a single call in the model code just before the beginning of the time-marching stage. Therefore, if Ω^V and Λ_p^V GVCs use a consistent definition for α_k, the QE localisation algorithm can be introduced with minimal changes to the h_k^0 calculation step and no further modifications to the hydrodynamical core of a QE ocean model. In particular, this means that equation 7 can be used only at the beginning of the simulation to compute $h_{k,p}^0$. This is particularly convenient since it permits one to detect any vertical grid set-up issue at a very early stage, saving time in the development and implementation process.

3 The Nordic overflows test-case

In this section, the details of the QE global ocean model used in our numerical experiments (Sec. 3.1) and the three QE GVCs localised in the proximity of the Greenland-Scotland ridge area (Sec. 3.2) are given.

3.1 The eddy-permitting global ocean model

The numerical integrations described in this manuscript are carried out using the GOSI9 global ocean configuration at $1/4°$ of horizontal resolution (GOSI9-025) developed and used by the UK Met Office Hadley Centre and the National Oceanography Centre under the umbrella of the Joint Marine Modelling Program (see Guiavarc'h et al. (2023) for a detailed description of the model). GOSI9-025 is an eddy-permitting forced ocean configuration based on the Nucleus for European Modelling of the Ocean (NEMO) numerical ocean model at version 4.0.4 (Madec & NEMO-team, 2019).

The model used in this study differs in a few details from the standard GOSI9-025 of Guiavarc'h et al. (2023):

- it is forced with the 1958-2020 JRA-55 atmospheric reanalysis (Kobayashi et al., 2015; Harada et al., 2016) instead of the 1948-2006 CORE atmospheric forcing (Large & Yeager, 2009), to cover the observational period (see Sec. 5);
- it adopts a bottom friction formulation consistent with the "law of the wall" with a bottom roughness $z_0 = 3{\times}10^{-3}$ for a better representation of the bottom boundary layer dynamics;
- it employs the Griffies et al. (1998) triad formulation for the iso-neutral diffusion since it is the only available option for using iso-neutral mixing with inclined GVCs in the current release of NEMO;
- it uses the standard NEMO pressure Jacobian scheme (Madec & NEMO-team, 2019) for a more accurate calculation of the horizontal pressure gradient force when using sloping model levels.

In the vertical direction, GOSI9-025 employs the QE z^*-coordinate of Stacey et al. (1995) and Adcroft & Campin (2004) (see Appendix B for the details) discretised using 75 levels and Madec et al. (1996) stretching function. In addition, in order to mitigate inaccuracies affecting the step-like representation of the bottom topography typical of geopotential-based models, the GOSI9-025 configuration also employs the Pacanowski et al. (1998) partial step parameterisation (see Fig. 3b). Hereafter, the GOSI9-025 model employing standard z^* levels with partial steps (z^*ps) everywhere in the domain is referred to as GOSI9-z^*ps model.

3.2 Localised general terrain-following vertical coordinates

Vertical coordinates smoothly following the seabed topography are able to offer a more realistic representation of gravity currents than models using geopotential coordinates, both in idealised (e.g., Ezer & Mellor (2004); Ezer (2005); Laanaia et al. (2010); Ilcak et al. (2012); Bruciaferri et al. (2018)) and more realistic scenarios (e.g., Käse (2003); Ezer (2006); Riemenschneider & Legg (2007); Seim et al. (2010); Colombo et al. (2020)). Therefore, in this study three different types of QE generalised terrain-following vertical coordinates are localised and tested in the Nordic overflows region.

The localisation area developed for this work includes the Greenland-Scotland ridge region and targets (where possible) the 2800 m isobath (see Fig. 3a), the depth at which ∇H decreases. In this work, the transition area is defined using the algorithm described in Appendix A. The following are the QE GVCs localised and tested in the Nordic overflows region in this paper:

- ***Vanishing quasi-sigma (vqs):*** the vqs method defines vertical coordinates following a smooth envelope topography surface H_e rather than the actual bathymetry H (with $H_e \geq H$), allowing one to reduce the steepness of computational levels with respect to classical terrain-following models (Dukhovskoy et al., 2009). While this approach is particularly effective in reducing errors in the computation

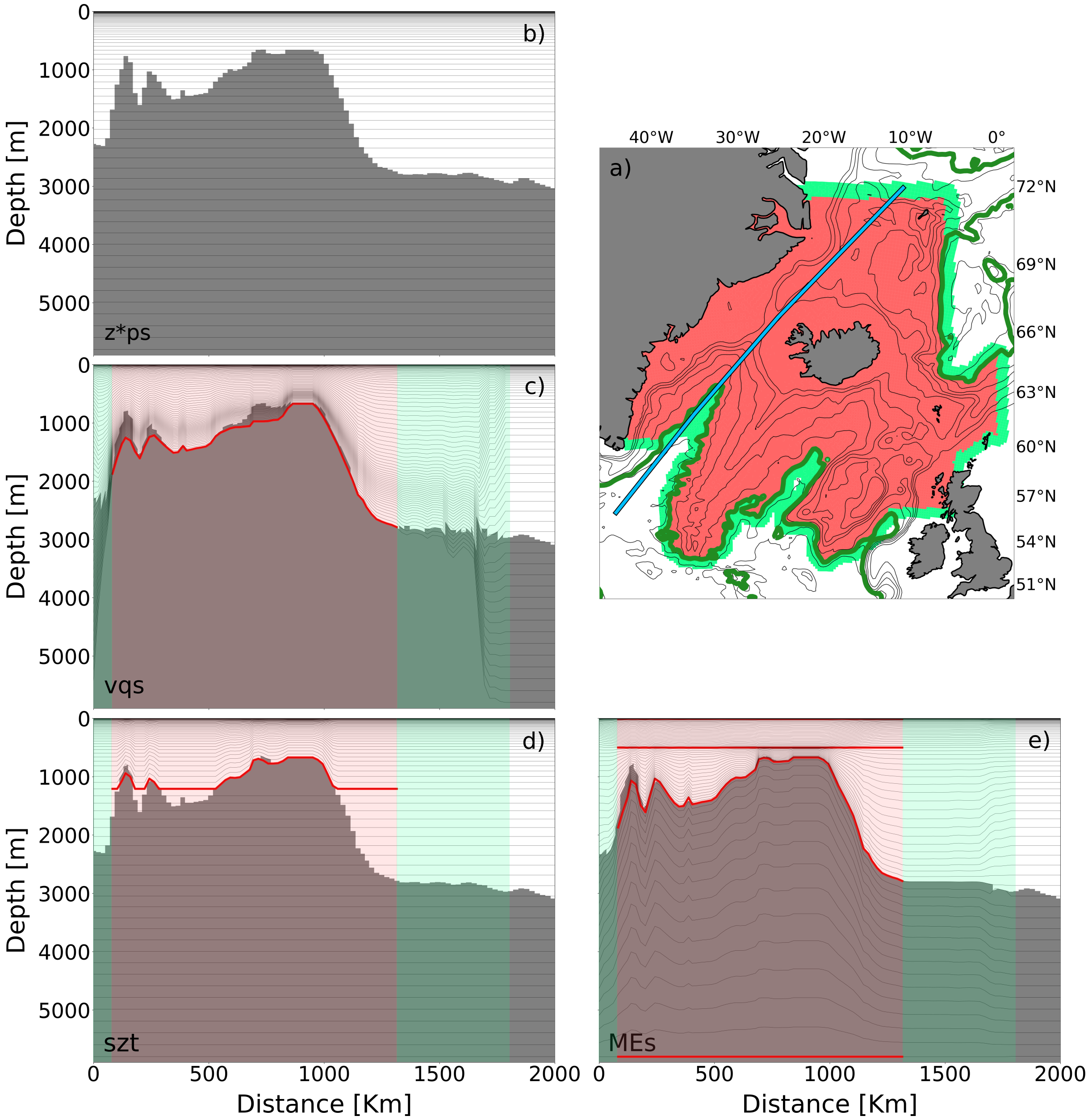

Figure 3. In panel a) the red and green regions represent the Nordic overflows localisation and transition areas used in this study, respectively, while the blue line shows the location of the model bathymetry cross-sections presented in the other panels and the green line marks the 2800 m isobath. Panel b) shows the model bathymetry cross-section extracted from the GOSI9-z^*ps model, panel c) from the GOSI9-vqs model while panel d) and e) from the GOSI9-szt and GOSI9-MEs models, respectively. In panels b) to e) the red lines shows the location of the envelopes used to configure the localised GVCs.

of horizontal pressure gradients (e.g., Dukhovskoy et al. (2009); O'Dea et al. (2012)), it can introduce spurious 'saw-tooth' patterns in the model bathymetry similar to z-level steps whenever $H_e - H$ is large, potentially affecting the accuracy of the simulated bottom dynamics. In this study, we implement local vqs vertical coordinates with a similar setting to Colombo (2018) (see Fig. 3c, Appendix B and Fig. B1b for the details).

- ***Hybrid sz-transitioning (szt):*** the szt scheme described in Wise et al. (2021) defines QE levels that follow a smooth envelope bathymetry H_e above a user-defined depth while smoothly transition into z^*-interfaces with partial steps at greater depths, effectively allowing one to combine vqs and z^* QE coordinates. In this study, we configure the local szt vertical discretisation scheme to use terrain-following levels up to $\approx 1200\ m$ (see Fig. 3d, Appendix B and Fig. B1c for the details on the configuration).

- ***Multi-Envelope s-coordinates (MEs):*** the ME method defines QE coordinate interfaces that are curved and adjusted to multiple arbitrarily defined surfaces (aka envelopes) rather than following geopotentials, the actual bottom topography or a single-envelope bathymetry as in the case of vqs or szt GVCs. In such a way, computational levels can be optimised to best represent different physical processes in different sub-domains of the model while minimising horizontal pressure gradient (HPG) errors (Bruciaferri et al., 2018, 2020; Wise et al., 2021; Bruciaferri et al., 2022). In this study, local MEs-coordinates are configured using four envelopes (see Fig. 3e, Appendix B and Fig. B1d for the details on the coordinate transformation and the set-up), so that in the Nordic overflows region model levels are nearly terrain-following to a depth of $2800\,m$.

Hereafter, the models using local vqs, szt and MEs GVCs in the Nordic overflow region are simply referred to as GOSI9-vqs, GOSI9-szt and GOSI9-MEs models.

In this study, the envelope bathymetry surfaces of the GOSI9-vqs and GOSI9-szt models or the generalised envelopes used by the GOSI9-MEs model were smoothed via the Martinho & Batteen (2006) iterative procedure. Such an algorithm aims at ensuring that the slope parameter $r = |\delta H|(2\bar{H})^{-1}$, with δH the horizontal change in H of adjacent model cells and $\bar{H}$ the mean local bottom depth (Mellor et al., 1998), is below a user defined threshold r_{max} (see Appendix C for the details on the procedure used in this paper).

Since szt-coordinates are nearly terrain-following only up to a certain prescribed depth, a more relaxed r_{max} value can be potentially applied in comparison to a similar configuration using local vqs-levels, resulting in a less smoothed envelope bathymetry. This can allow one to keep HPG error below an acceptable level while significantly reducing spurious 'saw-tooth' structures in the model bathymetry.

The ME method allows for a 3D varying maximum slope parameter r_{max}, effectively permitting to smooth the envelopes only where it is needed for maintaining HPG errors below an acceptable level. In such a way, the generation of undesired 'saw-tooth' patterns and 'step-like' structures can be significantly reduced in comparison to vqs and szt approaches. The ME approach offers great freedom in the configuration of the vertical grid, allowing one to directly control the design of model levels in each sub-zone of the vertical domain.

4 Idealised numerical experiments

Two different types of idealised numerical experiments are conducted in this study. The first one assessed whether the localised terrain-following grids can accurately compute HPGs (Sec. 4.1), a basic requirement for a robust numerical mesh that will be used for realistic oceanic simulations. The second numerical experiment evaluates the ability of the various GVCs to reduce numerical diapycnal mixing when simulating overflows (Sec. 4.2).

4.1 Errors in the computation of pressure forces

HPG errors affecting computational vertical grids are typically assessed via the classical HPG test of Haidvogel & Beckmann (1999). In this idealised numerical experiment, the ocean model is initialised at rest (i.e., $\mathbf{u} = 0$, $\eta = 0$) with a horizontally uniform stratification $\rho(z)$ so that initial horizontal density gradients are nil. In the absence of any external forcing and explicit tracers diffusion, the analytical solution for the ocean currents in this type of problem is 0 $m\,s^{-1}$. However, when using generalised $s(x, y, z, t)$ coordinates the horizontal pressure gradient $\nabla_z p$ (with $\nabla_z = (\partial_x|_z, \partial_y|_z, 0)$) becomes the result of two sizeable terms

$$\nabla_z p = \nabla_s p + \rho g \nabla_s z. \tag{8}$$

In the discrete limit, both terms on the right hand side of equation 8 are affected by distinct numerical errors that generally do not cancel, generating spurious pressure forces that drive non-trivial unphysical currents (Haney, 1991; Mellor et al., 1994; Ezer et al., 2002).

The control z^*ps model and the three GOSI9-vqs, GOSI9-szt and GOSI9-MEs models are initialised with the temperature and salinity vertical profiles shown in Fig. 4a. These synthetic profiles were suggested by Wise et al. (2021) as representative of the summer stratification in the deep eastern North Atlantic. Numerical simulations were integrated for one month with no external forcing.

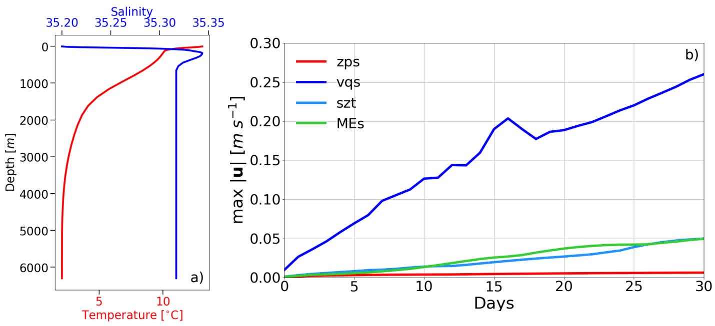

Figure 4. a) Wise et al. (2021) temperature (red) and salinity (blue) synthetic profiles used to initialise HPG experiments. b) Time evolution of the maximum HPG error $|\mathbf{u}|$ for the z^*ps (red), GOSI9-vqs (blue), GOSI9-szt (light blue) and GOSI9-MEs (light green) models.

Figure 4b presents the daily timeseries of the maximum HPG error $|\mathbf{u}|$ for the four models. The z^*ps model shows the smallest HPG error (< 0.005 $m\,s^{-1}$, in agreement with previous studies, e.g., Bruciaferri et al. (2018); Wise et al. (2021)) while the vqs model the largest (> 0.25 $m\,s^{-1}$). In the case of the GOSI9-szt and GOSI9-MEs models spurious currents are ≤ 0.05 $m\,s^{-1}$.

The envelopes of the three localised terrain-following GVCs are optimised to have HPG errors < 0.05 $m\,s^{-1}$ (see Appendix C for the details). For the GOSI9-szt and GOSI9-MEs models, this is in agreement with the results presented in Fig. 4b. However, in the case of the vqs model, spurious currents are much larger than the optimisation threshold. In order to understand the reason behind this result, Fig. 5 shows, for each grid point of the horizontal grid, the maximum in the vertical and time HPG error $|\mathbf{u}|$ for the three models using localised QE GVCs.

In the case of the GOSI9-szt and GOSI9-MEs models, HPG errors affects only the localisation area (red area in Fig. 3a), as expected. To the contrary, the vqs model presents large spurious currents in the proximity of the transition area (green region in Fig. 3a). Since the local-vqs approach relies on one single envelope bathymetry, the mismatch in depth between vqs and z^* model levels sharing the same k index can be quite large ($\approx$ 3500 m in the case of the last model level), resulting in two important consequences for the transition zone (see Fig. 3c and B1b). Firstly, computational surfaces will be particularly steep in the relaxation area, driving large HPG errors that can not be mitigated by limiting the slope parameter of the envelope bathymetry. Secondly, significant 'saw-tooth' patterns will be generated in the model bathymetry of the transition zone, introducing unrealistic spurious noise at the model grid scale. In agreement with Colombo (2018), we note that while the large HPG errors could be reduced by implementing a much wider and hand-adjusted transition area, the generation of undesired bathymetric noise in the relaxation zone appears to be a much harder problem to solve.

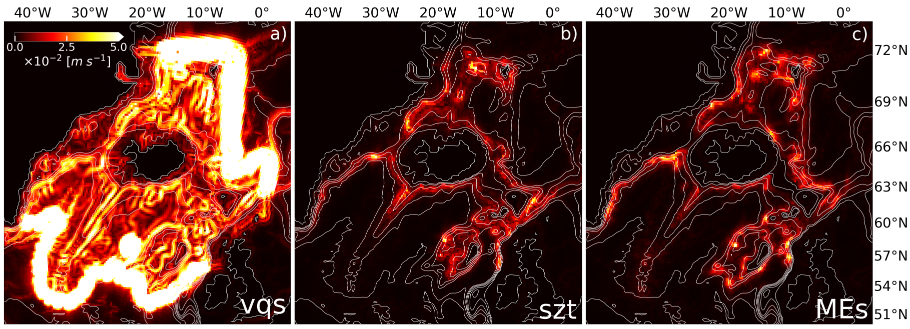

Figure 5. Maps of the maximum in the vertical and time spurious currents $|\mathbf{u}|$ $m\,s^{-1}$ after a 1 month long HPG numerical experiment for the models using localised vqs (a), szt (b) and MEs (c) GVC.

Neither the GOSI9-szt nor GOSI9-MEs models suffers from the same issues affecting local-vqs coordinates. For example, because at depth the szt approach uses the same vertical coordinate formulation of the global domain, the GOSI9-szt bathymetry in the transition zone is effectively discretised with z^*ps levels (see Fig. 3d and B1c), resulting in a smooth transition zone. Similarly, since the ME approach divides the model vertical space in sub-zones, model levels can be easily distributed along the water column to obtain a smooth transition zone free of HPG errors (see Fig. 3e and B1d and Appendix B). Given the large HPG errors affecting the GOSI9-vqs model, we conclude that the vqs approach is not suitable for the localisation method proposed in this manuscript and we continue our study only with the GOSI9-szt and GOSI9-MEs models.

4.2 Diapycnal mixing in an idealised overflow

Models with a stepped bottom topography introduce excessive numerical mixing when simulating dense gravity currents. This is the case especially at coarse horizontal resolutions such as the one used in this study, even when the partial steps parameterisation is employed (e.g., Legg et al. (2006)). Contrarily, terrain-following levels can offer a smooth representation of the sea bed, facilitating more realistic simulations of bottom intensified currents (e.g. Ezer & Mellor (2004)). The aim of this second set of idealised experiments is to evaluate the ability of localised GVCs to reduce spurious entrain-

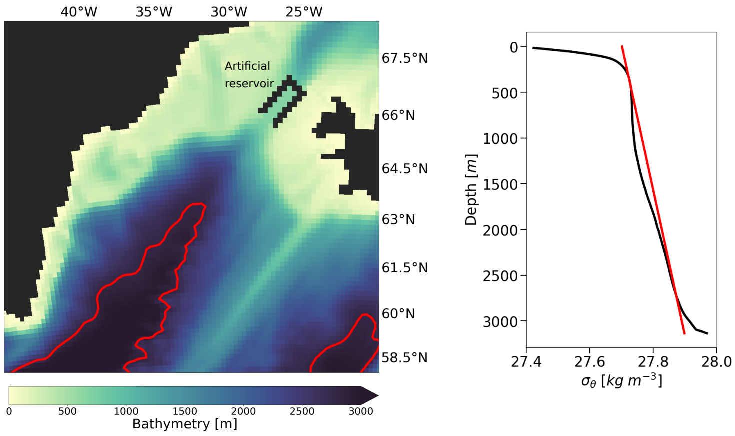

Figure 6. a) In the idealised overflow experiment, the original model bottom topography is modified to include an artificial reservoir in the proximity of the Denmark Strait. In red it is also shown the 2800 m isobath defining the boundary of the localisation area. b) Density vertical profile from OSNAP observational array in the Irminger Sea (black) compared against the analytical density profile (red) used to initialise the idealised overflows experiments.

ment and diapycnal mixing when simulating gravity currents generated by a dam-break in the Denmark Strait.

Numerical experiments are set as follows. The original model bathymetry is modified by introducing an artificial reservoir in the proximity of the Denmark Strait sill, as shown in Fig. 6a. Then, the model uses a linear equation of state (only function of temperature) and is initialised with a horizontally uniform ambient stratification $\rho(z)$ that linearly fits the observed density distribution in the middle of the Irminger Sea, as shown in Fig. 6b - observations are provided by the Overturning in the Subpolar North Atlantic Program (OSNAP, M. S. Lozier et al. (2017, 2019)). Such an initial condition is perturbed by introducing a cold dense water mass with density ρ_d such that $\Delta\rho = \max\{\rho_d - \rho(z)\} = 1.3\ kg\, m^{-3}$ inside the artificial reservoir. As already noted by Ezer (2006), this value for $\Delta\rho$ is somewhat larger than the ones observed in reality. However, one has to keep in mind that our simulations are lock-exchange gravity currents where the only forcing is represented by the buoyancy anomaly of the dense perturbation in the artificial reservoir. Therefore, $\Delta\rho$ needs to be large enough to promote a down-slope dense cascade that will continue even after the inevitably strong mixing at the beginning of the simulation. We emphasize that the aim of this second idealised experiment is to evaluate the impact of the vertical coordinate system on the simulation of a gravity current in the Denmark Strait, and not to reproduce observed properties of the overflow in this region.

In order to keep track of the cascading dense plume and facilitate our analysis, we use a passive tracer whose initial concentration C is 10 in the the cold dense water mass of the artificial reservoir while zero elsewhere. Computations are integrated for 90 days without any external forcing and using the standard GOSI9-025 setting for the numerics and the physics (Sec. 3.1), except for the use of the linear equation of state. In particular, ambient fluid entrainment and vertical mixing are explicitly taken into account by using the standard NEMO turbulent kinetic energy (TKE) scheme (see Guiavarc'h et al. 2023 for the details).

Dilution of the tracer concentration C is an indication for entrainment and mixing in of ambient fluid in the dense cascading water (Ezer, 2005; Legg et al., 2006). We define the overflow water to be the fluid with $C \geq 0.1$ and Fig. 7 and 8 show snapshots

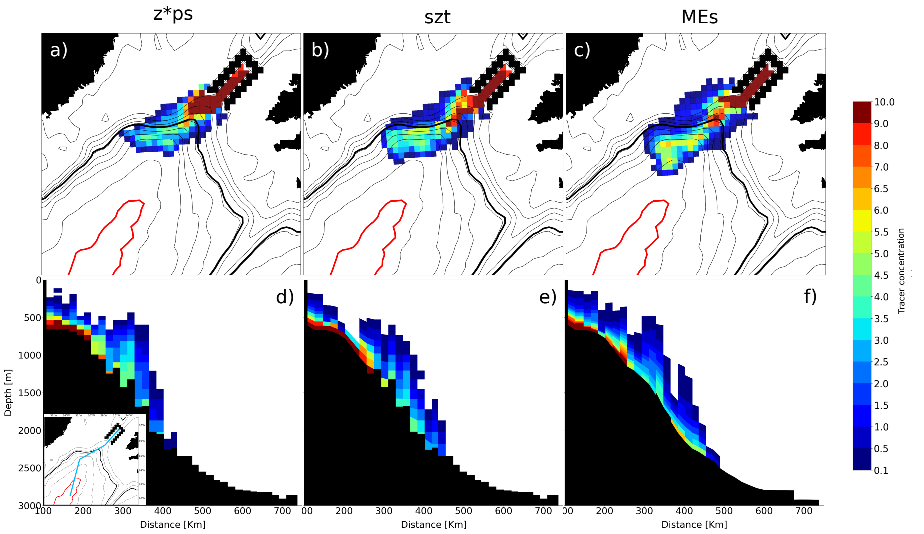

Figure 7. Passive tracer concentration at the bottom (upper row) and in a cross sections passing through the dense plume (bottom row) for the z^*ps, GOSI9-szt and GOSI9-MEs models after 30 days. Only wet cells with passive tracer concentration $C \geq 0.1$ are shown. The location of the cross section is shown in light blue in the inset. The thick red and black lines identify the 2800 m and 1200 m isobaths, respectively.

of the tracer concentration at the deepest wet cell just above the bottom topography (top row) and in a vertical cross section along the plume path (bottom row) for the three models after 30 and 90 days, respectively. All the three models simulate a dense water plume descending down the steep continental slope of the northern Irminger Sea basin which reaches the 2800 m after 90 days. However, their respective solutions for the passive tracer concentration distribution differ significantly.

The control z^*ps model produces the most diluted overflow (Fig. 7a, d and Fig. 8a, d), indicating large ambient fluid entrainment and mixing, in agreement with previous studies (e.g., Ezer (2005); Bruciaferri et al. (2018)). In the case of the GOSI9-MEs model, diapycnal mixing is significantly reduced, allowing the simulation of a much less diluted dense plume which after 90 days can reach the 2800 m isobath with up to 45% of the initial passive tracer concentration (see Fig. 8c and f). The GOSI9-szt model is able to reduce the large mixing in the first third of the simulation, reproducing a passive tracer concentration distribution similar to the one of the GOSI9-MEs model (Fig. 7b and e). However, the relatively shallow (1200 m) transition to a stepped topography leads to an increase in diapycnal mixing in the last two thirds of the simulation, slowing down and importantly diluting the GOSI9-szt overflow (Fig. 8b and e).

Qualitative examination of Fig. 7 seems to suggest that the three models may also differ in the way they represent the evolving dynamics of the dense plume. At the beginning of the simulation, the three models agree simulating a coherent down-slope cascading. However, after crossing the ≈ 1000 m isobath, the overflow reproduced by the z^*ps and GOSI9-szt models seem to move prevalently in the along-slope direction, with the bulk of the dense plume reaching a depth of $\approx$ 2000 m after 30 days (see Fig. 7a and b). In the case of the GOSI9-MEs model, after 30 days the head of the dense plume has crossed the 2500 m, indicating a larger down-slope component of the velocity. This is probably partly due to the fact that GOSI9-MEs model, with its increased resolution near the sea bed, is able to better resolve the Ekman transport at the bottom bound-

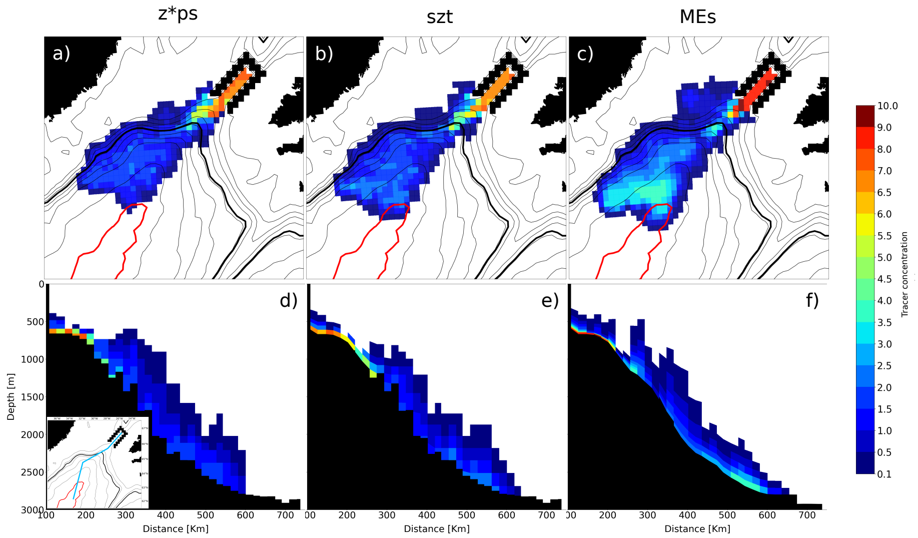

Figure 8. Same as Fig. 7 but after 90 days.

ary layer, in agreement with the findings of Ezer (2005) for the case of a classic terrain-following $\sigma-$model.

To evaluate and compare diapycnal mixing in our three simulations, Fig. 9 presents the time evolution of the distribution in density space of the total amount of passive tracer mass $Tr(x, y, \sigma_\theta, t)$. Computations are carried out for 21 density classes ($\Delta\sigma_\theta = 0.06\,kg\,m^{-3}$) and time windows Δt of 4 days. Such a metric is a modified version of the diagnostic firstly proposed by Ezer (2005); Legg et al. (2006). At the beginning of the experiments, the passive tracer marks only the heaviest density class, as in the initial condition. Once the dense overflow is initiated, all the three models reproduce strong diapycnal mixing and entrainment in the first $\approx 20-30$ days of the simulations, with the majority of the passive tracer moving towards lighter density classes. In the case of the GOSI9-z^*ps and GOSI9-szt models, the passive tracer lands and marks for the remaining two thirds of the simulations few ($\approx 2-3$) of the lightest density classes. To the contrary, in the GOSI9-MEs case after 30 days and in the second part of the simulation the passive tracer is spread within a larger number of relatively heavier density classes, demonstrating reduced diapycnal mixing.

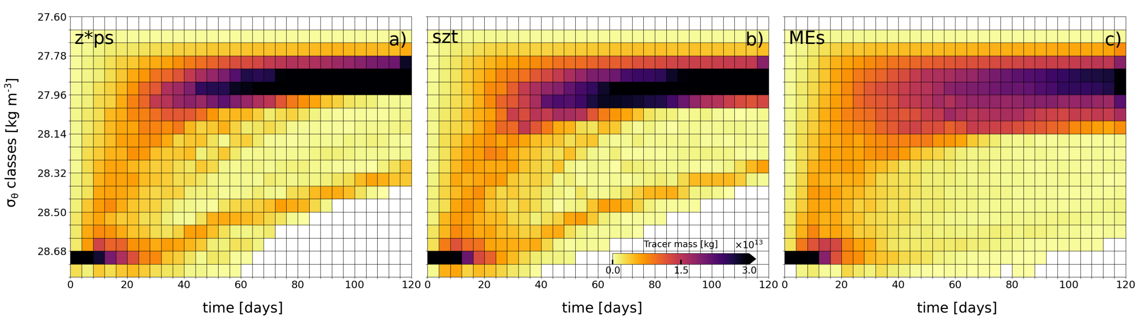

Figure 9. Distribution in density space and time of the total amount of passive tracer mass $Tr(x, y, \sigma_\theta, t)$ in kg for 21 density classes ($\Delta\sigma_\theta = 0.06\,kg\,m^{-3}$) and time windows Δt of 4 days for the GOSI9-z^*ps (a), GOSI9-szt (b) and GOSI9-MEs (c) models.

Both GOSI9-z^*ps and GOSI9-szt models present also a secondary constant diapycnal passive tracer transport event that starts around day 40 and continues until the end of the experiments and that is not present in the GOSI9-MEs simulation. Figure 7 seems to suggest that this is probably due to a larger volume of source dense water that is not able to cascade down the continental slope in the case of GOSI9-z^*ps and GOSI9-szt models and slowly mixes with the surrounding ambient water.

5 Realistic integrations

In the last set of numerical experiments the skills of the GOSI9-z^*ps, GOSI9-szt and GOSI9-MEs models in reproducing observed properties of the Nordic overflows are assessed. Numerical simulations are initialised with EN4 1995−2014 climatological January data (Good et al., 2013) and integrated from $01-01-2010$ to $01-01-2019$ using the setting for the forcing, numerics and physics described in Sec. 3.1. The first 4 years of the computations are considered spin-up time and numerical results are analysed for the period $2014-2018$.

5.1 Observations and analysis methodology

Numerical results are analysed and compared to observations in terms of hydrographic properties and total volume transports of the Nordic overflows. Observations include the World Ocean Atlas 2018 objectively analysed climatology (WOA18; Boyer et al. (2018)) for the bottom temperature and salinity as well as a number of selected cross-sections of measured in-situ temperature, salinity and normal velocities - see Tab. 1 for the details and Fig. 1 for the geographical location of the sections. In the case velocities observations were not available for a particular section, previously published estimates of overflows volume transport are used instead.

ID	Covered geographical area	Variables	Validity period	Dataset type	References
WOA18	World Ocean	Bottom Tem. and Sal.	2005 − 2017	clim. field @ 1/4° hor. res.	Boyer et al. (2018)
DS	Denmark Strait	Tem., Sal. OVF vol. transp.	1990 − 2012 1996 − 2015	clim. section average value	Mastropole et al. (2017) Østerhus et al. (2019)
IS	Irminger Sea	Tem., Sal., Vel.	2014 − 2018	30 days mean sections	M. S. Lozier et al. (2017) Li et al. (2023)
IB	Icelandic basin	Tem., Sal., Vel.	2014 − 2018	30 days mean sections	M. S. Lozier et al. (2017) Li et al. (2023)
IFR	Iceland-Faroe Ridge	Tem., Sal.	Aug. 2016	mean section	Quadfasel (2018) Hansen et al. (2018)
FSC	Faroe-Shetland Channel	Tem., Sal.	1994 − 2005	clim. section	Hansen & Østerhus (2000) Hughes et al. (2006)
FBC	Faroe-Bank Channel	OVF vol. transp.	1994 − 2005	average value	Østerhus et al. (2019)
WTR	Wyville Thomson Ridge	OVF vol. transp.	2006 − 2013	average value	Østerhus et al. (2019)
CFGZ	Charlie-Gibbs Fracture Zone	OVF vol. transp.	2010 − 2012	average value	Xu et al. (2018)

Table 1. List of observational datasets used to analyse the results of the realistic experiments.

The positive northward volume transport in Sv (1 Sv = $10^6\, m^3 s^{-1}$) of the observed (when available) and simulated dense overflows $\Psi^\star(t)$ is calculated as

$$\Psi^\star(t) = \iint\limits_{A^\star} \mathbf{u} \cdot \hat{\mathbf{n}}\, dA, \tag{9}$$

where $\mathbf{u}(x, y, z, t)$ is the horizontal velocity field, $\hat{\mathbf{n}}$ is a unit vector normal to the cross section and $A^{\star}$ represents the area of the cross section where the potential density anomaly σ_θ is larger than a chosen σ_θ^{ovf} threshold.

Similarly, the mean hydrographic properties of overflows water masses are computed as

$$\phi^{\star}(t) = \frac{1}{V^{\star}} \iiint\limits_{V^{\star}} \phi \, dV, \tag{10}$$

where $\phi(x, y, z, t)$ can be either temperature (T), salinity (S) or potential density anomaly (σ_θ) and $V^{\star}$ is the volume of water with $\sigma_\theta > \sigma_\theta^{ovf}$.

Typically, a widely accepted value of $\sigma_\theta^{ovf} = 27.80\ kg\ m^{-3}$ is used to separate the Nordic overflows water masses from the surrounding ambient fluid in the proximity of the Greenland-Scotland ridge (e.g., Dickson & Brown (1994); Østerhus et al. (2019)). As we will show later in our analysis (see Sec. 5.2), such a value for σ_θ^{ovf} works well also in our simulations to identify the dense waters of the overflows upstream.

Because of the entrainment of generally saltier ambient waters, a larger value for σ_θ^{ovf} is usually applied in the literature to track the modified DSOW and ISOW water masses farther downstream. Typical values are $\sigma_\theta^{ovf} = 27.85\ kg\ m^{-3}$ (Dickson et al., 2008) or $\sigma_\theta^{ovf} = 27.88\ kg\ m^{-3}$ (Kieke & Rhein, 2006) in the case of DSOW and $\sigma_\theta^{ovf} = 27.85\ kg\ m^{-3}$ for the ISOW (e.g., Xu et al. (2010); Holliday et al. (2015)). However, as we will show later (see Sec. 5.3), excessive spurious mixing affects the GOSI9-z^*ps and GOSI9-szt models, preventing them from representing such dense waters in the deep Irminger and Icelandic basins.

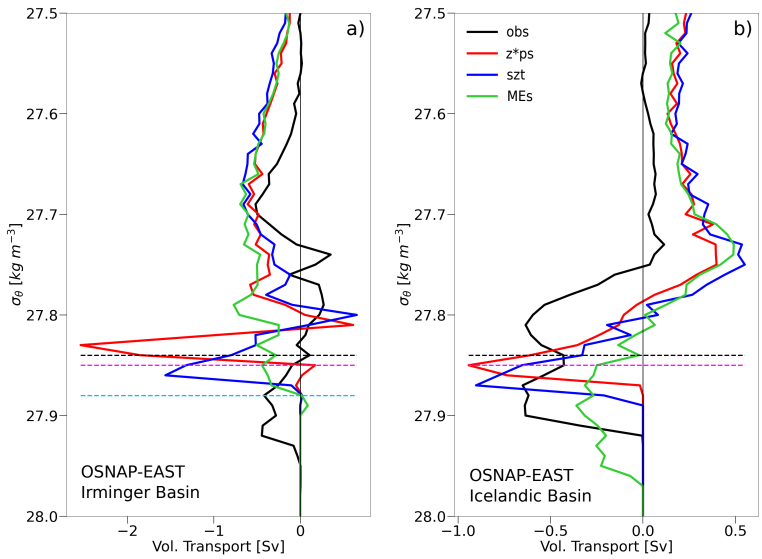

Figure 10. Volume transports (positive northward) integrated in potential density bins of $0.01\ kg\,m^{-3}$ and averaged across the $2014 - 2018$ period for OSNAP observations (in black) and GOSI9-z^*ps (red), GOSI9-szt (blue) and GOSI9-MEs (green) models in the Irminger Sea (a) and in the Icelandic basin (b). The black dashed lines mark the $\sigma_\theta^{ovf} = 27.84\ kg\,m^{-3}$ limit adopted in this study to identify overflow waters. The magenta and light blue dashed lines represent the limits ($\sigma_\theta^{ovf} = 27.85\ kg\ m^{-3}$ and $\sigma_\theta^{ovf} = 27.88\ kg\ m^{-3}$, respectively) typically used in literature to define DSOW and ISOW water masses downstream.

Therefore, a different threshold is needed in order to identify overflows waters downstream the Greenland-Scotland ridge in our simulations. Ideally, the σ_θ^{ovf} cutoff should be the boundary that separates the densest water masses in the basin where a local maximum in volume transport exists. A value of $\sigma_\theta^{ovf} = 27.84\ kg\,m^{-3}$ is chosen in this work. As shown later in Sec. 5.3, such a limit identifies in the IS and IB cross-sections dense water masses that agree well for both observations and modelling results. In addition, Fig. 10 presents the 2014-2018 mean volume transports distribution as a function of potential density classes. In the case of the ISOW (Fig. 10b), the $\sigma_\theta^{ovf} = 27.84\ kg\,m^{-3}$ limit correctly identifies the densest water masses in the observations and the models with a relative peak in the volume transports. For the DSOW (Fig. 10a), the chosen threshold works well for the observations and the GOSI9-szt and GOSI9-MEs models, while it does not capture the densest local maximum in transport for the case of the GOSI9-z^*ps model. However, we note that the relative peak of the GOSI9-z^*ps model is only marginally missed, while using a lower σ_θ^{ovf} limit will inevitably include in the analysis of the observations lighter waters not belonging to the overflows.

5.2 Properties of the Nordic overflows entering the North Atlantic

We begin our analysis evaluating the characteristics of the overflows simulated by the three models when crossing the Greenland-Scotland ridge. Table 2 compares the 2014−2018 time-averaged values of the overflows mean hydrographic properties simulated by the three models in the proximity of the upstream DS, IFR and FSC cross-sections and the mean volume transports reproduced in the DS, IFR, FBC and WTR sections (see Tab. 1 for more details, Fig. 1 for the locations of the sections and Appendix D for a list of the acronyms) against existing estimates from observations (the actual time-series used to compute the time averages can be found in Fig. S1 and Fig. S2 of the Supporting Information). In addition, Fig. 11 compares the 2014−2018 averaged potential density, temperature and salinity fields simulated by the three models in the DS, IFR and FSC cross-sections against the observations. As explained in Sec. 5.1, in the proximity of the Greenland-Scotland ridge the Nordic overflows water masses are identified using the threshold $\sigma_\theta^{ovf} = 27.80\ kg\,m^{-3}$.

Section ID	Variables	Observations	GOSI9-z^*ps	GOSI9-szt	GOSI9-MEs
DS	$\langle T^\star \rangle$ [°C]	0.74	1.96 ± 0.49	2.22 ± 0.48	1.99 ± 0.49
	$\langle S^\star \rangle$	34.85	34.96 ± 0.04	34.98 ± 0.05	34.97 ± 0.05
	$\langle \sigma_\theta{}^\star \rangle$ [$kg\,m^{-3}$]	27.94	27.93 ± 0.01	27.93 ± 0.01	27.94 ± 0.01
	$\langle \Psi^\star \rangle$ [Sv]	-3.2 ± 0.5	-2.2 ± 0.4	-2.0 ± 0.3	-2.3 ± 0.4
IFR	$\langle T^\star \rangle$ [°C]	2.52	2.63 ± 0.39	2.93 ± 0.49	2.64 ± 0.40
	$\langle S^\star \rangle$	34.97	34.97 ± 0.03	34.99 ± 0.04	34.97 ± 0.03
	$\langle \sigma_\theta{}^\star \rangle$ [$kg\,m^{-3}$]	27.90	27.89 ± 0.02	27.88 ± 0.01	27.89 ± 0.02
	$\langle \Psi^\star \rangle$ [Sv]	-0.4 ± 0.3	-2.2 ± 0.4	-2.0 ± 0.3	-0.32 ± 0.2
FSC	$\langle T^\star \rangle$ [°C]	0.67	0.49 ± 0.16	1.44 ± 0.19	0.79 ± 0.23
	$\langle S^\star \rangle$	34.92	34.93 ± 0.01	34.98 ± 0.02	34.94 ± 0.01
	$\langle \sigma_\theta{}^\star \rangle$ [$kg\,m^{-3}$]	27.99	28.01 ± 0.01	27.98 ± 0.01	27.99 ± 0.01
FBC	$\langle \Psi^\star \rangle$ [Sv]	-2.0 ± 0.3	-2.0 ± 0.3	-2.0 ± 0.4	-2.0 ± 0.4
WTR	$\langle \Psi^\star \rangle$ [Sv]	-0.2 ± 0.1	0.0 ± 0.0	-0.2 ± 0.3	-0.1 ± 0.1

Table 2. Time averaged (mean ± SD) temperature ($\langle T^\star \rangle$), salinity ($\langle S^\star \rangle$), potential density anomaly ($\langle \sigma_\theta{}^\star \rangle$) and transport ($\langle \Psi^\star \rangle$) of overflow water masses ($\sigma_\theta^{ovf} = 27.80\ kg\,m^{-3}$) estimated from observations and simulated by the models in the DS, FSC, IFR, FBC and WTR upstream sections.

In the case of the DS section, the three models simulate density structures which are very similar and in agreement with the observations (see Fig. 11a.1, b.1, c.1 and d.1

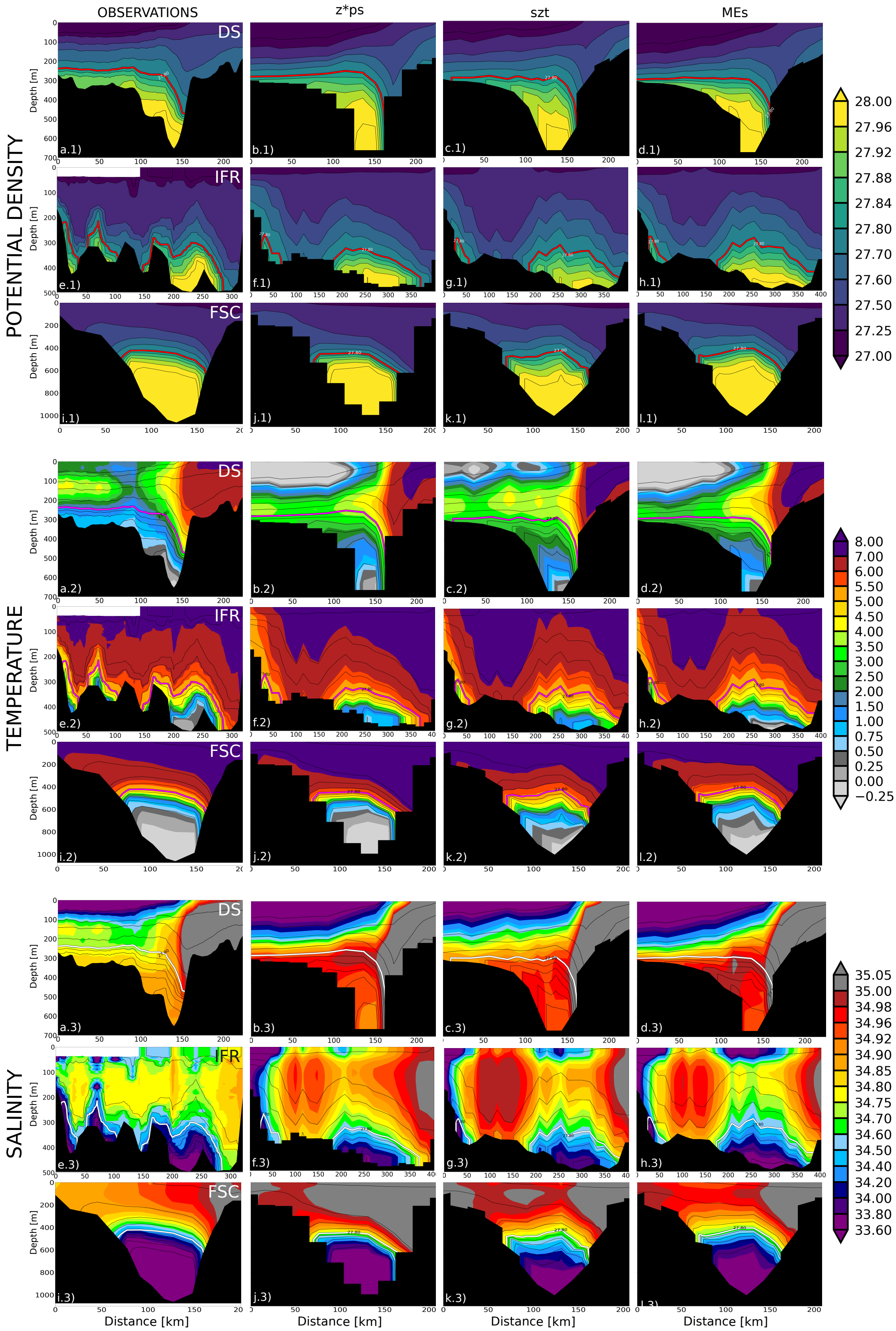

Figure 11. Potential density anomaly (panels $a.1$ to $l.1$), temperature (panels $a.2$ to $l.2$) and salinity (panels $a.3$ to $l.3$) fields observed (1^{st} column) and simulated by the GOSI9-z^{*}ps (2^{nd} column), GOSI9-szt (3^{rd} column) and GOSI9-MEs (4^{th} column) models in the Denmark Strait (DS), Iceland-Faroe-Ridge (IFR) and Faroe-Bank-Channel (FBC) cross-sections. The red, magenta and white lines show the 28.80 $kg\,m^{-3}$ isopycnal.

and Tab. 2). However, the analysis of the active tracers fields indicate that large biases consistently affect the DSOW represented by the three models (see Fig. 11a.2, b.2, c.2 and d.2, Fig. 11a.3, b.3, c.3 and d.3 and Tab. 2), with mean salinity errors > 0.1 and average warm biases > 1.0 °C. The three models also underestimate the DSOW mean volume transport in the DS section (differences are ≈ 1 Sv, see Tab. 2).

In the proximity of the IFR section, the GOSI9-z^*ps and GOSI9-MEs models simulate ISOW with mean hydrographic properties very similar to the observations (warm bias of $\approx$ 0.1 °C and average absolute salinity errors $<$ 0.01), resulting in marginally less dense ($\approx 0.01\ kg\,m^{-3}$) overflows water masses (see Fig. 11$e.^*$, $f.^*$, $g.^*$ and $h.^*$ and Tab. 2). In the case of the GOSI9-szt model, results present moderately larger errors, with average values of ≈ 0.5 °C for temperature, ≈ 0.025 for salinity and $\approx 0.02\ kg\,m^{-3}$ for density. For the mean volume transport (see Tab. 2), the GOSI9-MEs model results to be the more accurate (errors < 1.0 Sv) while the GOSI9-z^*ps and GOSI9-szt models present larger biases (> 1.5 Sv).

In the case of the FSC section, only climatological hydrographic observations from Hansen & Østerhus (2000); Hughes et al. (2006) were accessible in this study, while direct estimations of the overflows volume transport were available only for the two farthest downstream FBC and WTR sections. In the FSC section, the GOSI9-szt model simulates an ISOW that is moderately warmer and saltier than the observations (mean absolute errors of ≈ 0.7 °C and ≈ 0.06, respectively), while the GOSI9-z^*ps and GOSI9-MEs models show much reduced biases (mean absolute errors $<$ 0.2 °C for temperature and $\leq$ 0.02 for salinity, see also Fig. 11$i.^*$, $j.^*$, $k.^*$, $l.^*$ and Tab. 2). For the volume transport (see Tab. 2), the three models are in good agreement with the observations in the case of the FBC section; in the WTR transect, the GOSI9-szt model presents the highest accuracy while the GOSI9-MEs model shows large differences with the observations and the GOSI9-z^*ps model totally misses this secondary path of the Nordic overflows.

There are two key points to draw from this Section. Firstly, we note that similar biases in temperature, salinity and transport seem to affect the three models, with larger magnitude in the Greenland-Iceland ridge (i.e., the DS section) than in the Iceland-Scotland ridge (i.e., the FSC, FBC, IFR and WTR sections). Secondly, we observe that in general the local MEs GVC seems to have a small positive impact on the mean properties of the overflows upstream, while using local szt levels seems to somewhat degrade the properties of the simulated DSOW and ISOW, especially in the case of the FSC and IFR sections.

5.3 Dense overflows downstream the Greenland-Scotland Ridge

We continue our analysis assessing the properties of the Nordic overflows simulated by the three models downstream the Greenland-Scotland ridge. Table 3 compares the 2014−2018 time-averaged values of measured and simulated mean overflows hydrographic properties in the IS and IB sections and the overflows volume transport in the IS, IB and CGFZ sections (see Tab. 1 for more details and Fig. S3 and Fig. S4 of the Supporting Information for the actual time-series). Moreover, Fig. 12 presents the 2014−2018 averaged potential density anomaly, temperature and salinity fields observed and simulated by the three models along the OSNAP East array (M. S. Lozier et al., 2017; Li et al., 2023), which includes the Irminger Sea (IS) and the Icelandic Basin (IB) sections. Downstream the Greenland-Scotland ridge we use a density threshold σ_θ^{ovf} of 27.84 $kg\,m^{-3}$ to identify the modified DSOW and ISOW water masses (see Sec. 5.1 for the details).

In the IS section, the GOSI9-MEs model is able to reproduce a modified overflow water mass which is in good agreement with the observations for the density (mean absolute error is $< 0.003\ kg\,m^{-3}$). Contrarily, in the case of the GOSI9-z^*ps and GOSI9-szt simulations the deep waters are less dense than measurements, with an average ab-

Section ID	Variables	Observations	GOSI9-z^*ps	GOSI9-szt	GOSI9-MEs
IS	$\langle T^\star \rangle$ [$^\circ$C]	2.52 ± 0.02	2.83 ± 0.03	2.93 ± 0.01	2.82 ± 0.01
	$\langle S^\star \rangle$	34.93 ± 0.00	34.94 ± 0.00	34.95 ± 0.00	34.96 ± 0.00
	$\langle \sigma_\theta{}^\star \rangle$ [$kg\,m^{-3}$]	27.87 ± 0.00	27.86 ± 0.00	27.86 ± 0.00	27.87 ± 0.00
	$\langle \Psi^\star \rangle$ [Sv]	-2.5 ± 1.4	-0.7 ± 1.4	-3.7 ± 1.2	-1.6 ± 1.1
IB	$\langle T^\star \rangle$ [$^\circ$C]	2.82 ± 0.01	3.27 ± 0.08	3.11 ± 0.04	2.77 ± 0.03
	$\langle S^\star \rangle$	34.97 ± 0.00	34.99 ± 0.01	34.98 ± 0.00	34.98 ± 0.01
	$\langle \sigma_\theta{}^\star \rangle$ [$kg\,m^{-3}$]	27.88 ± 0.00	27.85 ± 0.00	27.86 ± 0.00	27.89 ± 0.00
	$\langle \Psi^\star \rangle$ [Sv]	-4.1 ± 1.0	-0.7 ± 0.5	-1.8 ± 0.8	-3.1 ± 0.4
CGFZ	$\langle \Psi^\star \rangle$ [Sv]	-1.7 ± 0.5	$+0.2 \pm 0.7$	-0.1 ± 0.9	-0.8 ± 1.1

Table 3. Time averaged (mean ± SD) temperature ($\langle T^\star \rangle$), salinity ($\langle S^\star \rangle$), potential density anomaly ($\langle \sigma_\theta{}^\star \rangle$) and transport ($\langle \Psi^\star \rangle$) of overflow water masses ($\sigma_\theta^{ovf} = 27.84\ kg\,m^{-3}$) estimated from observations and simulated by the models in the IS, IB and CGFZ downstream sections.

solute bias $> 0.01\ kg\,m^{-3}$ (see upper rows of Fig. 12 and Tab 3). Our analysis also shows that important positive biases in temperature (> 0.3 °C) and salinity (> 0.01) affect the three models (see middle and bottom rows of Fig. 12 and Tab 3). In the case of the transport, the 2014−2018 mean DSOW volume transport simulated by the GOSI9-MEs model is the most similar to the one estimated from OSNAP observations, followed by the ones of the GOSI9-szt and GOSI9-z^*ps models.

The results for the overflow density in the IB section are similar to the ones of the IS section, with the GOSI9-MEs model being the only one able to reproduce deep dense water masses with $\sigma_\theta > 27.88\ kg\,m^{-3}$ as the observations (see upper rows of Fig. 12 and Tab. 3). In addition, all three models present a mean positive bias > 0.01 for the overflow salinity in the IB section (see bottom rows of Fig. 12 and Tab. 3); for the temperature (see middle rows of Fig. 12 and Tab. 3) the GOSI9-z^*ps and GOSI9-szt simulations show warm biases of ≈ 0.4 °C and ≈ 0.3 °C, respectively, while the GOSI9-MEs model is in very good agreement with the observations (mean absolute bias ≈ 0.05 °C). Regarding the volume transport, the mean estimate from the GOSI9-MEs simulation is the closest to the one from observations (difference is ≈ 1 Sv), while GOSI9-z^*ps and GOSI9-szt mean values present larger biases (see Tab. 3).

In the case of CGFZ section, no hydrographic observations were available for this study and the mean volume transport estimate of Xu et al. (2018) is used. For the GOSI9-z^*ps model, a small mean transport in the opposite direction of the observations exists (see Tab. 3), while the GOSI9-szt simulation reproduces a mean transport that agrees with the observations in direction but is significantly weaker. In contrast, the GOSI9-MEs model represents a northward volume transport that better agrees with published estimates of magnitude (see Tab. 3).

In agreement with the findings of the idealised overflow experiment of Sec. 4.2, this Section demonstrates that the type of vertical coordinates has a large impact on the accuracy of the simulated overflows downstream the Greenland-Scotland ridge. Using local ME terrain-following levels seems to allow the model to quickly recover from the large inaccuracies of the initial condition at depth (see Fig. S3 of the Supporting Information for more details) and reproduce deep overflow water masses that are similar in density to the observations. Conversely, using a step-like bottom topography (either fully as in the control GOSI9-z^*ps model or only at depths $> 1200\ m$ as in the GOSI9-szt simulation) seems to introduce large spurious diapycnal mixing, excessively diluting the overflows along their descending paths. The shallow transition from smooth to stepped bathymetry of the GOSI9-szt model seems to mitigate some overflows biases (e.g. volume transport or hydrography in the IB), while having small negative impact on others (e.g. hydrography in the IS).

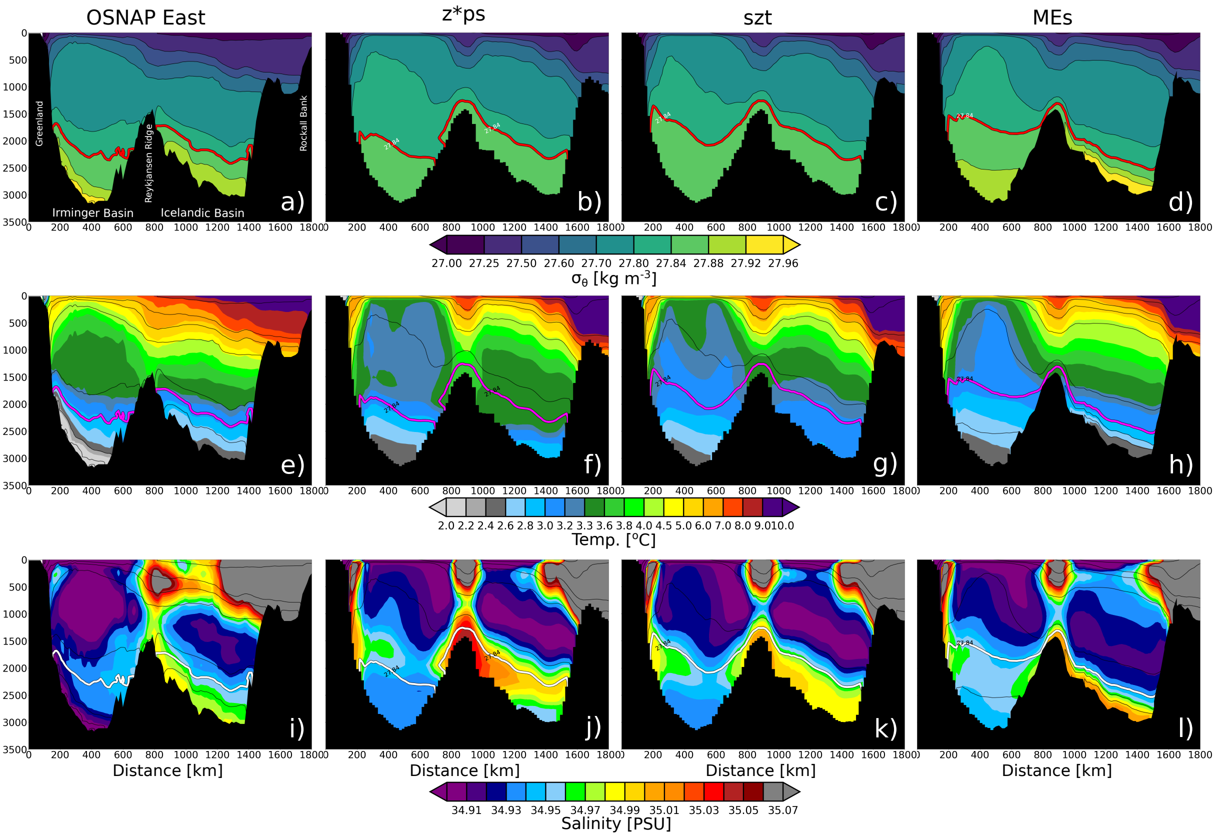

Figure 12. Potential density anomaly (upper row), temperature (middle row) and salinity (bottom row) fields observed (1^{st} column) and simulated by the GOSI9-z^*ps (2^{nd}), GOSI9-szt (3^{rd} column) and GOSI9-MEs (4^{th} column) models in the Irminger Sea (IS) and Icelandic Basin (IB) cross-sections (see Fig. 1 for their locations). The red, magenta and white lines show the 28.84 $kg\,m^{-3}$ isopycnal.

Our analysis also shows that important biases seems to affect the downstream hydrography of the overflows simulated by the three models, with discrepancies from observations that are buoyancy compensated and sometimes larger in the case of the models using localised GVCs (e.g. salinity in the IS section of the GOSI9-szt and GOSI9-MEs models).

5.4 Hydrographic biases at the bottom and overflow pathways

The aim of this Section is to better understand the origin of the large upstream and downstream biases presented in Sec. 5.2 and Sec. 5.3. Figure 13 compares the 2014−2018 bottom temperature and salinity fields simulated by the GOSI9-z^*ps, GOSI9-szt and GOSI9-MEs models in the Nordic overflows region against the ones from the 2005−2017 WOA18 climatology (Boyer et al., 2018) while Fig. 14 presents the inter-models' differences for the bottom hydrography.

The GOSI9-z^*ps model shows important bottom biases in both basins (Fig. 13b and f). The bottom temperature of the deep part of the IS and along the continental slope of Greenland is generally significantly warmer than WOA18 climatology, with errors between ≈ 0.7 °C and 1.2 $°C$. Similarly, at the bottom of the IB and along the east flank of the RR a warm bias of $\approx 0.5-0.7$ °C exists. The GOSI9-z^*ps bottom waters show also a strong salinity bias at depths around $1500-2000$ m along the continental

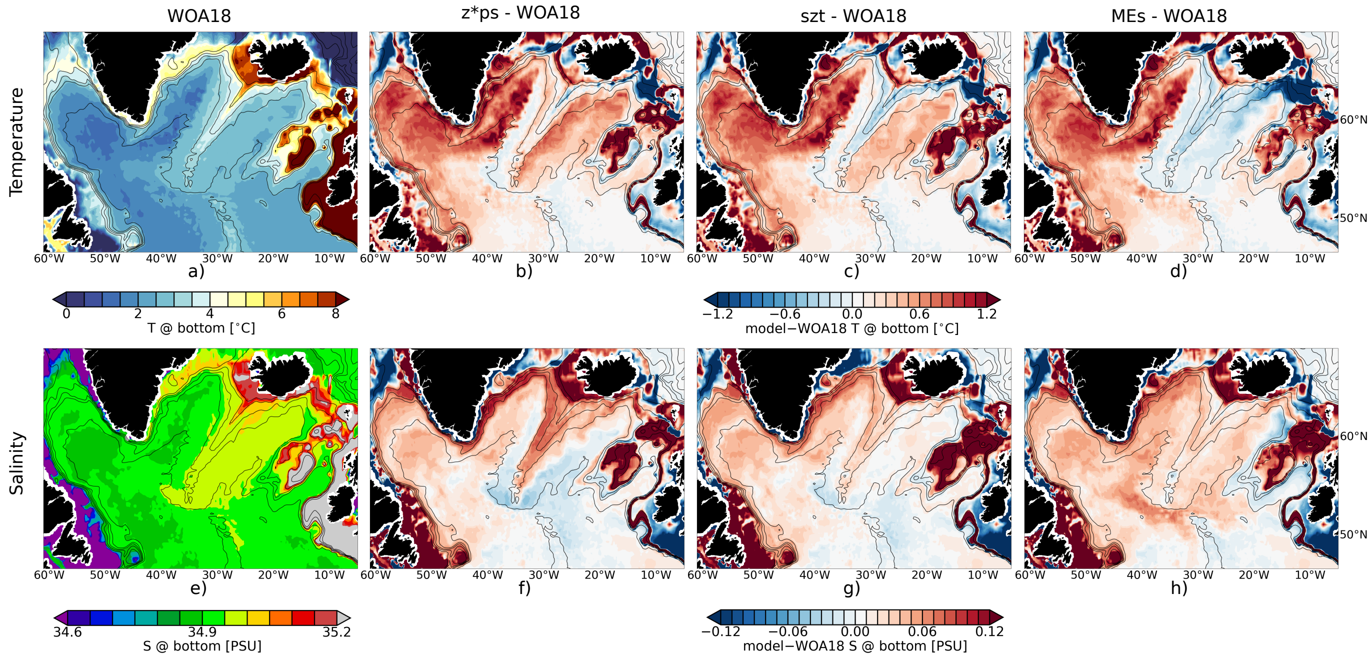

Figure 13. *Upper row*: bottom temperature field in the Nordic Seas region from 2005-2017 WOA18 climatology (a) and differences (model-WOA18) with GOSI9-z^*ps (b), GOSI9-szt (c) and GOSI9-MEs (d) models. *Bottom row*: same as in the *upper row* but for the bottom salinity. Black thin lines identify the 500 m, 1000 m, 1500 m, 2000 m and 3000 m isobaths.

slope of both the IS and IB, with errors of $\approx$ 0.07 $-$ 0.10 and $\approx$ 0.04 $-$ 0.06, respectively. Noteworthy, at larger depths the GOSI9-z^*ps bottom salinity is far more similar to the WOA18 climatology in both basins, with average differences $\leq$ 0.01.

In the case of the GOSI9-MEs model, the bottom temperature is significantly more accurate than the other two models (Fig. 13d), with improvements over the GOSI9-z^*ps model $\geq$ 0.5 °C in the IB and in the range $\approx$ 0.1 $-$ 0.5 °C for the bottom temperature along the continental slope of Greenland at depths around 1000$-$2500 m. In the deepest part of the IS the three models seem to be equivalent for the bottom temperature, with differences that are $\leq$ 0.1 °C (see Fig. 13 and Fig. 14). For salinity, the GOSI9-MEs model presents a bottom positive salinity bias at depths $\geq$ 2000 m in both the IS and IB, with errors that are between 0.2 $-$ 0.7, up to $\approx$ 0.06 larger than the GOSI9-z^*ps error. Contrarily, for depths between $\approx$ 1000$-$2000 m along the continental slope of both the IS and IB the GOSI9-MEs model shows better accuracy for the bottom salinity than the control GOSI9-z^*ps model, with improvements in the $\approx$ 0.2 $-$ 0.5 range.

The GOSI9-szt model presents temperature and salinity differences with the GOSI9-z^*ps model that are generally similar to the ones of the GOSI9-MEs model in terms of spatial distribution, but typically much weaker (see Fig. 13c and g and Fig. 14a, c, d and f). In particular, the bottom temperature of the GOSI9-MEs model shows improvements over the GOSI9-szt model $\geq$ 0.5 °C in the IB and up to $\approx$ 0.3 °C in the IS for depths between 2000 $-$ 2500 m (Fig. 14c). In the case of salinity, the GOSI9-szt and GOSI9-MEs models show similar improvements (average differences are $<$ 0.01) over the GOSI9-z^*ps model along the continental slope of the IS and IB for depths in the range $\approx$ 1000 $-$ 2000 m, while at larger depths the GOSI9-MEs model show higher salinity biases.

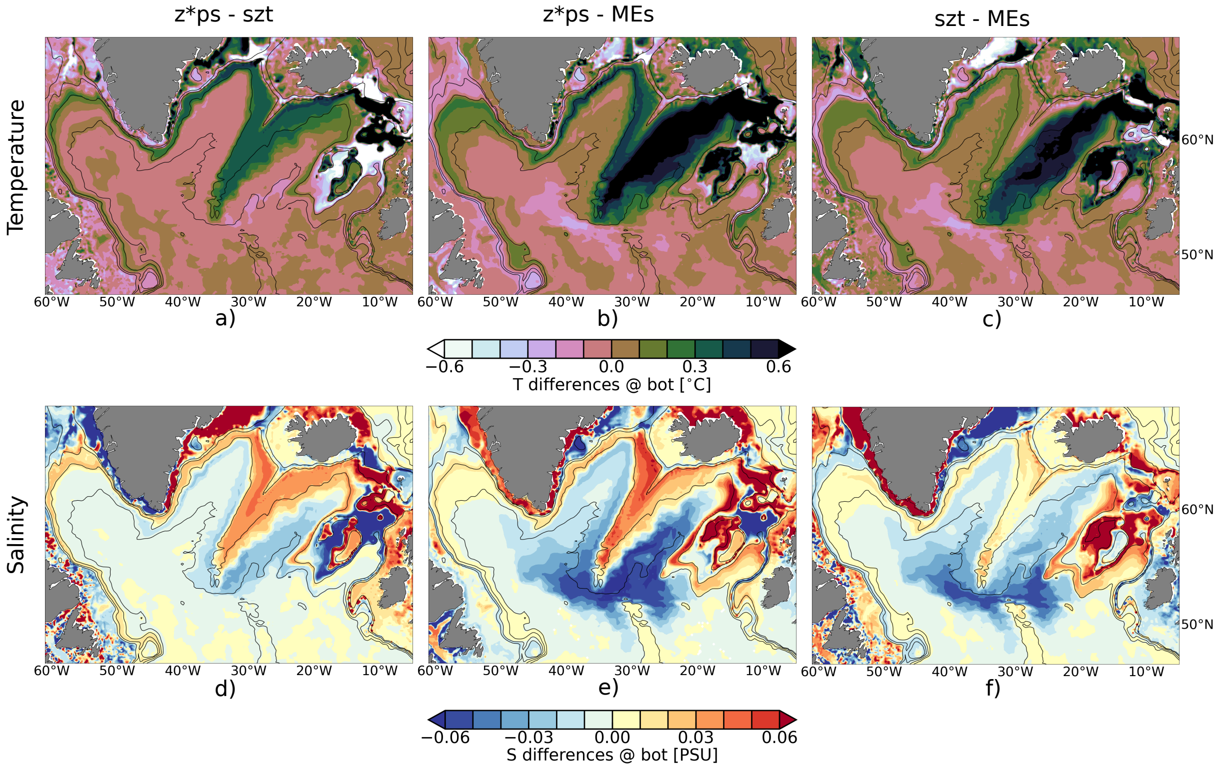

Figure 14. Differences between the control GOSI9-z^*ps model and the GOSI9-szt and GOSI9-MEs models for the bottom temperature (*upper row*) and salinity (*bottom row*). Black thin lines identify the 500 m, 1000 m, 2000 m and 3000 m isobaths.

We continue the analysis presenting in Fig. 15 maps of the volume transport and layer thickness of the overflowing dense waters ($\sigma_\theta \geq 27.84\ kg\,m^{-3}$) as reproduced by the three models.

The ISOW of the GOSI9-MEs simulation is in good agreement with observations, descending along the east flank of the RR and the deep part of the basin and leaving the IB via gaps in the RR or flowing through the CGFZ (see Fig. 1), as shown by the circulation patterns of Fig. 15c and the spreading pathways of the differences for the bottom tracers between GOSI9-MEs and GOSI9-z^*ps models of Fig. 14b and e (the latter are also in very good agreement with the overflow pathways analysis presented in figure 3 of S. M. Lozier et al. (2022)).

To the contrary, in the GOSI9-z^*ps and GOSI9-szt models the IB overflow flows along a narrower part of the east side of the RR, presents a weaker transport (especially in the control model) and leaves the IB only via the RR, with no circulation through the CGFZ (see Fig. 15a and b, Fig. 14a and Tab. 3).

In the IS, the GOSI9-z^*ps model simulates a narrow and thin overflow water mass flowing along the continental slope of Greenland with weak transport and confined below the 2000 m isobath, while in the GOSI9-szt experiment the DSOW flow is much stronger and intersects the $\approx 1000 - 2000\ m$ depth range. The GOSI9-MEs model reproduces a DSOW flowing at depths $\geq 2000\ m$ as the GOSI9-z^*ps model but with a much stronger transport similar to the one of the GOSI9-szt simulation.

In general, the net southward transport reproduced by the GOSI9-szt and GOSI9-z^*ps models in the IS is significantly larger than the one of the GOSI9-MEs simulation (see Fig. 10a). As already suggested by the idealised experiments, this can be partially

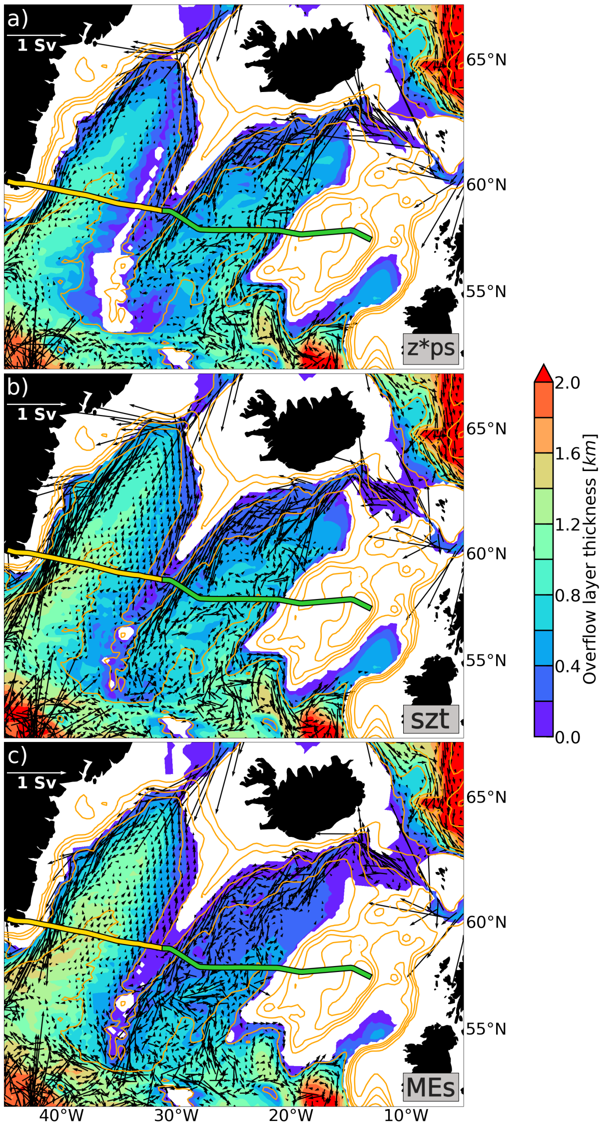

Figure 15. Layer thickness and associated volume transport of overflowing dense waters ($\sigma_\theta \geq 27.84\ kg\,m^{-3}$) for the GOSI9-$z^*$ps (a), GOSI9-$szt$ (b) and GOSI9-MEs (c) models. Thick yellow and green lines show the location of the IS and IB sections, respectively. Thin yellow lines present the 500 m, 1000 m, 1500 m, 2000 m and 3000 m isobaths

.

attributed to the fact that in the GOSI9-MEs model the Ekman bottom transport is better represented, breaking geostrophy and hence increasing the down-slope component of the flow. The net southward transport of the GOSI9-z^*ps model between 27.80-27.85 presented in Fig. 10a is much larger than the ones of the other two models: this is probably a consequence of the fact that in the GOSI9-z^*ps model the deep northward flow entering the IS is very weak, as shown by Fig. 15a.

5.5 The impact of vertical coordinates and model biases on overflows simulations

The tracers biases at the bottom and overflow pathways described in Sec. 5.4, together with the analysis of the upstream and downstream hydrography and transport presented in Sec. 5.2 and Sec. 5.3 indicates the following mechanisms for the impact of model biases and type of vertical coordinates on the overflows properties.

The three models simulate an ISOW crossing the Greenland-Scotland ridge with broadly similar hydrographic and transport characteristics, in reasonable agreement with the observations (see Sec. 5.2). When descending along the continental slope of the IB, the ISOW of the three models mixes with local waters that are generally moderately warmer and saltier than the observations.

Because of the step-like bottom topography, the ISOW of the GOSI9-z^*ps model experiences large spurious mixing while flowing down the IB. As a result, the GOSI9-z^*ps simulation reproduces an IB overflow that is not dense enough ($\sigma_\theta < 27.84\ kg\,m^{-3}$) to penetrate at depth and remains confined in a narrow part of the east side of the RR (Fig. 12b, f and j, Fig. 13b and f and Tab. 3).

In contrast, the smooth representation of the ocean floor typical of the GOSI9-MEs model significantly reduce the undesired numerical mixing during the dense plume descent. As a consequence, when the ISOW of the GOSI9-MEs model entrains the relatively warm and salty waters of the IB, the result is an overflow that is in good agreement with the observations for temperature but is slightly saltier and hence denser than the measurements (Fig. 12d, h and l, Fig. 13d and h and Tab. 3).

The GOSI9-szt simulation represents an intermediate solution, where numerical mixing is partially reduced in comparison to the GOSI9-z^*ps model but is still too large to retain a dense modified ISOW similar to the observations (Fig. 12c, g and k, Fig. 13c and g and Tab. 3). Interestingly, the GOSI9-szt model seems to be able to mitigate the salinity bias affecting the ISOW of the GOSI9-MEs simulation. This is probably a compensation error rather than a model improvement due to the higher numerical mixing affecting the GOSI9-szt model below the 1200 m, as indicated by Fig. 12k and l, Fig. 13g and h and Fig. 14f.

The DSOW simulated by the three models in the proximity of the Greenland-Scotland ridge presents significant positive temperature and salinity biases, that are compensated in terms of buoyancy, resulting in an overflow density very similar to the observations (Fig. 11$a.^*$, $b.^*$, $c.^*$ and $d.^*$ and Tab. 2).

In the GOSI9-z^*ps simulation, the excessive numerical diapycnal mixing seems to seriously affect the properties of the dense descending plume. As a result, a relatively light modified DSOW that does not reach the bottom of the IS is created - see the salty plume with $\sigma_\theta < 27.84\ kg\,m^{-3}$ that spreads at its neutrally buoyant level in Fig. 14j isolating the relatively fresh water mass at the bottom. Consequently, the mid depth flowing modified DSOW mixes with the relatively warm and salty modified ISOW circulating in the IS in the same depth range (see Fig. 15a). This can be observed in the peak in transport shown in Fig. 10a for densities between 27.80 $kg\,m^{-3}$ and 27.85 $kg\,m^{-3}$ and the large positive active tracers biases of Fig. 13 between $1500-2000$ m along the continental slope of Greenland.

In the GOSI9-MEs experiment, the cascading DSOW experiences significantly reduced numerical mixing and entrains the relatively cold and salty modified ISOW flowing in the IS at depths between $1500-2500$ m - see, for example, the propagation paths of the cold and salty anomalies with respect to GOSI9-z^*ps and GOSI9-szt models presented in Fig. 14b and e and Fig. 14c and f, respectively. As a result, a modified DSOW with an average σ_θ in good agreement with the observations that reaches the bottom of the IS is created, as shown in Fig. 12d and Tab. 3. Because of the hydrographic biases already affecting the DSOW upstream, improvements in temperature at the bottom of the IS in comparison to the other two models are small (Fig. 14b and c), while salinity errors are slightly more pronounced (Fig. 14e and f).

Also in the IS the GOSI9-szt solution represents a hybrid between the GOSI9-z^*ps and GOSI9-MEs simulations - see for example the temperature and salinity anomalies with respect to GOSI9-z^*ps (Fig. 14a and d) and GOSI9-MEs (Fig. 14c and f) simulations. Since numerical mixing is reduced only at depths shallower than 1200 m, the GOSI9-szt model simulates a modified DSOW with $\sigma_\theta > 27.84\ kg\,m^{-3}$, but one that is not dense enough to reach the bottom of the IS, therefore spreading laterally at its neutral buoyancy level and isolating the relatively cold and fresh water of the initial condition as in the GOSI9-z^*ps case (see Fig. 12c, g, and k).

Finally, our results show that the impact of changing the vertical coordinate system seems to extend beyond the boundaries of the localisation area, affecting also the hydrographic properties of the DWBC in the Labrador Sea and along the eastern continental slope of North America as indicated by Fig. 14.

In summary, the following main points result from our analysis:

- The three models present similar temperature and salinity biases that compensate in buoyancy;
- Biases affecting the modified ISOW seem to play an important role in pre-conditioning the overflow biases in the IS;
- The GOSI9-MEs model is able to reduce the spurious mixing and retain the dense overflow signal at depth, as expected. However, as a result tracers biases at the bottom are exacerbated in the GOSI9-MEs simulation, especially for the case of salinity;
- In the GOSI9-z^*ps and GOSI9-szt experiments the large numerical mixing combines with models biases to generate modified ISOW and DSOW water masses that are too warm and not dense enough but at the same time not as saline as the ones of the GOSI9-MEs simulation, especially at the bottom;
- The impact of using local-GVC in the Nordic Seas overflow region extends to the entire subpolar gyre.

6 Conclusions and perspectives

A simple methodology to smoothly blending between different type of quasi-Eulerian generalised vertical coordinates in the horizontal direction is introduced. We refer to it as *localisation* method, since it allows one to change the type of vertical coordinate system in arbitrarily chosen time-invariant localised areas of numerical ocean models. The result is a quasi-Eulerian coordinate system that is hybrid in the horizontal direction, similar to how some coordinates are hybrid in the vertical. One of the main aims of the *localisation* method proposed in this study is to improve the ocean models' representation of the important influence the bottom topography exerts on the oceanic flow.

After detailing the characteristics of the novel method, in this study we test its ability to improve the Nordic Seas overflows representation in a NEMO-based eddy-permitting global ocean configuration. Three state-of-the-art z^*-coordinate, with partial steps (z^*ps), models localising different types of terrain-following vertical coordinates in the proximity of the Greenland-Scotland ridge are compared against a control employing z^*ps levels everywhere. The quasi-Eulerian vertical coordinates tested in the Greenland-Scotland ridge localisation area are the vanishing quasi-sigma (vqs), the hybrid sz-transitioning (szt) or the multi-envelope s (MEs) coordinates.

Two idealised numerical experiments and a realistic 10-years long simulation are conducted. The idealised experiments aim at assessing the ability of the models to accurately compute horizontal pressure forces and reduce spurious diapycnal mixing when simulating dense water cascading down the steep continental slope of the Irminger Sea.

The realistic runs seek to evaluate the models' skill in reproducing observed hydorgraphic and transport properties of the Nordic overflows.

Numerical experiments indicate that the localisation approach proposed in this study can be successfully used to embed terrain-following levels in a global ocean configuration otherwise using quasi-Eulerian geopotential-based vertical coordinates, provided that the localised terrain-following coordinate system chosen is flexible enough to allow a smooth transition between the two (as in the MEs and szt cases, for example). In particular, the vqs approach seems to be not suitable for our localisation methodology, at least in the configuration proposed in this study (i.e., vqs embedded in z^*ps) - the same conclusion should apply to classical σ-coordinates, being a special case of vqs coordinates.

The Nordic overflow test-case shows that localising terrain-following MEs coordinates in the Greenland-Scotland ridge region allows important reduction of spurious cross-isopycnal mixing when modeling bottom intensified buoyancy driven currents, significantly improving the realism of Nordic overflows simulations in comparison to the models using z^*ps or szt coordinates, especially in term of density and transport. The impact of changing vertical grid propagates well beyond the boundaries of the Greenland-Scotland ridge localisation area, extending to the entire subpolar gyre, demonstrating the robustness and efficacy of the localisation method.

Important hydrographic biases similarly affect all the realistic experiments. In the case of models using geopotential-based levels at depth, the large numerical mixing results in a secondary compensating effect that mitigates the models' biases at the bottom, especially for salinity. To the contrary, the ability of the model using local-MEs levels to importantly reduce spurious mixing exacerbates the salinity biases at the bottom. These results indicate that the Nordic region of our eddy-permitting global configuration is affected by biases that can not be mitigated using a vertical grid targeting the local leading processes, especially in the case of salinity. Other studies have reported important salinity biases affecting NEMO-based simulations of the North Atlantic subpolar gyre (e.g., Treguier et al. (2005); Rattan et al. (2010); Marzocchi et al. (2015)). A special North Atlantic process evaluation group (NatlPEG) involving the UK Met Office and National Oceanography Centre is currently investigating possible large scale causes behind those biases.

The localisation method proposed in this paper is general, in the sense that can be easily applied to any region of any quasi-Eulerian model domain. For example, applications to improve the representation of boundary currents and the shelf dynamics in global ocean configurations are currently being tested. Similarly, the localisation method is also being implemented with promising results in a regional set-up to embed MEs coordinates in a model using vqs levels for improving the shelf dynamics.

Finally, possible future developments include using the localisation method to make it easier changing type of vertical grid in AGRIF (Debreu et al., 2008, 2012) nests or combining a local-MEs coordinate system with the Brinkman penalisation approach (Debreu et al., 2020), considering that both methods rely on the definition of envelope(s) of the bottom topography.

Appendix A A Simple algorithm for defining transition areas

Let us consider a model domain with horizontal coordinates x and y. A generic localisation area Λ can be defined by an indicator function $\mathbb{1}_\Lambda(x, y)$,

$$\mathbb{1}_\Lambda(x,y) = \begin{cases} 1 & \text{if } (x,y) \in \Lambda, \\ 0 & \text{otherwise.} \end{cases} \tag{A1}$$

Then, the generic transition area T encircling the localisation area Λ is computed in this study according to the following algorithm:

$B = J + \gamma(J - \mathbb{1}_\Lambda)$ // $B(x, y)$ is 1 if $(x, y) \in \Lambda$, $1 + \gamma$ if not;
$W = B$;
$n = 0$;
while $n \leq n_{iter}$ **do**
  $\overline{W} = G \star W$;
  $W = \mathbb{1}_\Lambda + (J - \mathbb{1}_\Lambda) \circ \overline{W}$ // $W(x, y)$ is 1 if $(x, y) \in \Lambda$, $\overline{W}(x, y)$ if not;
  $n+ = 1$;
end
$D = |W - B|$;

where $J(x, y) = 1$, $\gamma = 1.0 \times 10^{-10}$ is a tunable coefficient, n is the iterator variable, n_{iter} is the user-defined maximum number of iterations, $G(x_0, y_0, \sigma_G, x, y)$ is a two-dimensional spatial Gaussian filter with σ_G the user-defined width of the filter and $\circ$ describing the Hadamard product (e.g., Horn & Johnson (1985)). The value of a the filtered function $\overline{W}(x, y)$ after the Gaussian low-pass filtering operation $G \star W$ at a point(x_0, y_0) is given by

$$\overline{W}(x_0, y_0) = G \star W = \iint W(x, y)\, G(x_0, y_0, \sigma_G, x, y)\, dx\, dy \tag{A2}$$

$$= \frac{1}{2\pi\sigma_G^2} \iint W(x, y)\, \exp\Big\{ -\frac{(x - x_0) + (y - y_0)}{2\sigma_G^2} \Big\}\, dx\, dy \tag{A3}$$

The transition area T is then defined by the indicator function $\mathbb{1}_T(x, y)$,

$$\mathbb{1}_T(x, y) = \begin{cases} 1 & \text{if } D(x, y) > 0 \\ 0 & \text{otherwise.} \end{cases} \tag{A4}$$

In this work, the transition area is generated using $\sigma_G = 1$ and $n_{iter} = 1$.

Appendix B Quasi-Eulerian coordinates transformations

This section describes the QE GVCs implemented in this study. While here we focus on the details of the analytical coordinate transformations, it is worth mentioning that the NEMO model implements QE GVCs defining discrete model levels with respect to an unperturbed ocean at rest (i.e., $\mathbf{u} = 0$, $\eta = 0$) and then uses the variable volume layer algorithm of Levier et al. (2007) to evolve h_k according to equation 4 with $\alpha_k \propto h_k^0 H^{-1}$.

B1 z^*-coordinate

The NEMO implementation of the z^*-coordinate transformation follows Stacey et al. (1995) and Adcroft & Campin (2004):

$$z = \eta + z^* \frac{H + \eta}{H}, \tag{B1}$$

with $z^*(z = \eta) = 0$ and $z^*(z = -H) = -H$ (see Fig. 3b and Fig. B1a).

B2 vqs-coordinate

The standard NEMO v4.0.4 implementation of vqs coordinates is used in this study (see Fig. 3c and Fig. B1b), which combines modified versions of the QE GVCs originally proposed by Dukhovskoy et al. (2009) and Song & Haidvogel (1994):

$$z = \eta\Big[1 + \frac{h_c}{H_e}\sigma + \Big(1 - \frac{h_c}{H_e}\Big)C(\sigma)\Big] + h_c\sigma + C(\sigma)(H_e - h_c), \tag{B2}$$

where $\sigma(z = \eta) = 0$ and $\sigma(z = -H_e) = -1$, $C(\sigma)$ is the Song & Haidvogel (1994) stretching function, H_e is a smooth envelope bathymetry (positive downward and such that $H_e \geq H$) and h_c is the depth at which the transition from stretched to uniform distributed levels occurs. Equation B2, differently from the original s-coordinates of Song & Haidvogel (1994), ensures that α_k of equation 4 is a function of h_k^0 and the total model depth H_e.

A similar set-up to Colombo (2018) is applied for localising vqs levels in the Nordic overflows area, using $\theta = 6.0$ and $b = 0.7$ and $h_c = 50$.

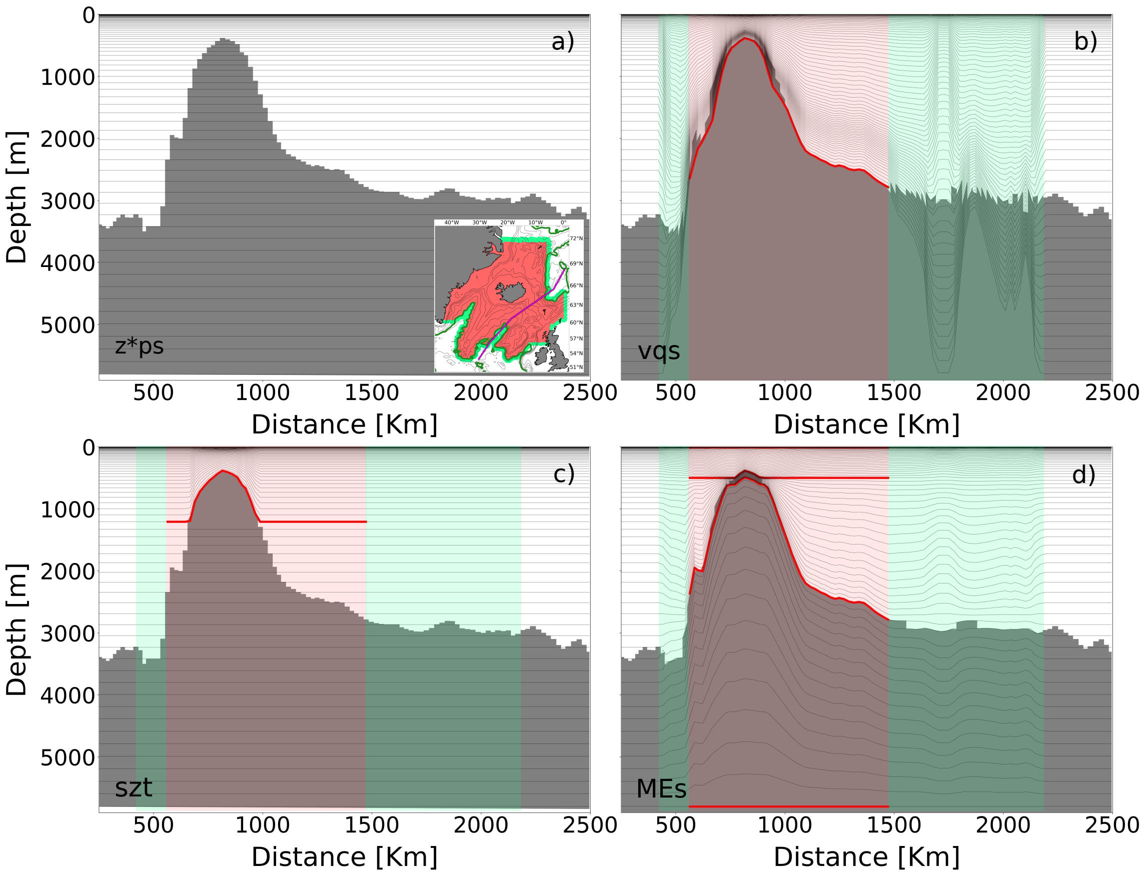

Figure B1. Panel a) shows the model bathymetry cross-section extracted from the GOSI9-z^*ps model, panel b) from the GOSI9-vqs model while panel c) and d) from the GOSI9-szt and GOSI9-MEs models, respectively. In the inset in panel a), the red and green regions represent the Nordic overflows localisation and transition areas used in this study, respectively, the blue line shows the location of the model bathymetry cross-sections presented in the other panels while the green line marks the 2800 m isobath. In panels a) to d) the red lines shows the location of the envelopes used to configure the localised GVCs.

B3 szt-coordinate

The szt scheme described in Wise et al. (2021) allows one to combine vqs and z^*ps QE coordinates (see Fig. 3d and Fig. B1c). The szt analytical formulation reads

$$z = \begin{cases} \eta\Big[1 + \frac{\tilde{h}_c}{H_e}\sigma + \Big(1 - \frac{\tilde{h}_c}{H_e}\Big)Z(\sigma)\Big] + \tilde{h}_c\sigma + Z(\sigma)(H_e - \tilde{h}_c) & \text{for } H \leq H_t, \\ \eta + z^*\frac{H+\eta}{H} & \text{for } H > H_t, \end{cases} \tag{B3}$$

where H_t is the depth at which the transition from vqs to $z*$ coordinates occurs, H_e is a smooth envelope bathymetry with maximum depth H_t and $\sigma(z = \eta) = 0$, $\sigma(z = -H_t) = -1$, $z^*(z = \eta) = 0$ and $z^*(z = -H) = -H$. The standard NEMO formulation for vqs-coordinates (B2) is modified by replacing $C(\sigma)$ with $Z(\sigma)$, a stretching function consistent with the one of Madec et al. (1996)), and using the variable $\tilde{h}_c$ defined as

$$\tilde{h}_c = \min\left\{\max\left\{\frac{H_e - H_t}{1 - \frac{H_t}{h_c}}, 0\right\}, h_c\right\}. \tag{B4}$$

When discretising, the smoothness of h_k is retained by ensuring that discrete vqs and z^* levels are distributed along the water column according to a consistent stretching function.

In practise, the following algorithm is used to generate a szt grid. At first, the k_t z^*-level at which the transition will occur is chosen (in the case of this paper, $k_t = 48$). Then, a standard z^*ps vertical grid is generated. After, an envelope bathymetry H_e with maximum depth $H_t = \max\{z_{k_t}\}$ is computed and used to recompute the depth of all the discrete model levels with $k < k_t$.

B4 MEs-coordinate

The ME method of Bruciaferri et al. (2018) defines n arbitrary depth surfaces $H_e^i(x, y, t)$ (downward positive) called *envelopes* (with $1 \leq i \leq n$) to divide the ocean model vertical domain into n sub-zones D_i, each one bounded by envelopes H_e^{i-1} at the top and H_e^i at the bottom (with $H_e^0 = -\eta$). Each envelope moves with the free surface according to

$$H_e^i = H_{e_0}^i - \eta\Big(1 - \frac{H_{e_0}^i}{H_b}\Big), \tag{B5}$$

where $H_{e_0}^i(x, y)$ is the depth with respect to an unperturbed ocean at rest and $H_b = H_{e_0}^n \geq H$.

ME s-coordinates are implemented in the Greenland-Scotland ridge local area using four envelopes and the following coordinate transformation (see Fig. 3e and Fig. B1d):

$$z\big|_{D_i} = \begin{cases} C_i(\sigma_i)(H_e^i - H_e^{i-1} - h_c^i) - H_e^{i-1} + h_c^i\sigma_i + \eta\beta_i & \text{if } i \in \{1, 3\}, \\ P_{x,y,i}^3(\sigma_i)\Big(1 + \frac{\eta}{H_b}\Big) & \text{if } i \in \{2, 4\}, \end{cases} \tag{B6}$$

where $\sigma_i(z = -H_e^{i-1}) = 0$ and $\sigma_i(z = -H_e^i) = -1$, $C_i(\sigma_i)$ is a generic stretching function applied in sub-zone D_i and h_c^i is the depth at which the transition from stretched to uniform distributed levels occurs. The term β_i, defined as

$$\beta_i = \frac{h_c^i}{H_b}\sigma_i - \frac{h_c^i}{H_b}C_i(\sigma_i),$$

ensures that α_k of equation 4 is a function of h_k^0 and the total model depth H_b. The function $P^3_{x,y,i}(\sigma_i)$ represents a complete cubic spline whose coefficients are computed ensuring the monotonicity and continuity of the Jacobian of the transformation for the case of an unperturbed ocean at rest (see Bruciaferri et al. (2018) for the details).

In this study we set $h_c^i = 0$ while the Song & Haidvogel (1994) stretching functions $C_1(\sigma_1)$ and $C_3(\sigma_3)$ use $\theta_1 = 1.2$, $b_1 = 0.7$ and $\theta_3 = 2.4$, $b_3 = 0.85$, respectively. The first envelope $H^1_{e_0}$ has depth equal to 10 m, so that the upper sub-zone D_1 can be discretised with a constant high resolution consistent with the global z^*ps grid. Envelope $H^2_{e_0}$ follows a smoothed version of the bottom topography H from a minimum depth of 40 m to a maximum depth of 500 m: in this way, sub-zone D_2 can use nearly terrain-following levels where $40\ m \leq H \leq 500\ m$ to better resolve shelf cascading, while elsewhere can employ z^*-like interfaces to minimise HPG errors; Similarly, the envelope $H^3_{e_0}$ follows the smoothed model bathymetry in areas where $610\ m \leq H \leq 2800\ m$, resulting in terrain-following levels only in areas where the bottom topography is in this depth range to improve overflows simulations. The bottom geopotential envelope $H^4_{e_0}$ targets the depth of last W-level of the global z^*ps grid, so that model levels near the bottom can smoothly transition from the local to the global grid. Envelopes $H^2_{e_0}$ and $H^3_{e_0}$ are smoothed using the iterative algorithm described in Appendix C.

Once the envelopes have been identified based on physical motivations, local ME s-coordinates are discretised assigning to each layers D_i a number of levels which is largely dictated by the number of levels possessed by the global z^*ps grid at a similar depth range. For example, in this study 9 levels are used in layer D_1, 31 in D_2, 20 in D_3 and 15 in D_4.

Appendix C Iterative algorithm for smoothing envelopes surfaces

The iterative algorithm applied in this study to smooth the envelopes of vqs, szt and MEs models relies on the Martinho & Batteen (2006) smoothing procedure to ensure that the local slope parameter r (see Sec. 3.2 for its definition) is smaller than a user defined threshold r_{max}.

Figure C1 summarises the main steps of our iterative algorithm. At first, the envelopes of the three GVCs were smoothed by applying the Martinho & Batteen (2006) method with an $r_{max} = 0.12$. After, for each of the GVCs, a series of idealised HPG tests with a set-up similar to the one described in Sec. 4.1 were run: at each iteration, the envelopes were smoothed with an increasingly more severe r_{max} only in those grid points where HPG errors exceeded 0.05 $m\ s^{-1}$ (see text of steps 4, 5 and 6 of Fig. C1 for the details). This value was chosen following Wise et al. (2021), that showed that optimising the envelopes of a ME system to have HPG error $< 0.05\ m\ s^{-1}$ can significantly improve the accuracy of a terrain-following shelf model of the North West European shelf with a lateral resolution of 7 km. In this work, three iterations of the iterative smoothing algorithm were applied to generate the envelopes used to implement the localised GVCs described in Sec. 3.2.

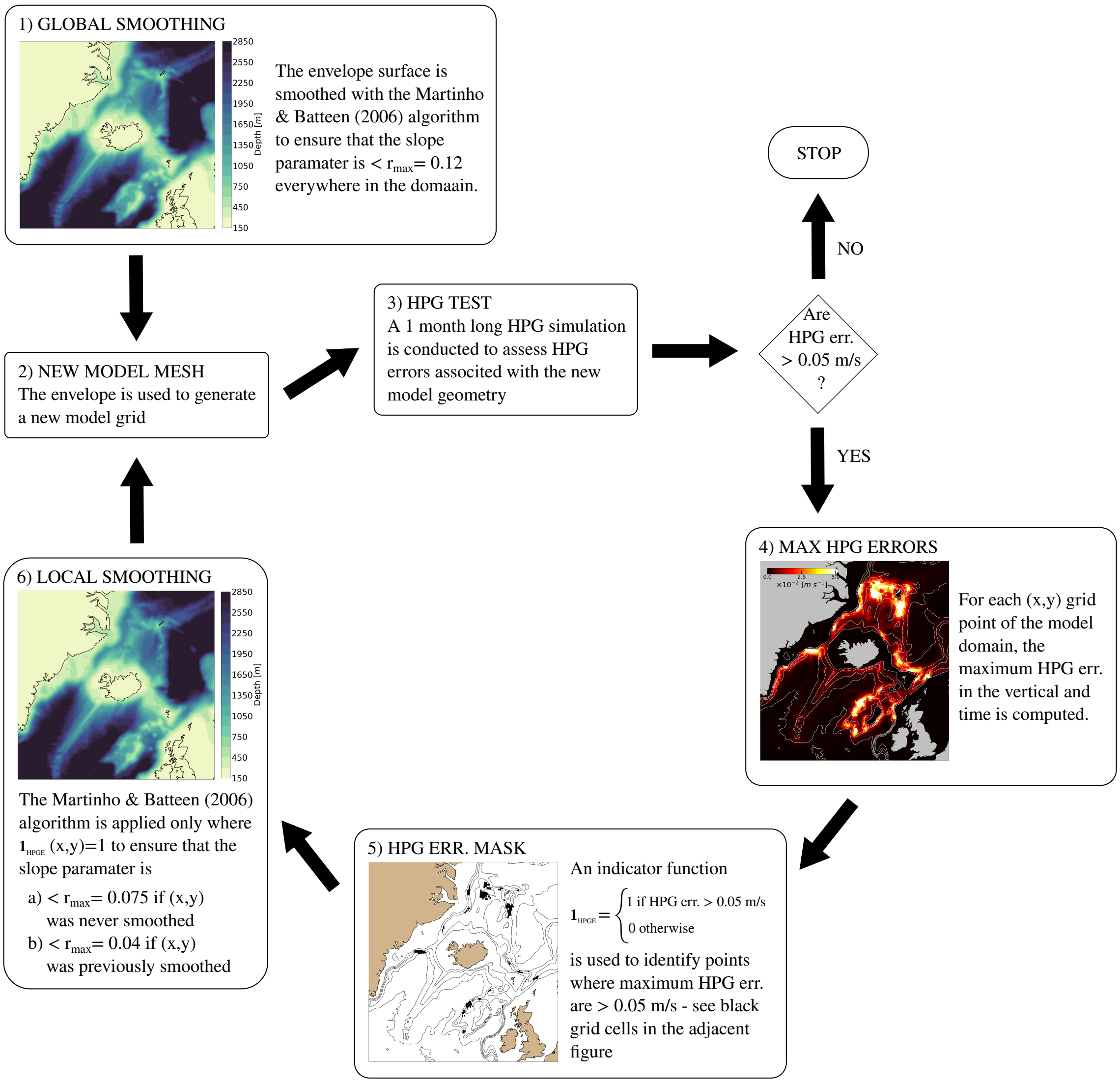

Figure C1. Main steps of the iterative smoothing algorithm applied in this study to smooth the envelopes of vqs, *szt* and ME*s* models.

Appendix D List of acronyms

Table D1 is a list of acronyms to assist cross-referencing abbreviations used in the paper.

Acronym	Meaning
Vertical Coordinates	
GVC	Generalised vertical coordinate
QE	quasi-Eulerian
QL	quasi-Lagrangian
ALE	Arbitrary Lagrangian Eulerian
z^*ps	z^*-coordinates with partial steps
vqs	Vanishing quasi-sigma
szt	Hybrid sz-transitioning
MEs	Multi-Envelope s-coordinates
Water masses and currents	
AMOC	Atlantic Meridional Overturning Circulation
DSOW	Denmark Strait Overflow Water
ISOW	Iceland-Scotland Overflow Water
NAW	North Atlantic Water
DWBC	Deep Western Boundary Current
Numerical models	
GOSI9-025	GOSI9 global ocean configuration at 1/4° of horizontal resolution
GOSI9-z^*ps	standard GOSI9-025 configuration using z^*ps everywhere
GOSI9-vqs	GOSI9-025 configuration using vqs levels in the Greenland-Scotland ridge area
GOSI9-szt	GOSI9-025 configuration using szt levels in the Greenland-Scotland ridge area
GOSI9-MEs	GOSI9-025 configuration using MEs levels in the Greenland-Scotland ridge area
Observational datasets	
OSNAP	Overturning in the Subpolar North Atlantic Program
WOA18	World Ocean Atlas 2018
DS	Denmark Strait cross-section
IS	Irminger sea portion of the eastern leg of the OSNAP cross-section
IB	Icelandic basin portion of the eastern leg of the OSNAP cross-section
IFR	Iceland-Faroe ridge cross-section
FSC	Faroe-Shetland channel cross-section
FBC	Faroe-Bank channel cross-section
WTR	Wyville-Thomson ridge cross-section
CFGZ	Charlie-Gibbs Fracture Zone cross-section
Miscellaneous	
NEMO	Nucleus for European Modelling of the Ocean
HPG	Horizontal pressure gradient

Table D1. List of acronyms used in the paper.

Appendix E Open Research

The four models compared in this study are based on the NEMO ocean model code, which is freely available from the NEMO website (`https://www.nemo-ocean.eu`, last access: 19 June 2023). The code to localise quasi-Eulerian general vertical coordinates used in this study is included in the NEMO v4.2 trunk. Additional modifications to the NEMO original code are required for running GOSI9-based configurations. The actual NEMO v4.0.4 source code and the namelists used to run the integrations presented in this manuscript are available at `https://zenodo.org/record/8056285` and `https://zenodo.org/record/8055445`.

The data that comprise the GOSI9-z^*ps, GOSI9-vqs, GOSI9-szt and GOSI9-MEs simulations are of the order of tens of TB. However, the data can be made available by contacting the authors.

The data describing the geometry of the four models and the derived output data used for the analyses and plots included in this manuscript are available at `https://zenodo.org/record/8055023` while the actual code to reproduce the analysis and the plots can be found at `https://github.com/JMMP-Group/loc_gvc-GO_ovf` and `https://github.com/JMMP-Group/nordic-seas-validation`.

Acknowledgments

Funding support for DB, CG and HH was provided by the Joint DECC/Defra Met Office Hadley Centre Climate Programme (GA01101), UK Ministry of Defense and the UK Public Weather Service. JH and MA were supported by the H2020 European Institute of Innovation and Technology (IMMERSE) grant no. 821926. The authors would like to thank Mike Bell, Dave Storkey, Nigel Wood and Jérome Chanut for helpful and constructive discussions, suggestions and advice. Numerical simulations and analysis were carried out on the Cray HPC at the Met Office, UK.

References

Adcroft, A., Anderson, W., Balaji, V., Blanton, C., Bushuk, M., Dufour, C. O., ... Zhang, R. (2019, oct). The GFDL Global Ocean and Sea Ice Model OM4.0: Model Description and Simulation Features. *Journal of Advances in Modeling Earth Systems*, *11*(10), 3167–3211. Retrieved from `https://onlinelibrary.wiley.com/doi/10.1029/2019MS001726` doi: 10.1029/2019MS001726

Adcroft, A., & Campin, J.-M. (2004, jan). Rescaled height coordinates for accurate representation of free-surface flows in ocean circulation models. *Ocean Modelling*, *7*(3-4), 269–284. Retrieved from `http://linkinghub.elsevier.com/retrieve/pii/S1463500303000544` doi: 10.1016/j.ocemod.2003.09.003

Adcroft, A., & Hallberg, R. (2006, jan). On methods for solving the oceanic equations of motion in generalized vertical coordinates. *Ocean Modelling*, *11*(1-2), 224–233. Retrieved from `https://linkinghub.elsevier.com/retrieve/pii/S1463500305000090` doi: 10.1016/j.ocemod.2004.12.007

Beckers, J. M., Gregoire, M., Nihoul, J. C. J., Stanev, E., Staneva, J., & Lancelot, C. (2002). Modelling the Danube-influenced North-western Continental Shelf of the Black Sea. I: Hydrodynamical Processes Simulated by 3-D and Box Models. *Estuarine, Coastal and Shelf Science*, *54*(3), 453–472. Retrieved from `http://www.sciencedirect.com/science/article/pii/S0272771400906589` doi: 10.1006/ecss.2000.0658

Bleck, R. (1978, sep). On the Use of Hybrid Vertical Coordinates in Numerical Weather Prediction Models. *Monthly Weather Review*, *106*(9), 1233–1244. Retrieved from `http://journals.ametsoc.org/doi/10.1175/1520-0493(1978)106%3C1233:OTUOHV%3E2.0.CO;2` doi: 10.1175/1520-0493(1978)106⟨1233:OTUOHV⟩2.0.CO;2

Bleck, R. (2002, jan). An oceanic general circulation model framed in hybrid isopycnic-Cartesian coordinates. *Ocean Modelling*, *4*(1), 55–88. Retrieved from `http://www.sciencedirect.com/science/article/pii/S1463500301000129https://linkinghub.elsevier.com/retrieve/pii/S1463500301000129` doi: 10.1016/S1463-5003(01)00012-9

Boyer, T. P., Garcia, H. E., Locarnini, R. A., Zweng, M. M., Mishonov, A. V., Reagan, J. R., ... Smolyar, I. V. (2018). *World Ocean Atlas 2018* (Tech. Rep.). NOAA National Centers for Environmental Information. Dataset. Retrieved from `https://www.ncei.noaa.gov/archive/accession/NCEI-WOA18`

Bruciaferri, D., Shapiro, G., Stanichny, S., Zatsepin, A., Ezer, T., Wobus, F., ... Hilton, D. (2020, feb). The development of a 3D computational mesh to improve the representation of dynamic processes: The Black Sea test case. *Ocean Modelling*, *146*, 101534. Retrieved from `https://linkinghub.elsevier.com/retrieve/pii/S1463500319301593` doi: 10.1016/j.ocemod.2019.101534

Bruciaferri, D., Shapiro, G. I., & Wobus, F. (2018, oct). A multi-envelope vertical coordinate system for numerical ocean modelling. *Ocean Dynamics*, *68*(10), 1239–1258. Retrieved from `http://link.springer.com/10.1007/s10236-018-1189-x` doi: 10.1007/s10236-018-1189-x

Bruciaferri, D., Tonani, M., Ascione, I., Al Senafi, F., O'Dea, E., Hewitt, H. T., &

Saulter, A. (2022, dec). GULF18, a high-resolution NEMO-based tidal ocean model of the Arabian/Persian Gulf. *Geoscientific Model Development*, *15*(23), 8705–8730. Retrieved from https://gmd.copernicus.org/articles/15/8705/2022/ doi: 10.5194/gmd-15-8705-2022

Burchard, H., Petersen, O., & Petersen, O. (1997, nov). Hybridization between σ- and z-co-ordinates for improving the internal pressure gradient calculation in marine models with steep bottom slopes. *International Journal for Numerical Methods in Fluids*, *25*(9), 1003–1023. Retrieved from https://onlinelibrary.wiley.com/doi/10.1002/(SICI)1097-0363(19971115)25:9%3C1003::AID-FLD600%3E3.0.CO;2-E doi: 10.1002/(SICI)1097-0363(19971115)25:9⟨1003::AID-FLD600⟩3.0.CO;2-E

Colombo, P. (2018). *Modelling dense water flows through sills in large scale realistic ocean models: demonstrating the potential of a hybrid geopotential/terrain-following vertical coordinate* (Doctoral dissertation, Université Grenoble Alpes). Retrieved from http://www.theses.fr/2018GREAU017

Colombo, P., Barnier, B., Penduff, T., Chanut, J., Deshayes, J., Molines, J.-M., ... Treguier, A.-M. (2020, jul). Representation of the Denmark Strait overflow in a z-coordinate eddying configuration of the NEMO (v3.6) ocean model: resolution and parameter impacts. *Geoscientific Model Development*, *13*(7), 3347–3371. Retrieved from https://gmd.copernicus.org/articles/13/3347/2020/ doi: 10.5194/gmd-13-3347-2020

Debreu, L., Kevlahan, N.-R., & Marchesiello, P. (2020, jan). Brinkman volume penalization for bathymetry in three-dimensional ocean models. *Ocean Modelling*, *145*, 101530. Retrieved from https://linkinghub.elsevier.com/retrieve/pii/S146350031930174X doi: 10.1016/j.ocemod.2019.101530

Debreu, L., Marchesiello, P., Penven, P., & Cambon, G. (2012, jun). Two-way nesting in split-explicit ocean models: Algorithms, implementation and validation. *Ocean Modelling*, *49-50*, 1–21. Retrieved from https://linkinghub.elsevier.com/retrieve/pii/S1463500312000480 doi: 10.1016/j.ocemod.2012.03.003

Debreu, L., Vouland, C., & Blayo, E. (2008, jan). AGRIF: Adaptive grid refinement in Fortran. *Computers & Geosciences*, *34*(1), 8–13. Retrieved from https://linkinghub.elsevier.com/retrieve/pii/S009830040700115Xhttp://linkinghub.elsevier.com/retrieve/pii/S009830040700115X doi: 10.1016/j.cageo.2007.01.009

Dickson, R. R., & Brown, J. (1994). The production of North Atlantic Deep Water: Sources, rates, and pathways. *Journal of Geophysical Research*, *99*(C6), 12319. Retrieved from http://doi.wiley.com/10.1029/94JC00530 doi: 10.1029/94JC00530

Dickson, R. R., Meincke, J., & Rhines, P. (Eds.). (2008). *ArcticSubarctic Ocean Fluxes*. Dordrecht: Springer Netherlands. Retrieved from http://link.springer.com/10.1007/978-1-4020-6774-7 doi: 10.1007/978-1-4020-6774-7

Dukhovskoy, D. S., Morey, S. L., Martin, P. J., O'Brien, J. J., & Cooper, C. (2009). Application of a vanishing, quasi-sigma, vertical coordinate for simulation of high-speed, deep currents over the Sigsbee Escarpment in the Gulf of Mexico. *Ocean Modelling*, *28*(4), 250–265. Retrieved from http://dx.doi.org/10.1016/j.ocemod.2009.02.009 doi: 10.1016/j.ocemod.2009.02.009

Ezer, T. (2005, jan). Entrainment, diapycnal mixing and transport in three-dimensional bottom gravity current simulations using the MellorYamada turbulence scheme. *Ocean Modelling*, *9*(2), 151–168. Retrieved from http://linkinghub.elsevier.com/retrieve/pii/S1463500304000368 doi: 10.1016/j.ocemod.2004.06.001

Ezer, T. (2006). Topographic influence on overflow dynamics: Idealized numerical simulations and the Faroe Bank Channel overflow. *Journal of Geophysical Research*, *111*(C2), C02002. Retrieved from http://doi.wiley.com/10.1029/

2005JC003195 doi: 10.1029/2005JC003195

Ezer, T. (2016, aug). Revisiting the problem of the Gulf Stream separation: on the representation of topography in ocean models with different types of vertical grids. *Ocean Modelling*, *104*, 15–27. Retrieved from http://linkinghub.elsevier.com/retrieve/pii/S1463500316300397 doi: 10.1016/j.ocemod.2016.05.008

Ezer, T., Arango, H., & Shchepetkin, A. F. (2002). Developments in terrain-following ocean models: Intercomparisons of numerical aspects. *Ocean Modelling*, *4*(3-4), 249–267. doi: 10.1016/S1463-5003(02)00003-3

Ezer, T., & Mellor, G. L. (2004, jan). A generalized coordinate ocean model and a comparison of the bottom boundary layer dynamics in terrain-following and in z-level grids. *Ocean Modelling*, *6*(3-4), 379–403. Retrieved from https://linkinghub.elsevier.com/retrieve/pii/S146350030300026X doi: 10.1016/S1463-5003(03)00026-X

Gibson, A. (2019). *An adaptive vertical coordinate for idealised and global ocean modelling* (Doctoral dissertation, The Australian National University). doi: 10.25911/5f58b0768dafb

Good, S. A., Martin, M. J., & Rayner, N. A. (2013, dec). EN4: Quality controlled ocean temperature and salinity profiles and monthly objective analyses with uncertainty estimates. *Journal of Geophysical Research: Oceans*, *118*(12), 6704–6716. Retrieved from http://doi.wiley.com/10.1002/2013JC009067 doi: 10.1002/2013JC009067

Griffies, S. M. (2004). *Fundamentals of Ocean Climate Models.* Princeton, NJ: Princeton University Press.

Griffies, S. M. (2012). *Elements of the modular ocean model (MOM): 2012 release (GFDL Ocean Group Technical Report No. 7)* (Tech. Rep.). Princeton, USA: NOAA/Geophysical Fluid Dynamics Laboratory.

Griffies, S. M., Adcroft, A., & Hallberg, R. W. (2020, oct). A Primer on the Vertical LagrangianRemap Method in Ocean Models Based on Finite Volume Generalized Vertical Coordinates. *Journal of Advances in Modeling Earth Systems*, *12*(10). Retrieved from https://onlinelibrary.wiley.com/doi/10.1029/2019MS001954 doi: 10.1029/2019MS001954

Griffies, S. M., Böning, C., Bryan, F. O., Chassignet, E. P., Gerdes, R., Hasumi, H., … Webb, D. (2000). Developments in ocean climate modelling. *Journal of Computational Physics*, *2*(3-4), 123–192. doi: 10.1016/S1463-5003(00)00014-7

Griffies, S. M., Gnanadesikan, A., Pacanowski, R. C., Larichev, V. D., Dukowicz, J. K., & Smith, R. D. (1998). Isoneutral Diffusion in a z-Coordinate Ocean Model. *Journal of Physical Oceanography*, *28*(5), 805–830. doi: 10.1175/1520-0485(1998)028⟨0805:IDIAZC⟩2.0.CO;2

Griffies, S. M., Pacanowski, R. C., & Hallberg, R. W. (2000, mar). Spurious Diapycnal Mixing Associated with Advection in a z -Coordinate Ocean Model. *Monthly Weather Review*, *128*(3), 538–564. doi: 10.1175/1520-0493(2000)128⟨0538:SDMAWA⟩2.0.CO;2

Guiavarc'h, C., Storkey, D., Blaker, A., Blockley, E., Megann, A., Hewitt, H., … Ann, B. (2023). GOSI9: UK Global Ocean and Sea Ice configurations. *to be submitted to Geoscientific Model Development*.

Guo, C., Ilicak, M., Bentsen, M., & Fer, I. (2016, aug). Characteristics of the Nordic Seas overflows in a set of Norwegian Earth System Model experiments. *Ocean Modelling*, *104*, 112–128. Retrieved from https://linkinghub.elsevier.com/retrieve/pii/S1463500316300543 doi: 10.1016/j.ocemod.2016.06.004

Haidvogel, D., & Beckmann, A. (1999). *Numerical Ocean Circulation Modeling.* Imperial College Press. doi: 10.2277/0521781825

Haney, R. L. (1991). On the pressure gradient force over steep topography in sigma coordinate ocean models. *Journal of Physical Oceanography*, *21*, 610–619.

Hansen, B., Larsen, K. M. H., Olsen, S. M., Quadfasel, D., Jochumsen, K., &

Østerhus, S. (2018, aug). Overflow of cold water across the IcelandFaroe Ridge through the Western Valley. *Ocean Science*, *14*(4), 871–885. Retrieved from https://os.copernicus.org/articles/14/871/2018/ doi: 10.5194/os-14-871-2018

Hansen, B., & Østerhus, S. (2000, feb). North AtlanticNordic Seas exchanges. *Progress in Oceanography*, *45*(2), 109–208. Retrieved from https://linkinghub.elsevier.com/retrieve/pii/S007966119900052X doi: 10.1016/S0079-6611(99)00052-X

Harada, Y., Kamahori, H., Kobayashi, C., Endo, H., Kobayashi, S., Ota, Y., ... Takahashi, K. (2016). The JRA-55 Reanalysis: Representation of Atmospheric Circulation and Climate Variability. *Journal of the Meteorological Society of Japan. Ser. II*, *94*(3), 269–302. Retrieved from https://www.jstage.jst.go.jp/article/jmsj/94/3/94_2016-015/_article doi: 10.2151/jmsj.2016-015

Hirt, C., Amsden, A., & Cook, J. (1974). An arbitrary LagrangianEulerian computing method for all flow speeds. *Journal of Computational Physics*, *14*(3), 227–253.

Hofmeister, R., Burchard, H., & Beckers, J. M. (2010). Non-uniform adaptive vertical grids for 3D numerical ocean models. *Ocean Modelling*, *33*(1-2), 70–86. Retrieved from http://dx.doi.org/10.1016/j.ocemod.2009.12.003 doi: 10.1016/j.ocemod.2009.12.003

Holliday, N. P., Cunningham, S. A., Johnson, C., Gary, S. F., Griffiths, C., Read, J. F., & Sherwin, T. (2015, sep). Multidecadal variability of potential temperature, salinity, and transport in the eastern subpolar North Atlantic. *Journal of Geophysical Research: Oceans*, *120*(9), 5945–5967. Retrieved from https://onlinelibrary.wiley.com/doi/abs/10.1002/2015JC010762 doi: 10.1002/2015JC010762

Hopkins, J. E., Holliday, N. P., Rayner, D., Houpert, L., Le Bras, I., Straneo, F., ... Bacon, S. (2019, may). Transport Variability of the Irminger Sea Deep Western Boundary Current From a Mooring Array. *Journal of Geophysical Research: Oceans*, *124*(5), 3246–3278. Retrieved from https://onlinelibrary.wiley.com/doi/abs/10.1029/2018JC014730 doi: 10.1029/2018JC014730

Horn, R. A., & Johnson, C. R. (1985). *Matrix Analysis*. Cambridge University Press. Retrieved from https://www.cambridge.org/core/product/identifier/9780511810817/type/book doi: 10.1017/CBO9780511810817

Hughes, S., Turrell, W., Hansen, B., & Østerhus, S. (2006). Fluxes of Atlantic Water (volume, heat and salt) through the Faroe Shetland Channel calculated using a decade of acoustic Doppler current profiler data (1994–2005). Collaborative Rep. 01/06. *Fisheries Research Services, Marine Laboratory*, *77*.

Ilcak, M., Adcroft, A. J., Griffies, S. M., & Hallberg, R. W. (2012, jan). Spurious dianeutral mixing and the role of momentum closure. *Ocean Modelling*, *45-46*, 37–58. Retrieved from https://linkinghub.elsevier.com/retrieve/pii/S1463500311001685 doi: 10.1016/j.ocemod.2011.10.003

Johns, W. E., Devana, M., Houk, A., & Zou, S. (2021, aug). Moored Observations of the IcelandScotland Overflow Plume Along the Eastern Flank of the Reykjanes Ridge. *Journal of Geophysical Research: Oceans*, *126*(8). Retrieved from https://onlinelibrary.wiley.com/doi/10.1029/2021JC017524 doi: 10.1029/2021JC017524

Johnson, H. L., Cessi, P., Marshall, D. P., Schloesser, F., & Spall, M. A. (2019, aug). Recent Contributions of Theory to Our Understanding of the Atlantic Meridional Overturning Circulation. *Journal of Geophysical Research: Oceans*, *124*(8), 5376–5399. Retrieved from https://onlinelibrary.wiley.com/doi/10.1029/2019JC015330 doi: 10.1029/2019JC015330

Kasahara, A. (1974, jul). Various Vertical Coordinate Systems Used for Numerical Weather Prediction. *Monthly Weather Review*, *102*(7), 509–522. doi: 10.1175/

1520-0493(1974)102⟨0509:VVCSUF⟩2.0.CO;2

Käse, R. H. (2003). Structure and variability of the Denmark Strait Overflow: Model and observations. *Journal of Geophysical Research*, *108*(C6), 3181. Retrieved from `http://doi.wiley.com/10.1029/2002JC001548` doi: 10.1029/2002JC001548

Kieke, D., & Rhein, M. (2006, mar). Variability of the Overflow Water Transport in the Western Subpolar North Atlantic, 195097. *Journal of Physical Oceanography*, *36*(3), 435–456. Retrieved from `http://journals.ametsoc.org/doi/10.1175/JPO2847.1` doi: 10.1175/JPO2847.1

Kobayashi, S., Ota, Y., Harada, Y., Ebita, A., Moriya, M., Onoda, H., ... Takahashi, K. (2015). The JRA-55 Reanalysis: General Specifications and Basic Characteristics. *Journal of the Meteorological Society of Japan. Ser. II*, *93*(1), 5–48. Retrieved from `https://www.jstage.jst.go.jp/article/jmsj/93/1/93_2015-001/_article` doi: 10.2151/jmsj.2015-001

Laanaia, N., Wirth, A., Molines, J. M., Barnier, B., & Verron, J. (2010, jun). On the numerical resolution of the bottom layer in simulations of oceanic gravity currents. *Ocean Science*, *6*(2), 563–572. Retrieved from `http://www.ocean-sci.net/6/563/2010/` doi: 10.5194/os-6-563-2010

Large, W. G., & Yeager, S. G. (2009, aug). The global climatology of an interannually varying airsea flux data set. *Climate Dynamics*, *33*(2-3), 341–364. Retrieved from `http://link.springer.com/10.1007/s00382-008-0441-3` doi: 10.1007/s00382-008-0441-3

Leclair, M., & Madec, G. (2011). z-Coordinate, an Arbitrary Lagrangian-Eulerian coordinate separating high and low frequency motions. *Ocean Modelling*, *37*(3-4), 139–152. Retrieved from `http://linkinghub.elsevier.com/retrieve/pii/S1463500311000126` doi: 10.1016/j.ocemod.2011.02.001

Legg, S., Briegleb, B., Chang, Y., Chassignet, E. P., Danabasoglu, G., Ezer, T., ... Yang, J. (2009, may). Improving Oceanic Overflow Representation in Climate Models: The Gravity Current Entrainment Climate Process Team. *Bulletin of the American Meteorological Society*, *90*(5), 657–670. Retrieved from `http://journals.ametsoc.org/doi/10.1175/2008BAMS2667.1` doi: 10.1175/2008BAMS2667.1

Legg, S., Hallberg, R. W., & Girton, J. B. (2006, jan). Comparison of entrainment in overflows simulated by z-coordinate, isopycnal and non-hydrostatic models. *Ocean Modelling*, *11*(1-2), 69–97. Retrieved from `http://linkinghub.elsevier.com/retrieve/pii/S1463500304001064` doi: 10.1016/j.ocemod.2004.11.006

Lemarié, F., Kurian, J., Shchepetkin, A. F., Jeroen Molemaker, M., Colas, F., & McWilliams, J. C. (2012, jan). Are there inescapable issues prohibiting the use of terrain-following coordinates in climate models? *Ocean Modelling*, *42*, 57–79. doi: 10.1016/j.ocemod.2011.11.007

Levier, B., Treguier, A. M., Madec, G., & Garnier, V. (2007). *Free surface and variable volume in the NEMO code* (Tech. Rep.). Brest, France, MESRSEA IP report WP09-CNRS-STR03-1: IFREMER.

Li, F., Lozier, M. S., Bacon, S., Bower, A., Cunningham, S., de Jong, M., ... Zhou, C. (2023). *Temperature, Salinity and Velocity Data Derived from the OSNAP Array between August 2014 and May 2018* (Tech. Rep.). Georgia Institute of Technology. School of Earth and Atmospheric Sciences. doi: https://doi.org/10.35090/gatech/70328

Lozier, M. S., Bacon, S., Bower, A. S., Cunningham, S. A., Femke de Jong, M., de Steur, L., ... Zika, J. D. (2017, apr). Overturning in the Subpolar North Atlantic Program: A New International Ocean Observing System. *Bulletin of the American Meteorological Society*, *98*(4), 737–752. Retrieved from `https://journals.ametsoc.org/doi/10.1175/BAMS-D-16-0057.1` doi: 10.1175/BAMS-D-16-0057.1

Lozier, M. S., Li, F., Bacon, S., Bahr, F., Bower, A. S., Cunningham, S. A., ... Zhao, J. (2019, feb). A sea change in our view of overturning in the subpolar North Atlantic. *Science*, *363*(6426), 516–521. Retrieved from `https://www.science.org/doi/10.1126/science.aau6592` doi: 10.1126/science.aau6592

Lozier, S. M., Bower, A. S., Furey, H. H., Drouin, K. L., Xu, X., & Zou, S. (2022, nov). Overflow water pathways in the North Atlantic. *Progress in Oceanography*, *208*, 102874. Retrieved from `https://linkinghub.elsevier.com/retrieve/pii/S0079661122001331` doi: 10.1016/j.pocean.2022.102874

Madec, G., Delecluse, P., Crépon, M., & Lott, F. (1996, aug). Large-Scale Preconditioning of Deep-Water Formation in the Northwestern Mediterranean Sea. *Journal of Physical Oceanography*, *26*(8), 1393–1408. doi: 10.1175/1520-0485(1996)026⟨1393:LSPODW⟩2.0.CO;2

Madec, G., & NEMO-team. (2019). NEMO ocean engine. *Scientific Notes of Climate Modelling Center, Institut Pierre-Simon Laplace (IPSL)*(27). doi: 10.5281/zenodo.1464816

Martinho, A. S., & Batteen, M. L. (2006). On reducing the slope parameter in terrain-following numerical ocean models. *Ocean Modelling*, *13*(2), 166–175. doi: 10.1016/j.ocemod.2006.01.003

Marzocchi, A., Hirschi, J. J.-M., Holliday, N. P., Cunningham, S. A., Blaker, A. T., & Coward, A. C. (2015, feb). The North Atlantic subpolar circulation in an eddy-resolving global ocean model. *Journal of Marine Systems*, *142*, 126–143. Retrieved from `https://linkinghub.elsevier.com/retrieve/pii/S0924796314002437` doi: 10.1016/j.jmarsys.2014.10.007

Mastropole, D., Pickart, R. S., Valdimarsson, H., Våge, K., Jochumsen, K., & Girton, J. (2017, jan). On the hydrography of Denmark Strait. *Journal of Geophysical Research: Oceans*, *122*(1), 306–321. Retrieved from `http://doi.wiley.com/10.1002/2016JC012007` doi: 10.1002/2016JC012007

Megann, A., Chanut, J., & Storkey, D. (2022, nov). Assessment of the z Time-Filtered Arbitrary LagrangianEulerian Coordinate in a Global EddyPermitting Ocean Model. *Journal of Advances in Modeling Earth Systems*, *14*(11). Retrieved from `https://agupubs.onlinelibrary.wiley.com/doi/10.1029/2022MS003056` doi: 10.1029/2022MS003056

Megann, A., New, A. L., Blaker, A. T., & Sinha, B. (2010, oct). The Sensitivity of a Coupled Climate Model to Its Ocean Component. *Journal of Climate*, *23*(19), 5126–5150. Retrieved from `http://journals.ametsoc.org/doi/10.1175/2010JCLI3394.1` doi: 10.1175/2010JCLI3394.1

Mellor, G. L., Ezer, T., & Oey, L.-Y. (1994). The Pressure Gradient Conundrum of Sigma Coordinate Ocean Models. *Journal of Atmospheric and Oceanic Technology*, *11*(4), 1126–1134. Retrieved from `http://journals.ametsoc.org/doi/pdf/10.1175/2517.1%5Cnhttp://journals.ametsoc.org/doi/abs/10.1175/1520-0426%281994%29011%3C1126%3ATPGCOS%3E2.0.CO%3B2%5Cnhttp://dx.doi.org/10.1175/1520-0426(1994)011%3C1126:TPGCOS%3E2.0.CO` doi: 10.1175/1520-0426(1994)011⟨1126:TPGCOS⟩2.0.CO;2

Mellor, G. L., Oey, L. Y., & Ezer, T. (1998). Sigma coordinate pressure gradient errors and the seamount Problem. *Journal of Atmospheric and Oceanic Technology*, *15*(5), 1122–1131. doi: 10.1175/1520-0426(1998)015⟨1122:SCPGEA⟩2.0.CO;2

O'Dea, E. J., Arnold, A. K., Edwards, K. P., Furner, R., Hyder, P., Martin, M. J., ... Liu, H. (2012). An operational ocean forecast system incorporating NEMO and SST data assimilation for the tidally driven European North-West shelf. *Journal of Operational Oceanography*, *5*(1), 3–17. doi: 10.1080/1755876X.2012.1102012

Østerhus, S., Woodgate, R., Valdimarsson, H., Turrell, B., de Steur, L., Quadfasel, D., ... Berx, B. (2019, apr). Arctic Mediterranean exchanges: a consistent volume budget and trends in transports from two decades of observations. *Ocean Science*, *15*(2), 379–399. Retrieved from https://os.copernicus.org/articles/15/379/2019/ doi: 10.5194/os-15-379-2019

Pacanowski, R. C., Gnanadesikan, A., & Olume, V. (1998). Transient Response in a Z -Level Ocean Model That Resolves Topography with Partial Cells. *Monthly Weather Review*, *126*(12), 3248–3270. doi: 10.1175/1520-0493(1998)126⟨3248:TRIAZL⟩2.0.CO;2

Penduff, T., Le Sommer, J., Barnier, B., Treguier, A.-M., Molines, J.-M., & Madec, G. (2007, dec). Influence of numerical schemes on current-topography interactions in 1/4 global ocean simulations. *Ocean Science*, *3*(4), 509–524. Retrieved from https://os.copernicus.org/articles/3/509/2007/ doi: 10.5194/os-3-509-2007

Petersen, M. R., Jacobsen, D. W., Ringler, T. D., Hecht, M. W., & Maltrud, M. E. (2015, feb). Evaluation of the arbitrary LagrangianEulerian vertical coordinate method in the MPAS-Ocean model. *Ocean Modelling*, *86*, 93–113. Retrieved from https://linkinghub.elsevier.com/retrieve/pii/S1463500314001796 doi: 10.1016/j.ocemod.2014.12.004

Phillips, N. A. (1957, apr). A coordinate system having some special advantages for numerical forecasting. *Journal of Meteorology*, *14*(2), 184–185. Retrieved from http://journals.ametsoc.org/doi/10.1175/1520-0469(1957)014%3C0184:ACSHSS%3E2.0.CO;2 doi: 10.1175/1520-0469(1957)014⟨0184:ACSHSS⟩2.0.CO;2

Quadfasel, D. (2018). *Physical oceanography during POSEIDON cruise POS503.* PANGAEA. Retrieved from https://doi.org/10.1594/PANGAEA.890699 doi: 10.1594/PANGAEA.890699

Rattan, S., Myers, P. G., Treguier, A.-M., Theetten, S., Biastoch, A., & Böning, C. (2010, jan). Towards an understanding of Labrador Sea salinity drift in eddy-permitting simulations. *Ocean Modelling*, *35*(1-2), 77–88. Retrieved from https://linkinghub.elsevier.com/retrieve/pii/S1463500310001009 doi: 10.1016/j.ocemod.2010.06.007

Riemenschneider, U., & Legg, S. (2007, jan). Regional simulations of the Faroe Bank Channel overflow in a level model. *Ocean Modelling*, *17*(2), 93–122. Retrieved from https://linkinghub.elsevier.com/retrieve/pii/S146350030700011X doi: 10.1016/j.ocemod.2007.01.003

Saunders, P. M. (1996, jan). The Flux of Dense Cold Overflow Water Southeast of Iceland. *Journal of Physical Oceanography*, *26*(1), 85–95. Retrieved from http://journals.ametsoc.org/doi/10.1175/1520-0485(1996)026%3C0085:TFODCO%3E2.0.CO;2 doi: 10.1175/1520-0485(1996)026⟨0085:TFODCO⟩2.0.CO;2

Schoonover, J., Dewar, W., Wienders, N., Gula, J., McWilliams, J. C., Molemaker, M. J., … Yeager, S. (2016, jan). North Atlantic Barotropic Vorticity Balances in Numerical Models. *Journal of Physical Oceanography*, *46*(1), 289–303. Retrieved from https://journals.ametsoc.org/view/journals/phoc/46/1/jpo-d-15-0133.1.xml doi: 10.1175/JPO-D-15-0133.1

Seim, K. S., Fer, I., & Berntsen, J. (2010, jan). Regional simulations of the Faroe Bank Channel overflow using a σ-coordinate ocean model. *Ocean Modelling*, *35*(1-2), 31–44. Retrieved from https://linkinghub.elsevier.com/retrieve/pii/S1463500310000843 doi: 10.1016/j.ocemod.2010.06.002

Shchepetkin, A. F., & McWilliams, J. C. (2005, jan). The regional oceanic modeling system (ROMS): a split-explicit, free-surface, topography-following-coordinate oceanic model. *Ocean Modelling*, *9*(4), 347–404. doi: 10.1016/j.ocemod.2004.08.002

Song, Y., & Haidvogel, D. (1994, nov). A Semi-implicit Ocean Circulation Model Using a Generalized Topography-Following Coordinate System. *Journal of Computational Physics*, *115*(1), 228–244. doi: 10.1006/jcph.1994.1189

Stacey, M. W., Pond, S., & Nowak, Z. P. (1995, jun). A Numerical Model of the Circulation in Knight Inlet, British Columbia, Canada. *Journal of Physical Oceanography*, *25*(6), 1037–1062. Retrieved from http://journals.ametsoc.org/doi/10.1175/1520-0485(1995)025%3C1037:ANMOTC%3E2.0.CO;2 doi: 10.1175/1520-0485(1995)025⟨1037:ANMOTC⟩2.0.CO;2

Treguier, A. M., Theetten, S., Chassignet, E. P., Penduff, T., Smith, R., Talley, L., ... Böning, C. (2005, may). The North Atlantic Subpolar Gyre in Four High-Resolution Models. *Journal of Physical Oceanography*, *35*(5), 757–774. Retrieved from http://journals.ametsoc.org/doi/10.1175/JPO2720.1 doi: 10.1175/JPO2720.1

Wang, H., Legg, S. A., & Hallberg, R. W. (2015, feb). Representations of the Nordic Seas overflows and their large scale climate impact in coupled models. *Ocean Modelling*, *86*, 76–92. Retrieved from https://linkinghub.elsevier.com/retrieve/pii/S1463500314001802 doi: 10.1016/j.ocemod.2014.12.005

Willebrand, J., Barnier, B., Böning, C., Dieterich, C., Killworth, P. D., Le Provost, C., ... New, A. L. (2001, jan). Circulation characteristics in three eddy-permitting models of the North Atlantic. *Progress in Oceanography*, *48*(2-3), 123–161. Retrieved from https://linkinghub.elsevier.com/retrieve/pii/S0079661101000039 doi: 10.1016/S0079-6611(01)00003-9

Winton, M., Hallberg, R., & Gnanadesikan, A. (1998, nov). Simulation of Density-Driven Frictional Downslope Flow in Z -Coordinate Ocean Models. *Journal of Physical Oceanography*, *28*(11), 2163–2174. Retrieved from http://journals.ametsoc.org/doi/10.1175/1520-0485(1998)028%3C2163:SODDFD%3E2.0.CO;2 doi: 10.1175/1520-0485(1998)028⟨2163:SODDFD⟩2.0.CO;2

Wise, A., Harle, J., Bruciaferri, D., O'Dea, E., & Polton, J. (2021, dec). The effect of vertical coordinates on the accuracy of a shelf sea model. *Ocean Modelling*, 101935. Retrieved from https://linkinghub.elsevier.com/retrieve/pii/S1463500321001827 doi: 10.1016/j.ocemod.2021.101935

Xu, X., Bower, A., Furey, H., & Chassignet, E. P. (2018, aug). Variability of the IcelandScotland Overflow Water Transport Through the CharlieGibbs Fracture Zone: Results From an Eddying Simulation and Observations. *Journal of Geophysical Research: Oceans*, *123*(8), 5808–5823. Retrieved from https://onlinelibrary.wiley.com/doi/10.1029/2018JC013895 doi: 10.1029/2018JC013895

Xu, X., Schmitz, W. J., Hurlburt, H. E., Hogan, P. J., & Chassignet, E. P. (2010, dec). Transport of Nordic Seas overflow water into and within the Irminger Sea: An eddyresolving simulation and observations. *Journal of Geophysical Research: Oceans*, *115*(C12). Retrieved from https://onlinelibrary.wiley.com/doi/10.1029/2010JC006351 doi: 10.1029/2010JC006351

Localised general vertical coordinates for quasi-Eulerian ocean models: the Nordic overflows test-case

Diego Bruciaferri[1], Catherine Guiavarc'h[1], Helene T. Hewitt[1], James Harle[2], Mattia Almansi[2*], Pierre Mathiot[3]

[1]Met Office Hadley Center, Exeter, UK
[2]National Oceanography Centre, Southampton, UK
[3]Université Grenoble Alpes, CNRS, IRD, Grenoble INP, Grenoble, France

Key Points:

- A generalised methodology to embed distinct types of vertical coordinates in local time-invariant targeted areas of quasi-Eulerian ocean models
- Three different types of terrain-following coordinates are localised in the Nordic overflows region of a geopotential-levels based global model
- Local multi-envelope terrain-following levels reduce spurious diapycnal mixing and improve the accuracy of the simulated Nordic overflows

*now at B-Open Solutions srl, Rome, Italy

Corresponding author: Diego Bruciaferri, `diego.bruciaferri@metoffice.gov.uk`

Abstract

A generalised methodology to deploy different types of vertical coordinate system in arbitrarily defined time-invariant local areas of quasi-Eulerian numerical ocean models is presented. After detailing its characteristics, we show how the novel *localisation* method can be used to improve the representation of the Nordic Seas overflows in the UK Met Office NEMO-based eddy-permitting global ocean configuration. Three z*-levels with partial steps models localising different types of terrain-following vertical coordinates in the proximity of the Greenland-Scotland ridge are developed and compared against a control. Experiments include a series of idealised and realistic numerical simulations where the skill of the models in computing pressure forces, reducing spurious diapycnal mixing and reproducing observed properties of the Nordic Seas overflows are assessed. Numerical results prove that the localisation approach proposed here can be successfully used to embed terrain-following levels in a global geopotential levels-based configuration, provided that the localised vertical coordinate chosen is flexible enough to allow a smooth transition between the two. In addition, our experiments show that deploying localised terrain-following coordinates via the multi-envelope method allows the crucial reduction of spurious cross-isopycnal mixing when modelling bottom intensified buoyancy driven currents, significantly improving the realism of the Nordic Seas overflows simulations in comparison to the other models. Important hydrographic biases are found to similarly affect all the realistic experiments and a discussion on how their interaction with the type of localised vertical coordinate affects the accuracy of the simulated overflows is provided.

Plain Language Summary

Numerical ocean models are arguably one of the most advanced tools the scientific community can use to study the role of the worlds oceans. However, the ability of an ocean model to realistically simulate ocean currents depends on some of the numerical techniques it employs. One such example concerns the type of vertical coordinate system employed. Ocean models usually implement a single type of vertical coordinate throughout the entire model domain, which is typically unable to accurately represent the vast variety of physical processes driving the oceans. In this study, we propose a new method that allows different types of vertical coordinates in selected regions of the same model domain. Our method targets a particular class of ocean models (known as quasi-Eulerian), improving the way they represent the important influence the sea floor exerts on ocean currents. After introducing our novel approach, we present the results of a series of numerical experiments where we test its skill for improving the representation of the Nordic Seas overflows, an important type of ocean current located at depth in the proximity of the Greenland-Scotland ridge.

1 Introduction

The governing equations of modern numerical ocean models are typically formulated in terms of a generalised vertical coordinate (GVC) $s = s(x, y, z, t)$ (e.g., Bleck (2002); Adcroft & Campin (2004); Shchepetkin & McWilliams (2005); Leclair & Madec (2011); Griffies (2012); Petersen et al. (2015); Adcroft et al. (2019)), where the only constraint for s is to be a strictly monotone function of the depth z (e.g., Kasahara (1974); Griffies (2004)). In general, GVCs usually employed in numerical ocean models can be divided in three main groups, depending on the type of the time-stepping algorithm used to solve the oceanic equations (e.g., Adcroft & Hallberg (2006); Leclair & Madec (2011); Griffies et al. (2020)): quasi-Eulerian (QE; e.g., Kasahara (1974)), quasi-Lagrangian (QL; e.g., Bleck (2002)) and Arbitrary Lagrangian Eulerian (ALE; e.g., Hirt et al. (1974)) coordinates.

QE coordinates 'breath' with the barotropic motion of the ocean and diagnose the vertical advective velocities from mass continuity. Examples of this type of GVCs are the rescaled geopotential z^*-coordinate (Stacey et al. (1995); Adcroft & Campin (2004)), the various flavours of terrain-following σ-coordinates (e.g., Phillips (1957); Song & Haidvogel (1994); Shchepetkin & McWilliams (2005)) and subsequent hybridisation of these two ($z^*-\sigma$ coordinates; e.g., Dukhovskoy et al. (2009); Bruciaferri et al. (2018); Wise et al. (2021)).

The second type of GVCs are the QL coordinates; they take advantage of vertical Lagrangian-remap methods to evolve with the flow whilst retaining a grid able to provide an accurate representation of the ocean state, as in modern isopycnal models (e.g., Bleck (2002); Adcroft et al. (2019)).

Lastly, and providing the most general framework, are the ALE coordinates, such as the $\tilde{z}$-coordinate proposed by Leclair & Madec (2011) and Petersen et al. (2015) or the adaptive terrain-following γ-coordinates of Hofmeister et al. (2010). This class of GVCs employs vertical ALE methods to modify the computational grid in time with a motion that typically does not strictly mimic the oceanic flow (i.e., in a Lagrangian sense), but can follow any prescribed algorithm.

In the continuous limit, oceanic equations formulated in different GVCs are of course completely equivalent. However, numerical discretisation can introduce errors specific to the type of GVC employed that can seriously undermine the ability of a numerical model to accurately represent some aspects of the oceanic dynamics, especially on climatic scales (e.g., Haidvogel & Beckmann (1999); Griffies, Böning, et al. (2000)). One such example is the inevitable truncation errors that arise the tracer advection schemes, causing substantial spurious diapycnal mixing in the ocean interior of QE models. This leads to a modification of water masses and potentially significant climatic model drifts (Griffies, Böning, et al., 2000; Griffies, Pacanowski, & Hallberg, 2000). It has been demonstrated that the same type of numerical mixing can be greatly reduced when using QL or ALE vertical coordinates (e.g., Adcroft et al. (2019); Megann et al. (2022)).

The choice of GVC also dictates the way an ocean model resolves the bottom topography, hence affecting its ability to simulate the critical interactions between flow and topography. In the case of QE geopotential coordinates, the step-like nature of the sea floor in the ocean model can compromise the accuracy of the simulated large scale ocean dynamics (e.g., Penduff et al. (2007); Ezer (2016)). In addition, it also has the potential to introduce significant spurious mixing when simulating gravity current flows (e.g., Winton et al. (1998); Legg et al. (2006, 2009); Colombo et al. (2020)). With an improved representation of the sea floor, as in the case of QE terrain-following coordinates, flow-topography interactions are more naturally simulated and such deficiencies can be substantially reduced (e.g., Willebrand et al. (2001); Käse (2003); Ezer (2005, 2016); Schoonover et al. (2016)). However, employing QE terrain-following coordinates in regions of steep topography can introduce significant errors in the computation of horizontal pressure forces, making their use in global configurations challenging (e.g., Lemarié et al. (2012)). The use of isopycnal coordinates has been proven to be effective in reducing spurious mixing in idealised (Legg et al., 2006) and realistic simulations of the Nordic Seas overflows (Megann et al., 2010; Wang et al., 2015; Guo et al., 2016). However, such models suffer from the outcropping of coordinate interfaces in weakly stratified regions and detrainment from a mixed layer into the ocean interior (e.g., Megann et al. (2022)).

Ocean models typically implement one single type of vertical coordinate throughout the model domain. However, it is evident that a perfect vertical coordinate suitable for *any* oceanic regime does not exist and a hybrid approach, combining the best features of each vertical coordinate system within a single framework, is currently an active area of research. In one such example, Bleck (2002, HYCOM) and subsequently Adcroft et al. (2019, MOM6) tried to alleviate some of the drawbacks of isopycnal models using a QL hybrid isopycnal-z^* vertical coordinate. Adcroft et al. (2019) reports that issues still remain with the dense high latitude overflows and concludes that more research is needed to determine a robust vertical grid algorithm suitable for the World Ocean. On paper, generalised ALE coordinates appear to be the most attractive framework for evolving in time the vertical grid according to a *dynamical* algorithm that seeks the optimal coordinate configuration for the various oceanic regimes of the model domain. However, the practical realisation of such an *optimal* ALE is non-trivial, and active research is currently on-going (e.g., Hofmeister et al. (2010); Gibson (2019)).

To better represent some features of the ocean dynamics such as flow-topography interactions, an algorithm that defines time-invariant target areas of the model domain where the vertical grid smoothly transitions into another more appropriate GVC may be sufficient. This was the concept behind the local-sigma vertical coordinate of Colombo (2018): to improve the representation of Nordic Seas overflows in a global model, terrain-following coordinates were employed only in the proximity of the Greenland-Scotland ridge, whilst standard z^*-coordinates with partial steps were used everywhere else. However, the development of such a mesh is non-trivial, especially when defining the transition zone between the two vertical coordinates. Consequently, their approach resulted in an ad hoc methodology not easily generalizable and applicable to different scenarios.

Building on the study of Colombo (2018), the aim of this paper is to (i) introduce a general methodology that enables QE numerical ocean models to localise (i.e., embed) various GVCs configurations within a model domain and (ii) assess the ability of the new method to improve the representation of the Nordic Seas overflows in eddy-permitting global ocean simulations. Two different types of numerical experiments are conducted in this study. At first, a series of idealised numerical experiments is carried out to test the accuracy of localised GVCs in computing horizontal pressure forces and reproducing gravity currents. After, realistic global simulations are run to test the skill of the localised vertical coordinates in reproducing observed properties of the Nordic Seas overflows when compared with the traditional approach of employing z^*-coordinates with partial steps.

The Nordic Seas overflows consist of dense cold waters formed in the Nordic Seas and the Arctic Ocean and flowing south via the Greenland-Scotland ridge in the form of strong gravity currents that form the lower limb of the Atlantic Meridional Overturning Circulation (AMOC; e.g. Dickson & Brown (1994); Johnson et al. (2019); Østerhus et al. (2019)). Several physical processes combine to generate such dense water masses, including i) open ocean convection in the Greenland sea, ii) cascading from the Arctic shelves and iii) transformation of North Atlantic Water (NAW) recirculating within a cyclonic boundary current along the Icelandic basin and the Irminger Sea topography (e.g. Hansen & Østerhus (2000)).

The Nordic Seas overflows include the Denmark Strait Overflow Water (DSOW) and the Iceland-Scotland Overflow Water (ISOW). The DSOW flows south via the Denmark Strait (see Fig. 1), cascading along the continental slope of the western Irminger Sea (Dickson & Brown, 1994). While descending, the DSOW entrains and mixes with the ambient water encountered along its path, resulting in an approximately doubled transport within a few hundred kilometres downstream of the Denmark Strait sill (Dickson et al., 2008). In the proximity of Cape Farewell, the DSOW turns westward and enters the Labrador Sea as the densest part of the Deep Western Boundary Current (DWBC) (e.g. Hopkins et al. (2019)).

The path of the ISOW is more complex (see also Fig. 1 for the locations). It crosses the Greenland-Scotland ridge primarily via the Faroe-Shetland channel and the Faroe-Bank channel, although secondary contributions via the Wyville Thomson ridge and the Iceland-Faroe ridge are also important (Østerhus et al., 2019). Once the main branch has passed the Faroe-Bank channel, the ISOW descends along the Iceland-Faroe slope, mixing with waters spilling from the Iceland-Faroe ridge. After, the ISOW proceeds southwestward into the Icelandic basin, flowing along the eastern flank of the Reykjanes ridge and mixing with the surrounding ambient fluid. While early observational studies indicated a reduced importance of mixing and dilution in comparison to the DSOW (Saun-

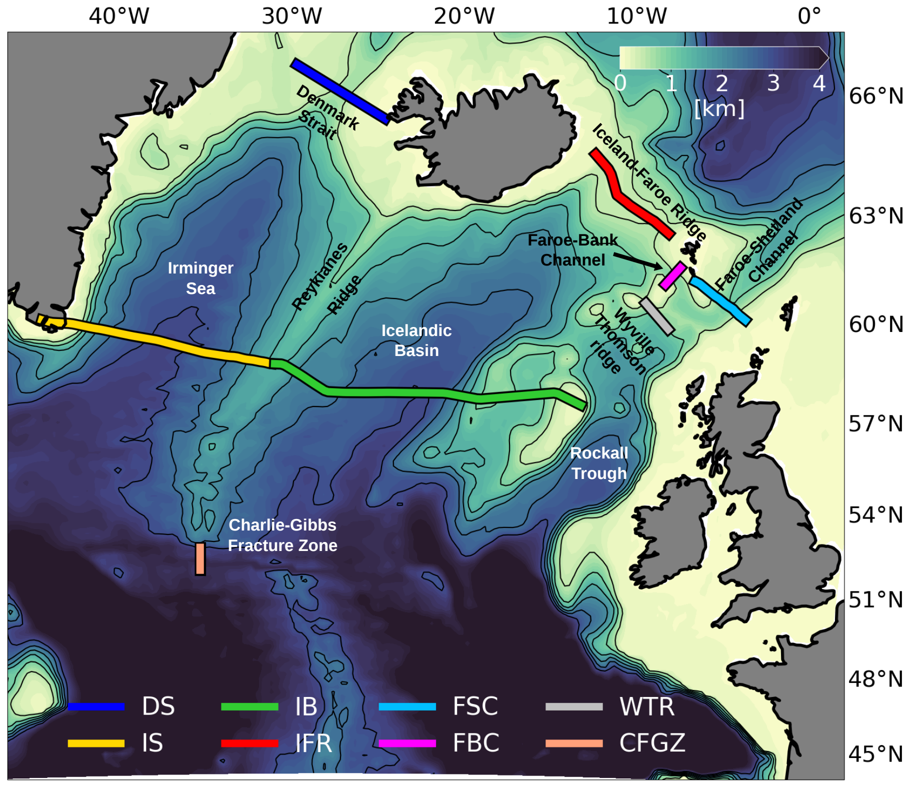

Figure 1. Bathymetry of the Nordic overflows region at 1/4° of resolution showing the location of the main geographical features of the area and the position of the observational cross-sections analysed in the realistic experiments - see Sec. 5 and Tab. 1 for the details. The thin black lines are selected isobaths ranging from 500 m to 3000 m with a discretisation step of 500 m.

ders, 1996), recent estimates appear to suggest that entrainment contributes in doubling the ISOW transport (Johns et al., 2021). The modified ISOW leaves the Icelandic basin through multiple pathways (e.g., Hopkins et al. (2019); S. M. Lozier et al. (2022)): on the one side, the dense water descending the Icelandic basin directly flows into the Irminger Sea via various gaps in the Reykjanes ridge; on the other side, after flowing through the Charlie-Gibbs Fracture Zone, the modified ISOW either continues westward spreading towards the Labrador Sea or enters the Irminger sea as a deep boundary current that flows cyclonically around the continental slope of the Irminger basin and rides above the DSOW to form the lightest part of the DWBC.

The manuscript is organised as follows. Section 2 describes the details of the localisation method proposed in this study. Section 3 introduces the Nordic overflows test-case, describing the global ocean model used in our integrations and the three localised QE vertical coordinates developed and tested in our experiments. Sections 4 and 5 describe and discuss the set-up and the results of the idealised and realistic numerical experiments conducted in this work, respectively. Finally, Sec. 6 summarise our conclusion and discuss future perspectives. For the reader convenience, a list of the acronyms used in this paper is given in Appendix D.

2 Localised quasi-Eulerian vertical coordinates

The intent of developing localised GVCs is to provide ocean models with the capability of arbitrarily varying the vertical coordinate system in targeted areas of the model domain. Although the broad idea of changing/adapting the vertical grid within an ocean model is not new (e.g., Beckers et al. (2002); Colombo (2018); Adcroft et al. (2019)), the approach proposed here combines three specific attractive features:

1) it uses a generalised, simple and fully reproducible algorithm to define time-invariant limited areas of the model domain where local-GVCs will be employed;
2) it allows one to have full control on the definition of the areas where local-GVCs will be employed as well as on the final set-up of the vertical grid;
3) it is simple and efficient, allowing for minimal modifications to the original code of an oceanic model;

Some of these properties follow from the fact that the method introduced here targets QE GVCs, exploiting some key features of this specific class of vertical coordinates. In the next two sections, first the QE approach is summarised (Sec. 2.1) and after the details of the localisation algorithm are described (Sec. 2.2).

2.1 The quasi-Eulerian approach to vertical coordinates

The QE approach applies to any GVCs where the vertical coordinate transformation can be expressed as a direct function of the ocean free-surface $\eta(x, y, t)$. The evolution in time of QE coordinate interfaces is importantly controlled by the prognostic thickness equation. In the case of an incompressible Boussinesq ocean, the continuous thickness equation can be written in terms of a GVC $s = s(x, y, z, t)$ and in conservation form as (e.g., Bleck (1978); Burchard et al. (1997); Griffies et al. (2020))

$$\frac{\partial h}{\partial t} + \nabla_s \cdot (h\,\mathbf{u}) + \frac{\partial w}{\partial s} = 0, \tag{1}$$

where $h(x, y, s, t) = \partial_s z$ is the Jacobian of the coordinate transformation, $\nabla_s = (\partial_x|_s, \partial_y|_s, 0)$ is the lateral gradient operator acting along surfaces of constant s, $\mathbf{u}(x, y, s, t)$ is the horizontal flow vector and $w(x, y, s, t) = h\, D_t s$ is the dia-surface velocity (with D_t the material time derivative operator; see Griffies (2004) for the details).

When moving to a discrete level, the transformed vertical domain can be divided into N layers $k = 1, ..., N$, so that the k^{th} generic model layer is bounded by generalised coordinate interfaces $s_{k+\frac{1}{2}}$ at the top and $s_{k-\frac{1}{2}}$ at the bottom, respectively. In such a framework, the thickness $h_k(x, y, t)$ of the discrete layer k is given by

$$h_k = \int_{s_{k-\frac{1}{2}}}^{s_{k+\frac{1}{2}}} h(x, y, s, t)\, ds = z_{k+\frac{1}{2}} - z_{k-\frac{1}{2}}, \tag{2}$$

where $z_{k\pm\frac{1}{2}}(x, y, t) = z\Big(x, y, s_{k\pm\frac{1}{2}}, t\Big)$ and $z_{k+\frac{1}{2}} > z_{k-\frac{1}{2}}$. This definition ensures that $\int_{s(z=-H)}^{s(z=\eta)} h\, ds = \sum_{k=1}^{N} h_k = H + \eta$, with $H(x, y)$ the ocean bottom topography and $z_{\frac{1}{2}} = -H(x, y)$ at the bottom boundary and $z_{N+\frac{1}{2}} = \eta(x, y)$ at the free surface. Consequently, the layer integrated thickness equation reads

$$\frac{\partial h_k}{\partial t} + \nabla_s \cdot (h_k\, \mathbf{u}_k) + w_{k+\frac{1}{2}} - w_{k-\frac{1}{2}} = 0, \tag{3}$$

where $\mathbf{u}_k(x,y,t) = h_k^{-1}\int_{s_{k-\frac{1}{2}}}^{s_{k+\frac{1}{2}}} h\mathbf{u}\,ds$ is the layer averaged horizontal flow vector and $w_{k\pm\frac{1}{2}}(x,y,t) = w\Big(x,y,s_{k\pm\frac{1}{2}},t\Big)$.

The QE algorithm includes two steps to integrate equation 3. At first, the thickness tendency is deduced from a prescribed functional relationship of the type $\partial_t h_k \propto \partial_t \eta$, sometimes referred to as the *coordinate equation* (e.g., Leclair & Madec (2011)) since it completely depends on the analytical formulation of the coordinate transformation. Subsequently, once $\partial_t h_k$ is known, the thickness equation 3 is used to diagnose the dia-surface velocity w.

Introducing a time-invariant model layer thickness $h_k^0(x,y)$ defined for an unperturbed ocean at rest (i.e., when $\eta = 0$) allows one to express the layer thickness as

$$h_k = h_k^0 + \alpha_k \eta, \tag{4}$$

where $0 \le \alpha_k \le 1$ represents the fraction of $\eta(x,y,t)$ assigned to each $h_k(x,y,t)$. While in general this parameter depends on the type of QE vertical coordinate employed, a useful and attractive approach is to develop numerical ocean model code that implements vertical coordinate transformations sharing the same formulation for α_k. In such a way, QE ocean models can be equipped with a general and relatively simple dynamical core that can be used consistently with different types of QE GVCs. This latter property is particularly useful for the localisation method proposed in this paper, as will be explained in the next section.

Modern ocean models typically use an α_k function of $h_k^0\,H^{-1}$ (e.g., Adcroft & Campin (2004); Shchepetkin & McWilliams (2005); Leclair & Madec (2011); Petersen et al. (2015)), resulting in a QE coordinate equation written as

$$\frac{\partial h_k}{\partial t} = \frac{h_k^0}{H}\frac{\partial \eta}{\partial t} = -\frac{h_k^0}{H}\nabla_s \cdot \int_{s(z=-H)}^{s(z=\eta)} h\,\mathbf{u}\,ds = -\frac{h_k^0}{H}\nabla_s \cdot \sum_{m=1}^{N} h_m\,\mathbf{u}_m, \tag{5}$$

where the free-surface equation (neglecting fresh water sources for simplicity) is used to obtain the second equation.

2.2 The localisation algorithm

The localisation method proposed in this paper permits one to embed distinct *local* QE vertical coordinates in different targeted areas of the same model domain Ω, which otherwise employs the *global* Ω^V QE coordinate system. Figure 2 presents an explanatory sketch for the case of two local areas, although there are no restrictions on the total number P of local areas that can be implemented. Here, the red regions Λ_1 and Λ_2 are two *localisation* areas where the model uses Λ_1^V and Λ_2^V QE coordinates, respectively. In addition, the green areas T_1 and T_2 represent *transition* zones where $\mathrm{T}_1^{\mathrm{V}}$ and $\mathrm{T}_2^{\mathrm{V}}$ vertical coordinates result from a smooth relaxation of the local Λ_1^V and Λ_2^V towards the global Ω^V.

While it is desirable to have complete freedom in choosing the localisation areas, it is preferable to apply a generalised algorithm to define the transition areas. For this work we propose a simple method as described in Appendix A.

Once the transition regions have been identified, the following function is used in this study to compute the relaxation weights in the generic transition area T_p (where $1 \le p \le P$):

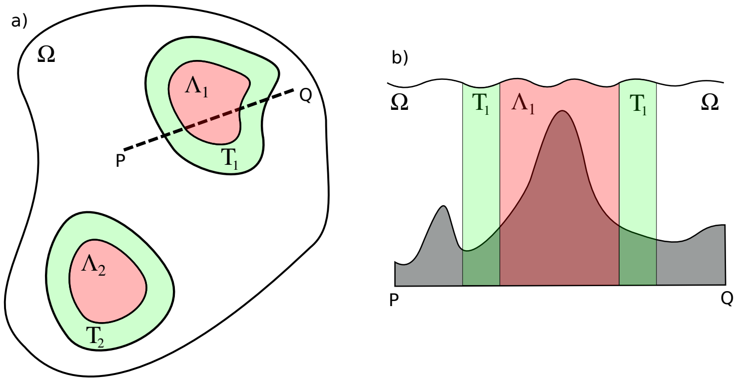

Figure 2. Explanatory sketch of the QE localisation method for the case of two localisation areas - a) is a planar view while b) is a vertical cross-section through line PQ. In the white area Ω the model employs the *global* Ω^V QE GVC, while in the two red regions Λ_1 and Λ_2 the *localised* Λ_1^V and Λ_2^V QE coordinates are used. In the green *transition* zones T_1 and T_2 the vertical coordinates $\mathrm{T}_1^{\mathrm{V}}$ and $\mathrm{T}_2^{\mathrm{V}}$ are computed via equation 7.

$$w_p = \frac{1}{2} + \tanh\left(a\frac{D_p - d_p}{D_p + d_p}\right)\Big[2\tanh(a)\Big]^{-1}. \tag{6}$$

Here, $a = 1.7$ is a tunable coefficient while D_p and d_p are the minimum Euclidean distances of a particular point of the transition zone T_p from its outer and inner boundaries, respectively. Finally, the thickness $h_{k,p}$ of a particular model grid cell included in the area T_p is computed as

$$h_{k,p} = w_p h_{k,\Omega} + (1 - w_p) h_{k,\Lambda_p}, \tag{7}$$

where $h_{k,\Omega}$ and h_{k,Λ_p} are the model cell thicknesses consistent with Ω^V or Λ_p^V GVCs, respectively.

Equation 4 allows QE ocean models to compute h_k in terms of h_k^0, α_k and η. Typically, the calculation of h_k^0 is conducted at the very beginning of a model simulation, either as an 'off-line' pre-processing step or as a single call in the model code just before the beginning of the time-marching stage. Therefore, if Ω^V and Λ_p^V GVCs use a consistent definition for α_k, the QE localisation algorithm can be introduced with minimal changes to the h_k^0 calculation step and no further modifications to the hydrodynamical core of a QE ocean model. In particular, this means that equation 7 can be used only at the beginning of the simulation to compute $h_{k,p}^0$. This is particularly convenient since it permits one to detect any vertical grid set-up issue at a very early stage, saving time in the development and implementation process.

3 The Nordic overflows test-case

In this section, the details of the QE global ocean model used in our numerical experiments (Sec. 3.1) and the three QE GVCs localised in the proximity of the Greenland-Scotland ridge area (Sec. 3.2) are given.

3.1 The eddy-permitting global ocean model

The numerical integrations described in this manuscript are carried out using the GOSI9 global ocean configuration at 1/4° of horizontal resolution (GOSI9-025) developed and used by the UK Met Office Hadley Centre and the National Oceanography Centre under the umbrella of the Joint Marine Modelling Program (see Guiavarc'h et al. (2023) for a detailed description of the model). GOSI9-025 is an eddy-permitting forced ocean configuration based on the Nucleus for European Modelling of the Ocean (NEMO) numerical ocean model at version 4.0.4 (Madec & NEMO-team, 2019).

The model used in this study differs in a few details from the standard GOSI9-025 of Guiavarc'h et al. (2023):

- it is forced with the 1958-2020 JRA-55 atmospheric reanalysis (Kobayashi et al., 2015; Harada et al., 2016) instead of the 1948-2006 CORE atmospheric forcing (Large & Yeager, 2009), to cover the observational period (see Sec. 5);
- it adopts a bottom friction formulation consistent with the "law of the wall" with a bottom roughness $z_0 = 3{\times}10^{-3}$ for a better representation of the bottom boundary layer dynamics;
- it employs the Griffies et al. (1998) triad formulation for the iso-neutral diffusion since it is the only available option for using iso-neutral mixing with inclined GVCs in the current release of NEMO;
- it uses the standard NEMO pressure Jacobian scheme (Madec & NEMO-team, 2019) for a more accurate calculation of the horizontal pressure gradient force when using sloping model levels.

In the vertical direction, GOSI9-025 employs the QE z^*-coordinate of Stacey et al. (1995) and Adcroft & Campin (2004) (see Appendix B for the details) discretised using 75 levels and Madec et al. (1996) stretching function. In addition, in order to mitigate inaccuracies affecting the step-like representation of the bottom topography typical of geopotential-based models, the GOSI9-025 configuration also employs the Pacanowski et al. (1998) partial step parameterisation (see Fig. 3b). Hereafter, the GOSI9-025 model employing standard z^* levels with partial steps (z^*ps) everywhere in the domain is referred to as GOSI9-z^*ps model.

3.2 Localised general terrain-following vertical coordinates

Vertical coordinates smoothly following the seabed topography are able to offer a more realistic representation of gravity currents than models using geopotential coordinates, both in idealised (e.g., Ezer & Mellor (2004); Ezer (2005); Laanaia et al. (2010); Ilcak et al. (2012); Bruciaferri et al. (2018)) and more realistic scenarios (e.g., Käse (2003); Ezer (2006); Riemenschneider & Legg (2007); Seim et al. (2010); Colombo et al. (2020)). Therefore, in this study three different types of QE generalised terrain-following vertical coordinates are localised and tested in the Nordic overflows region.

The localisation area developed for this work includes the Greenland-Scotland ridge region and targets (where possible) the 2800 m isobath (see Fig. 3a), the depth at which ∇H decreases. In this work, the transition area is defined using the algorithm described in Appendix A. The following are the QE GVCs localised and tested in the Nordic overflows region in this paper:

- ***Vanishing quasi-sigma (vqs):*** the vqs method defines vertical coordinates following a smooth envelope topography surface H_e rather than the actual bathymetry H (with $H_e \geq H$), allowing one to reduce the steepness of computational levels with respect to classical terrain-following models (Dukhovskoy et al., 2009). While this approach is particularly effective in reducing errors in the computation

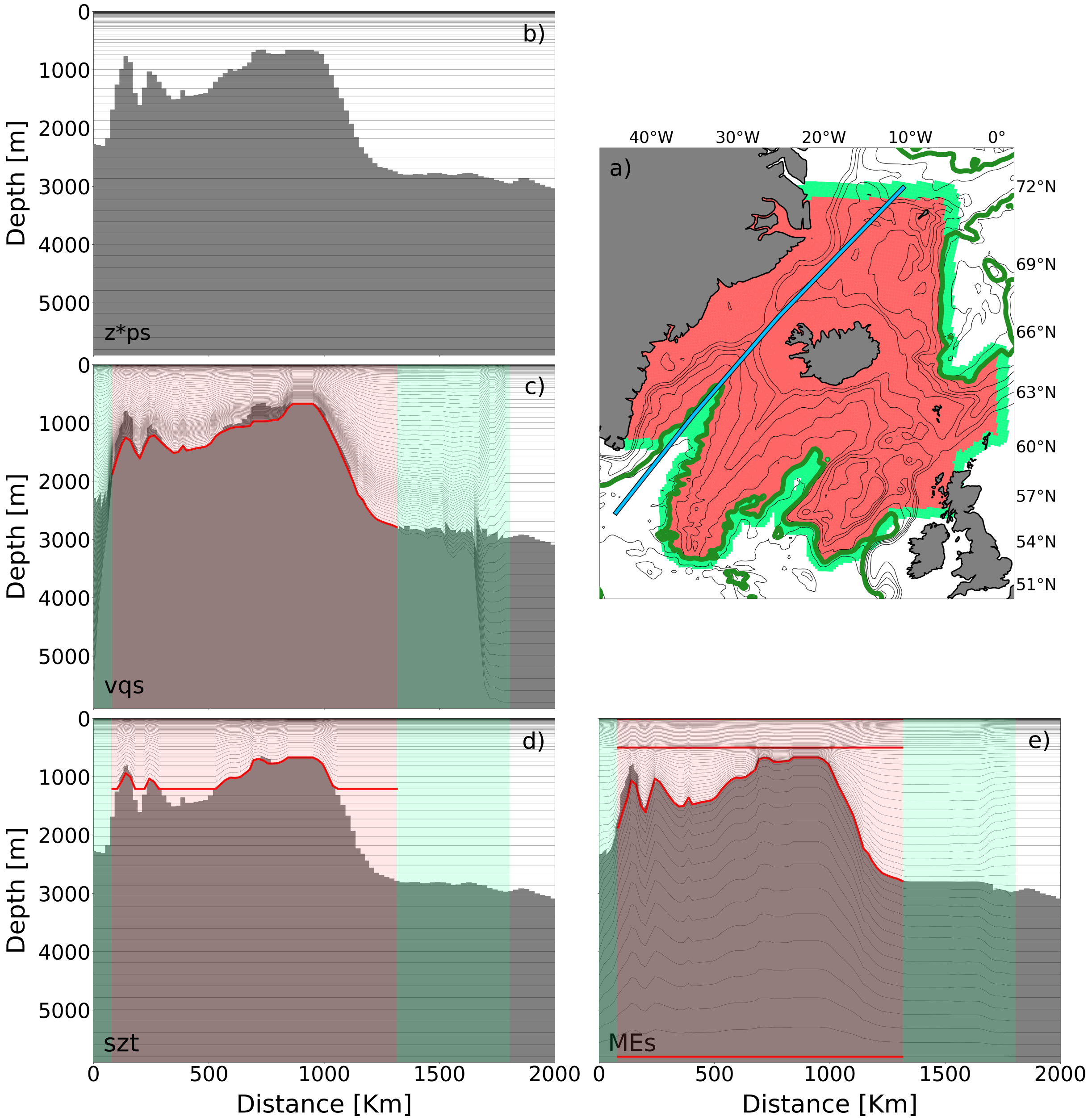

Figure 3. In panel a) the red and green regions represent the Nordic overflows localisation and transition areas used in this study, respectively, while the blue line shows the location of the model bathymetry cross-sections presented in the other panels and the green line marks the 2800 m isobath. Panel b) shows the model bathymetry cross-section extracted from the GOSI9-z^*ps model, panel c) from the GOSI9-vqs model while panel d) and e) from the GOSI9-szt and GOSI9-MEs models, respectively. In panels b) to e) the red lines shows the location of the envelopes used to configure the localised GVCs.

of horizontal pressure gradients (e.g., Dukhovskoy et al. (2009); O'Dea et al. (2012)), it can introduce spurious 'saw-tooth' patterns in the model bathymetry similar to z-level steps whenever $H_e - H$ is large, potentially affecting the accuracy of the simulated bottom dynamics. In this study, we implement local vqs vertical coordinates with a similar setting to Colombo (2018) (see Fig. 3c, Appendix B and Fig. B1b for the details).

- ***Hybrid sz-transitioning (szt):*** the szt scheme described in Wise et al. (2021) defines QE levels that follow a smooth envelope bathymetry H_e above a user-defined depth while smoothly transition into z^*-interfaces with partial steps at greater depths, effectively allowing one to combine vqs and z^* QE coordinates. In this study, we configure the local szt vertical discretisation scheme to use terrain-following levels up to $\approx 1200\ m$ (see Fig. 3d, Appendix B and Fig. B1c for the details on the configuration).

- ***Multi-Envelope s-coordinates (MEs):*** the ME method defines QE coordinate interfaces that are curved and adjusted to multiple arbitrarily defined surfaces (aka envelopes) rather than following geopotentials, the actual bottom topography or a single-envelope bathymetry as in the case of vqs or szt GVCs. In such a way, computational levels can be optimised to best represent different physical processes in different sub-domains of the model while minimising horizontal pressure gradient (HPG) errors (Bruciaferri et al., 2018, 2020; Wise et al., 2021; Bruciaferri et al., 2022). In this study, local MEs-coordinates are configured using four envelopes (see Fig. 3e, Appendix B and Fig. B1d for the details on the coordinate transformation and the set-up), so that in the Nordic overflows region model levels are nearly terrain-following to a depth of $2800\,m$.

Hereafter, the models using local vqs, szt and MEs GVCs in the Nordic overflow region are simply referred to as GOSI9-vqs, GOSI9-szt and GOSI9-MEs models.

In this study, the envelope bathymetry surfaces of the GOSI9-vqs and GOSI9-szt models or the generalised envelopes used by the GOSI9-MEs model were smoothed via the Martinho & Batteen (2006) iterative procedure. Such an algorithm aims at ensuring that the slope parameter $r = |\delta H|(2\bar{H})^{-1}$, with δH the horizontal change in H of adjacent model cells and $\bar{H}$ the mean local bottom depth (Mellor et al., 1998), is below a user defined threshold r_{max} (see Appendix C for the details on the procedure used in this paper).

Since szt-coordinates are nearly terrain-following only up to a certain prescribed depth, a more relaxed r_{max} value can be potentially applied in comparison to a similar configuration using local vqs-levels, resulting in a less smoothed envelope bathymetry. This can allow one to keep HPG error below an acceptable level while significantly reducing spurious 'saw-tooth' structures in the model bathymetry.

The ME method allows for a 3D varying maximum slope parameter r_{max}, effectively permitting to smooth the envelopes only where it is needed for maintaining HPG errors below an acceptable level. In such a way, the generation of undesired 'saw-tooth' patterns and 'step-like' structures can be significantly reduced in comparison to vqs and szt approaches. The ME approach offers great freedom in the configuration of the vertical grid, allowing one to directly control the design of model levels in each sub-zone of the vertical domain.

4 Idealised numerical experiments

Two different types of idealised numerical experiments are conducted in this study. The first one assessed whether the localised terrain-following grids can accurately compute HPGs (Sec. 4.1), a basic requirement for a robust numerical mesh that will be used for realistic oceanic simulations. The second numerical experiment evaluates the ability of the various GVCs to reduce numerical diapycnal mixing when simulating overflows (Sec. 4.2).

4.1 Errors in the computation of pressure forces

HPG errors affecting computational vertical grids are typically assessed via the classical HPG test of Haidvogel & Beckmann (1999). In this idealised numerical experiment, the ocean model is initialised at rest (i.e., $\mathbf{u} = 0$, $\eta = 0$) with a horizontally uniform stratification $\rho(z)$ so that initial horizontal density gradients are nil. In the absence of any external forcing and explicit tracers diffusion, the analytical solution for the ocean currents in this type of problem is 0 $m\,s^{-1}$. However, when using generalised $s(x, y, z, t)$ coordinates the horizontal pressure gradient $\nabla_z p$ (with $\nabla_z = (\partial_x|_z, \partial_y|_z, 0)$) becomes the result of two sizeable terms

$$\nabla_z p = \nabla_s p + \rho g \nabla_s z. \tag{8}$$

In the discrete limit, both terms on the right hand side of equation 8 are affected by distinct numerical errors that generally do not cancel, generating spurious pressure forces that drive non-trivial unphysical currents (Haney, 1991; Mellor et al., 1994; Ezer et al., 2002).

The control z^*ps model and the three GOSI9-vqs, GOSI9-szt and GOSI9-MEs models are initialised with the temperature and salinity vertical profiles shown in Fig. 4a. These synthetic profiles were suggested by Wise et al. (2021) as representative of the summer stratification in the deep eastern North Atlantic. Numerical simulations were integrated for one month with no external forcing.

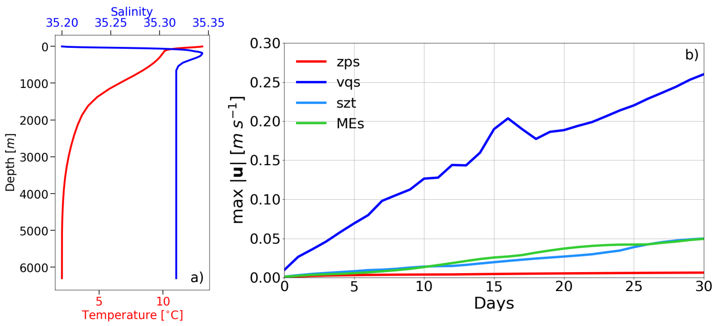

Figure 4. a) Wise et al. (2021) temperature (red) and salinity (blue) synthetic profiles used to initialise HPG experiments. b) Time evolution of the maximum HPG error $|\mathbf{u}|$ for the z^*ps (red), GOSI9-vqs (blue), GOSI9-szt (light blue) and GOSI9-MEs (light green) models.

Figure 4b presents the daily timeseries of the maximum HPG error $|\mathbf{u}|$ for the four models. The z^*ps model shows the smallest HPG error ($< 0.005\ m\,s^{-1}$, in agreement with previous studies, e.g., Bruciaferri et al. (2018); Wise et al. (2021)) while the vqs model the largest ($> 0.25\ m\,s^{-1}$). In the case of the GOSI9-szt and GOSI9-MEs models spurious currents are $\leq 0.05\ m\,s^{-1}$.

The envelopes of the three localised terrain-following GVCs are optimised to have HPG errors $< 0.05\ m\,s^{-1}$ (see Appendix C for the details). For the GOSI9-szt and GOSI9-MEs models, this is in agreement with the results presented in Fig. 4b. However, in the case of the vqs model, spurious currents are much larger than the optimisation threshold. In order to understand the reason behind this result, Fig. 5 shows, for each grid point of the horizontal grid, the maximum in the vertical and time HPG error $|\mathbf{u}|$ for the three models using localised QE GVCs.

In the case of the GOSI9-szt and GOSI9-MEs models, HPG errors affects only the localisation area (red area in Fig. 3a), as expected. To the contrary, the vqs model presents large spurious currents in the proximity of the transition area (green region in Fig. 3a). Since the local-vqs approach relies on one single envelope bathymetry, the mismatch in depth between vqs and z^* model levels sharing the same k index can be quite large ($\approx$ 3500 m in the case of the last model level), resulting in two important consequences for the transition zone (see Fig. 3c and B1b). Firstly, computational surfaces will be particularly steep in the relaxation area, driving large HPG errors that can not be mitigated by limiting the slope parameter of the envelope bathymetry. Secondly, significant 'saw-tooth' patterns will be generated in the model bathymetry of the transition zone, introducing unrealistic spurious noise at the model grid scale. In agreement with Colombo (2018), we note that while the large HPG errors could be reduced by implementing a much wider and hand-adjusted transition area, the generation of undesired bathymetric noise in the relaxation zone appears to be a much harder problem to solve.

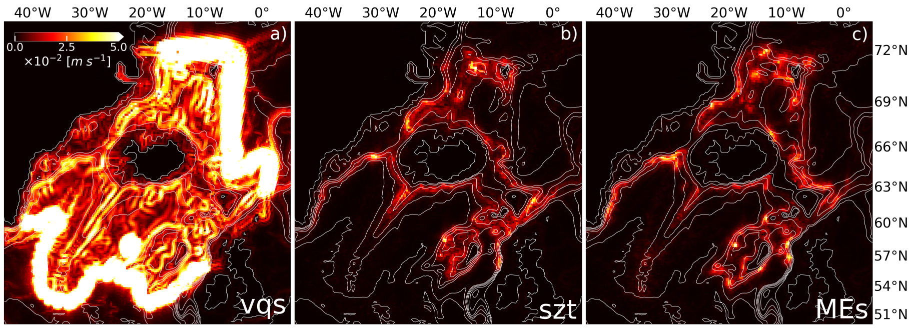

Figure 5. Maps of the maximum in the vertical and time spurious currents $|\mathbf{u}|$ $m\,s^{-1}$ after a 1 month long HPG numerical experiment for the models using localised vqs (a), szt (b) and MEs (c) GVC.

Neither the GOSI9-szt nor GOSI9-MEs models suffers from the same issues affecting local-vqs coordinates. For example, because at depth the szt approach uses the same vertical coordinate formulation of the global domain, the GOSI9-szt bathymetry in the transition zone is effectively discretised with z^*ps levels (see Fig. 3d and B1c), resulting in a smooth transition zone. Similarly, since the ME approach divides the model vertical space in sub-zones, model levels can be easily distributed along the water column to obtain a smooth transition zone free of HPG errors (see Fig. 3e and B1d and Appendix B). Given the large HPG errors affecting the GOSI9-vqs model, we conclude that the vqs approach is not suitable for the localisation method proposed in this manuscript and we continue our study only with the GOSI9-szt and GOSI9-MEs models.

4.2 Diapycnal mixing in an idealised overflow

Models with a stepped bottom topography introduce excessive numerical mixing when simulating dense gravity currents. This is the case especially at coarse horizontal resolutions such as the one used in this study, even when the partial steps parameterisation is employed (e.g., Legg et al. (2006)). Contrarily, terrain-following levels can offer a smooth representation of the sea bed, facilitating more realistic simulations of bottom intensified currents (e.g. Ezer & Mellor (2004)). The aim of this second set of idealised experiments is to evaluate the ability of localised GVCs to reduce spurious entrain-

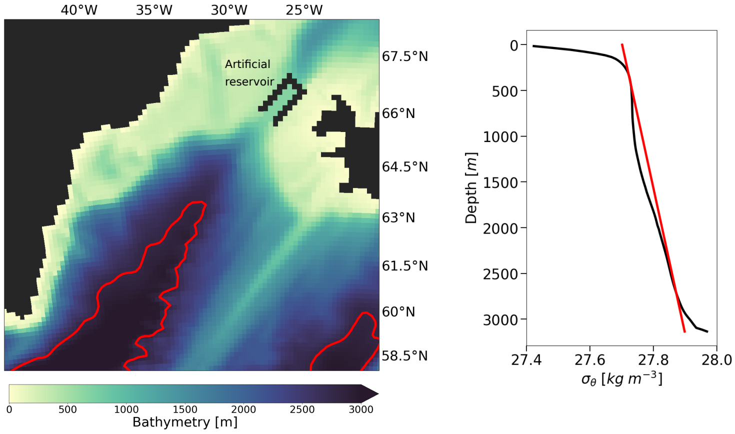

Figure 6. a) In the idealised overflow experiment, the original model bottom topography is modified to include an artificial reservoir in the proximity of the Denmark Strait. In red it is also shown the 2800 m isobath defining the boundary of the localisation area. b) Density vertical profile from OSNAP observational array in the Irminger Sea (black) compared against the analytical density profile (red) used to initialise the idealised overflows experiments.

ment and diapycnal mixing when simulating gravity currents generated by a dam-break in the Denmark Strait.

Numerical experiments are set as follows. The original model bathymetry is modified by introducing an artificial reservoir in the proximity of the Denmark Strait sill, as shown in Fig. 6a. Then, the model uses a linear equation of state (only function of temperature) and is initialised with a horizontally uniform ambient stratification $\rho(z)$ that linearly fits the observed density distribution in the middle of the Irminger Sea, as shown in Fig. 6b - observations are provided by the Overturning in the Subpolar North Atlantic Program (OSNAP, M. S. Lozier et al. (2017, 2019)). Such an initial condition is perturbed by introducing a cold dense water mass with density ρ_d such that $\Delta\rho = \max\{\rho_d - \rho(z)\} = 1.3\ kg\,m^{-3}$ inside the artificial reservoir. As already noted by Ezer (2006), this value for $\Delta\rho$ is somewhat larger than the ones observed in reality. However, one has to keep in mind that our simulations are lock-exchange gravity currents where the only forcing is represented by the buoyancy anomaly of the dense perturbation in the artificial reservoir. Therefore, $\Delta\rho$ needs to be large enough to promote a down-slope dense cascade that will continue even after the inevitably strong mixing at the beginning of the simulation. We emphasize that the aim of this second idealised experiment is to evaluate the impact of the vertical coordinate system on the simulation of a gravity current in the Denmark Strait, and not to reproduce observed properties of the overflow in this region.

In order to keep track of the cascading dense plume and facilitate our analysis, we use a passive tracer whose initial concentration C is 10 in the the cold dense water mass of the artificial reservoir while zero elsewhere. Computations are integrated for 90 days without any external forcing and using the standard GOSI9-025 setting for the numerics and the physics (Sec. 3.1), except for the use of the linear equation of state. In particular, ambient fluid entrainment and vertical mixing are explicitly taken into account by using the standard NEMO turbulent kinetic energy (TKE) scheme (see Guiavarc'h et al. 2023 for the details).

Dilution of the tracer concentration C is an indication for entrainment and mixing in of ambient fluid in the dense cascading water (Ezer, 2005; Legg et al., 2006). We define the overflow water to be the fluid with $C \geq 0.1$ and Fig. 7 and 8 show snapshots

Figure 7. Passive tracer concentration at the bottom (upper row) and in a cross sections passing through the dense plume (bottom row) for the z ps, GOSI9-szt and GOSI9-MEs models after 30 days. Only wet cells with passive tracer concentration $C \geq 0.1$ are shown. The location of the cross section is shown in light blue in the inset. The thick red and black lines identify the 2800 m and 1200 m isobaths, respectively.

of the tracer concentration at the deepest wet cell just above the bottom topography (top row) and in a vertical cross section along the plume path (bottom row) for the three models after 30 and 90 days, respectively. All the three models simulate a dense water plume descending down the steep continental slope of the northern Irminger Sea basin which reaches the 2800 m after 90 days. However, their respective solutions for the passive tracer concentration distribution differ significantly.

The control z ps model produces the most diluted overflow (Fig. 7a, d and Fig. 8a, d), indicating large ambient fluid entrainment and mixing, in agreement with previous studies (e.g., Ezer (2005); Bruciaferri et al. (2018)). In the case of the GOSI9-MEs model, diapycnal mixing is significantly reduced, allowing the simulation of a much less diluted dense plume which after 90 days can reach the 2800 m isobath with up to 45% of the initial passive tracer concentration (see Fig. 8c and f). The GOSI9-szt model is able to reduce the large mixing in the first third of the simulation, reproducing a passive tracer concentration distribution similar to the one of the GOSI9-MEs model (Fig. 7b and e). However, the relatively shallow (1200 m) transition to a stepped topography leads to an increase in diapycnal mixing in the last two thirds of the simulation, slowing down and importantly diluting the GOSI9-szt overflow (Fig. 8b and e).

Qualitative examination of Fig. 7 seems to suggest that the three models may also differ in the way they represent the evolving dynamics of the dense plume. At the beginning of the simulation, the three models agree simulating a coherent down-slope cascading. However, after crossing the 1000 m isobath, the overflow reproduced by the z ps and GOSI9-szt models seem to move prevalently in the along-slope direction, with the bulk of the dense plume reaching a depth of 2000 m after 30 days (see Fig. 7a and b). In the case of the GOSI9-MEs model, after 30 days the head of the dense plume has crossed the 2500 m, indicating a larger down-slope component of the velocity. This is probably partly due to the fact that GOSI9-MEs model, with its increased resolution near the sea bed, is able to better resolve the Ekman transport at the bottom boundand Tab. 2). However, the analysis of the active tracers fields indicate that large biases consistently affect the DSOW represented by the three models (see Fig. 11a.2, b.2, c.2 and d.2, Fig. 11a.3, b.3, c.3 and d.3 and Tab. 2), with mean salinity errors > 0.1 and average warm biases > 1.0 °C. The three models also underestimate the DSOW mean volume transport in the DS section (differences are ≈ 1 Sv, see Tab. 2).

In the proximity of the IFR section, the GOSI9-z^*ps and GOSI9-MEs models simulate ISOW with mean hydrographic properties very similar to the observations (warm bias of $\approx$ 0.1 °C and average absolute salinity errors $<$ 0.01), resulting in marginally less dense (≈ 0.01 $kg\,m^{-3}$) overflows water masses (see Fig. 11$e.^*$, $f.^*$, $g.^*$ and $h.^*$ and Tab. 2). In the case of the GOSI9-szt model, results present moderately larger errors, with average values of ≈ 0.5 °C for temperature, ≈ 0.025 for salinity and ≈ 0.02 $kg\,m^{-3}$ for density. For the mean volume transport (see Tab. 2), the GOSI9-MEs model results to be the more accurate (errors < 1.0 Sv) while the GOSI9-z^*ps and GOSI9-szt models present larger biases (> 1.5 Sv).

In the case of the FSC section, only climatological hydrographic observations from Hansen & Østerhus (2000); Hughes et al. (2006) were accessible in this study, while direct estimations of the overflows volume transport were available only for the two farthest downstream FBC and WTR sections. In the FSC section, the GOSI9-szt model simulates an ISOW that is moderately warmer and saltier than the observations (mean absolute errors of ≈ 0.7 °C and ≈ 0.06, respectively), while the GOSI9-z^*ps and GOSI9-MEs models show much reduced biases (mean absolute errors $<$ 0.2 °C for temperature and $\leq$ 0.02 for salinity, see also Fig. 11$i.^*$, $j.^*$, $k.^*$, $l.^*$ and Tab. 2). For the volume transport (see Tab. 2), the three models are in good agreement with the observations in the case of the FBC section; in the WTR transect, the GOSI9-szt model presents the highest accuracy while the GOSI9-MEs model shows large differences with the observations and the GOSI9-z^*ps model totally misses this secondary path of the Nordic overflows.

There are two key points to draw from this Section. Firstly, we note that similar biases in temperature, salinity and transport seem to affect the three models, with larger magnitude in the Greenland-Iceland ridge (i.e., the DS section) than in the Iceland-Scotland ridge (i.e., the FSC, FBC, IFR and WTR sections). Secondly, we observe that in general the local MEs GVC seems to have a small positive impact on the mean properties of the overflows upstream, while using local szt levels seems to somewhat degrade the properties of the simulated DSOW and ISOW, especially in the case of the FSC and IFR sections.

5.3 Dense overflows downstream the Greenland-Scotland Ridge

We continue our analysis assessing the properties of the Nordic overflows simulated by the three models downstream the Greenland-Scotland ridge. Table 3 compares the 2014$-$2018 time-averaged values of measured and simulated mean overflows hydrographic properties in the IS and IB sections and the overflows volume transport in the IS, IB and CGFZ sections (see Tab. 1 for more details and Fig. S3 and Fig. S4 of the Supporting Information for the actual time-series). Moreover, Fig. 12 presents the 2014$-$2018 averaged potential density anomaly, temperature and salinity fields observed and simulated by the three models along the OSNAP East array (M. S. Lozier et al., 2017; Li et al., 2023), which includes the Irminger Sea (IS) and the Icelandic Basin (IB) sections. Downstream the Greenland-Scotland ridge we use a density threshold σ_θ^{ovf} of 27.84 $kg\,m^{-3}$ to identify the modified DSOW and ISOW water masses (see Sec. 5.1 for the details).

In the IS section, the GOSI9-MEs model is able to reproduce a modified overflow water mass which is in good agreement with the observations for the density (mean absolute error is < 0.003 $kg\,m^{-3}$). Contrarily, in the case of the GOSI9-z^*ps and GOSI9-szt simulations the deep waters are less dense than measurements, with an average ab-

Section ID	Variables	Observations	GOSI9-z^*ps	GOSI9-szt	GOSI9-MEs
IS	$\langle T^\star \rangle$ [°C]	2.52 ± 0.02	2.83 ± 0.03	2.93 ± 0.01	2.82 ± 0.01
	$\langle S^\star \rangle$	34.93 ± 0.00	34.94 ± 0.00	34.95 ± 0.00	34.96 ± 0.00
	$\langle \sigma_\theta{}^\star \rangle$ [$kg\,m^{-3}$]	27.87 ± 0.00	27.86 ± 0.00	27.86 ± 0.00	27.87 ± 0.00
	$\langle \Psi^\star \rangle$ [Sv]	-2.5 ± 1.4	-0.7 ± 1.4	-3.7 ± 1.2	-1.6 ± 1.1
IB	$\langle T^\star \rangle$ [°C]	2.82 ± 0.01	3.27 ± 0.08	3.11 ± 0.04	2.77 ± 0.03
	$\langle S^\star \rangle$	34.97 ± 0.00	34.99 ± 0.01	34.98 ± 0.00	34.98 ± 0.01
	$\langle \sigma_\theta{}^\star \rangle$ [$kg\,m^{-3}$]	27.88 ± 0.00	27.85 ± 0.00	27.86 ± 0.00	27.89 ± 0.00
	$\langle \Psi^\star \rangle$ [Sv]	-4.1 ± 1.0	-0.7 ± 0.5	-1.8 ± 0.8	-3.1 ± 0.4
CGFZ	$\langle \Psi^\star \rangle$ [Sv]	-1.7 ± 0.5	$+0.2 \pm 0.7$	-0.1 ± 0.9	-0.8 ± 1.1

Table 3. Time averaged (mean ± SD) temperature ($\langle T^\star \rangle$), salinity ($\langle S^\star \rangle$), potential density anomaly ($\langle \sigma_\theta{}^\star \rangle$) and transport ($\langle \Psi^\star \rangle$) of overflow water masses ($\sigma_\theta^{ovf} = 27.84\ kg\,m^{-3}$) estimated from observations and simulated by the models in the IS, IB and CGFZ downstream sections.

solute bias $> 0.01\ kg\,m^{-3}$ (see upper rows of Fig. 12 and Tab 3). Our analysis also shows that important positive biases in temperature (> 0.3 °C) and salinity (> 0.01) affect the three models (see middle and bottom rows of Fig. 12 and Tab 3). In the case of the transport, the 2014−2018 mean DSOW volume transport simulated by the GOSI9-MEs model is the most similar to the one estimated from OSNAP observations, followed by the ones of the GOSI9-szt and GOSI9-z^*ps models.

The results for the overflow density in the IB section are similar to the ones of the IS section, with the GOSI9-MEs model being the only one able to reproduce deep dense water masses with $\sigma_\theta > 27.88\ kg\,m^{-3}$ as the observations (see upper rows of Fig. 12 and Tab. 3). In addition, all three models present a mean positive bias > 0.01 for the overflow salinity in the IB section (see bottom rows of Fig. 12 and Tab. 3); for the temperature (see middle rows of Fig. 12 and Tab. 3) the GOSI9-z^*ps and GOSI9-szt simulations show warm biases of ≈ 0.4 °C and ≈ 0.3 °C, respectively, while the GOSI9-MEs model is in very good agreement with the observations (mean absolute bias ≈ 0.05 °C). Regarding the volume transport, the mean estimate from the GOSI9-MEs simulation is the closest to the one from observations (difference is ≈ 1 Sv), while GOSI9-z^*ps and GOSI9-szt mean values present larger biases (see Tab. 3).

In the case of CGFZ section, no hydrographic observations were available for this study and the mean volume transport estimate of Xu et al. (2018) is used. For the GOSI9-z^*ps model, a small mean transport in the opposite direction of the observations exists (see Tab. 3), while the GOSI9-szt simulation reproduces a mean transport that agrees with the observations in direction but is significantly weaker. In contrast, the GOSI9-MEs model represents a northward volume transport that better agrees with published estimates of magnitude (see Tab. 3).

In agreement with the findings of the idealised overflow experiment of Sec. 4.2, this Section demonstrates that the type of vertical coordinates has a large impact on the accuracy of the simulated overflows downstream the Greenland-Scotland ridge. Using local ME terrain-following levels seems to allow the model to quickly recover from the large inaccuracies of the initial condition at depth (see Fig. S3 of the Supporting Information for more details) and reproduce deep overflow water masses that are similar in density to the observations. Conversely, using a step-like bottom topography (either fully as in the control GOSI9-z^*ps model or only at depths $> 1200\ m$ as in the GOSI9-szt simulation) seems to introduce large spurious diapycnal mixing, excessively diluting the overflows along their descending paths. The shallow transition from smooth to stepped bathymetry of the GOSI9-szt model seems to mitigate some overflows biases (e.g. volume transport or hydrography in the IB), while having small negative impact on others (e.g. hydrography in the IS).

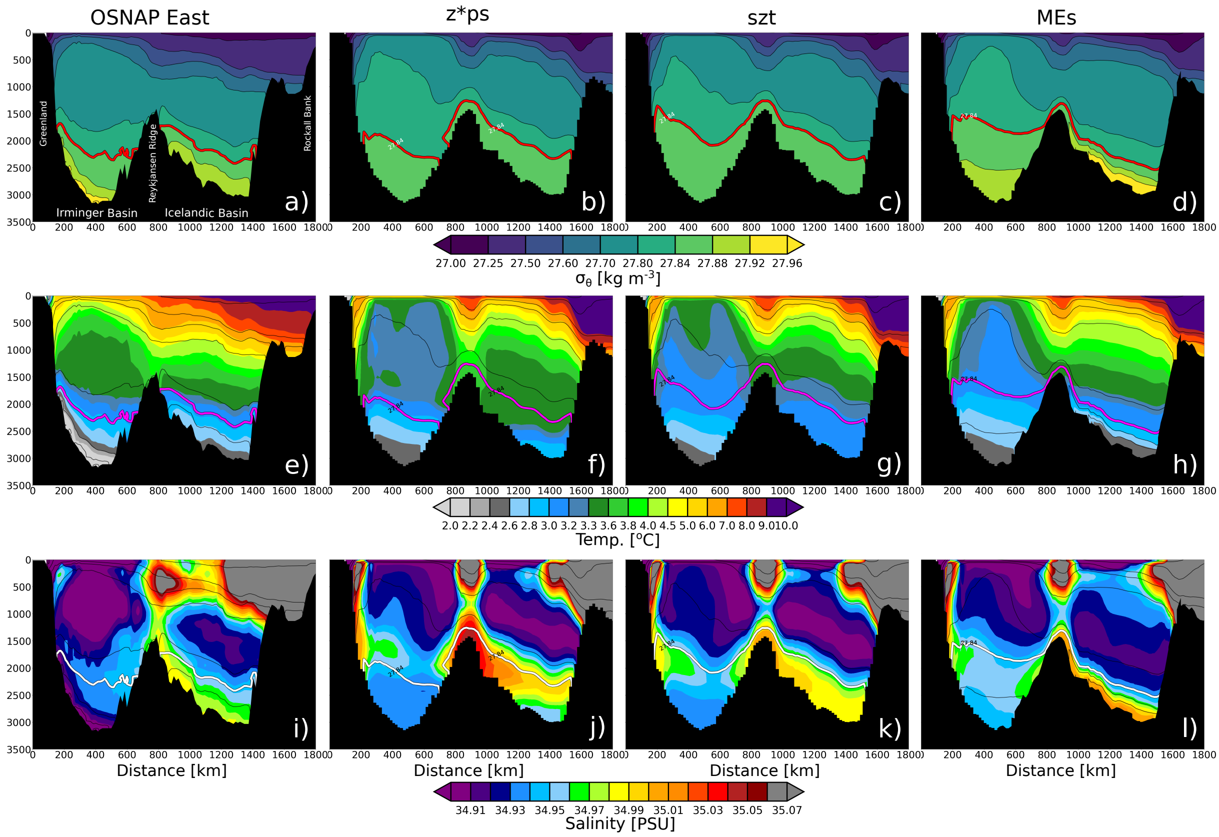

Figure 12. Potential density anomaly (upper row), temperature (middle row) and salinity (bottom row) fields observed (1^{st} column) and simulated by the GOSI9-z^*ps (2^{nd}), GOSI9-szt (3^{rd} column) and GOSI9-MEs (4^{th} column) models in the Irminger Sea (IS) and Icelandic Basin (IB) cross-sections (see Fig. 1 for their locations). The red, magenta and white lines show the 28.84 $kg\,m^{-3}$ isopycnal.

Our analysis also shows that important biases seems to affect the downstream hydrography of the overflows simulated by the three models, with discrepancies from observations that are buoyancy compensated and sometimes larger in the case of the models using localised GVCs (e.g. salinity in the IS section of the GOSI9-szt and GOSI9-MEs models).

5.4 Hydrographic biases at the bottom and overflow pathways

The aim of this Section is to better understand the origin of the large upstream and downstream biases presented in Sec. 5.2 and Sec. 5.3. Figure 13 compares the 2014−2018 bottom temperature and salinity fields simulated by the GOSI9-z^*ps, GOSI9-szt and GOSI9-MEs models in the Nordic overflows region against the ones from the 2005−2017 WOA18 climatology (Boyer et al., 2018) while Fig. 14 presents the inter-models' differences for the bottom hydrography.

The GOSI9-z^*ps model shows important bottom biases in both basins (Fig. 13b and f). The bottom temperature of the deep part of the IS and along the continental slope of Greenland is generally significantly warmer than WOA18 climatology, with errors between ≈ 0.7 °C and 1.2 $°C$. Similarly, at the bottom of the IB and along the east flank of the RR a warm bias of $\approx 0.5-0.7$ °C exists. The GOSI9-z^*ps bottom waters show also a strong salinity bias at depths around $1500-2000$ m along the continental

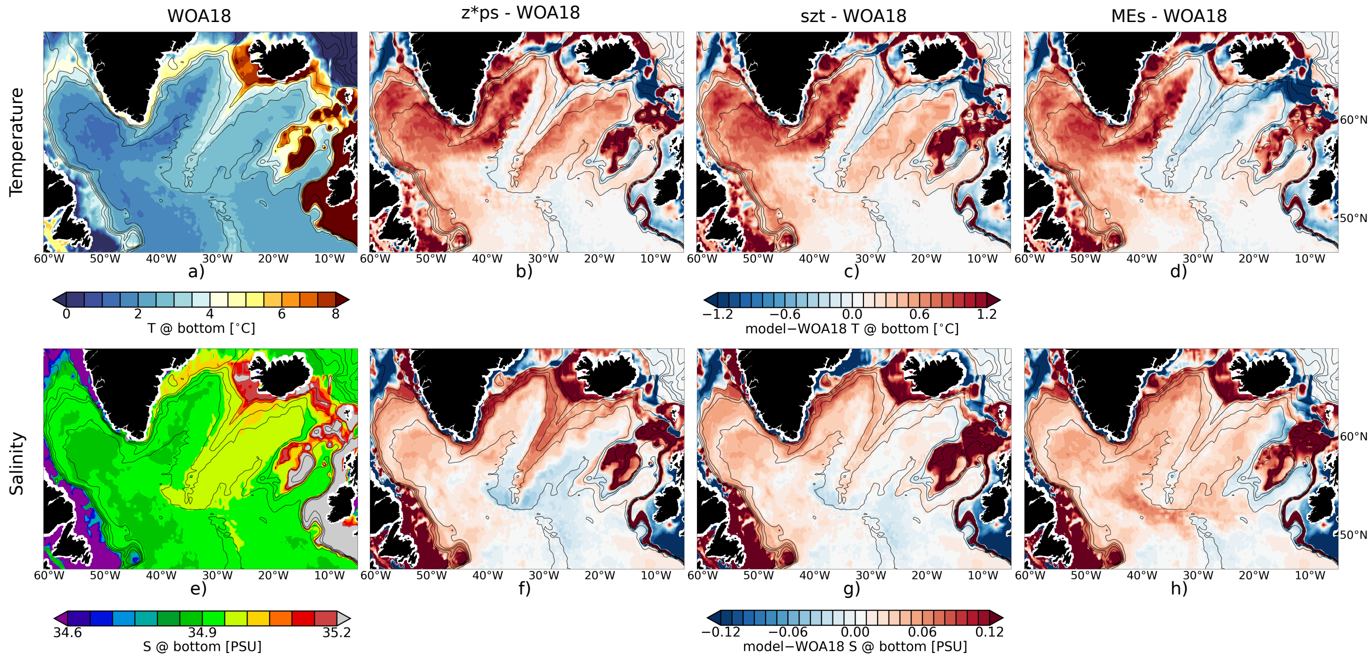

Figure 13. *Upper row*: bottom temperature field in the Nordic Seas region from 2005-2017 WOA18 climatology (a) and differences (model-WOA18) with GOSI9-z^*ps (b), GOSI9-szt (c) and GOSI9-MEs (d) models. *Bottom row*: same as in the *upper row* but for the bottom salinity. Black thin lines identify the 500 m, 1000 m, 1500 m, 2000 m and 3000 m isobaths.

slope of both the IS and IB, with errors of $\approx 0.07 - 0.10$ and $\approx 0.04 - 0.06$, respectively. Noteworthy, at larger depths the GOSI9-z^*ps bottom salinity is far more similar to the WOA18 climatology in both basins, with average differences ≤ 0.01.

In the case of the GOSI9-MEs model, the bottom temperature is significantly more accurate than the other two models (Fig. 13d), with improvements over the GOSI9-z^*ps model $\geq$ 0.5 °C in the IB and in the range $\approx$ 0.1 $-$ 0.5 °C for the bottom temperature along the continental slope of Greenland at depths around $1000-2500$ m. In the deepest part of the IS the three models seem to be equivalent for the bottom temperature, with differences that are ≤ 0.1 °C (see Fig. 13 and Fig. 14). For salinity, the GOSI9-MEs model presents a bottom positive salinity bias at depths ≥ 2000 m in both the IS and IB, with errors that are between $0.2 - 0.7$, up to $\approx$ 0.06 larger than the GOSI9-z^*ps error. Contrarily, for depths between $\approx 1000-2000$ m along the continental slope of both the IS and IB the GOSI9-MEs model shows better accuracy for the bottom salinity than the control GOSI9-z^*ps model, with improvements in the $\approx 0.2 - 0.5$ range.

The GOSI9-szt model presents temperature and salinity differences with the GOSI9-z^*ps model that are generally similar to the ones of the GOSI9-MEs model in terms of spatial distribution, but typically much weaker (see Fig. 13c and g and Fig. 14a, c, d and f). In particular, the bottom temperature of the GOSI9-MEs model shows improvements over the GOSI9-szt model ≥ 0.5 °C in the IB and up to ≈ 0.3 °C in the IS for depths between $2000 - 2500$ m (Fig. 14c). In the case of salinity, the GOSI9-szt and GOSI9-MEs models show similar improvements (average differences are $<$ 0.01) over the GOSI9-z^*ps model along the continental slope of the IS and IB for depths in the range $\approx 1000 - 2000$ m, while at larger depths the GOSI9-MEs model show higher salinity biases.

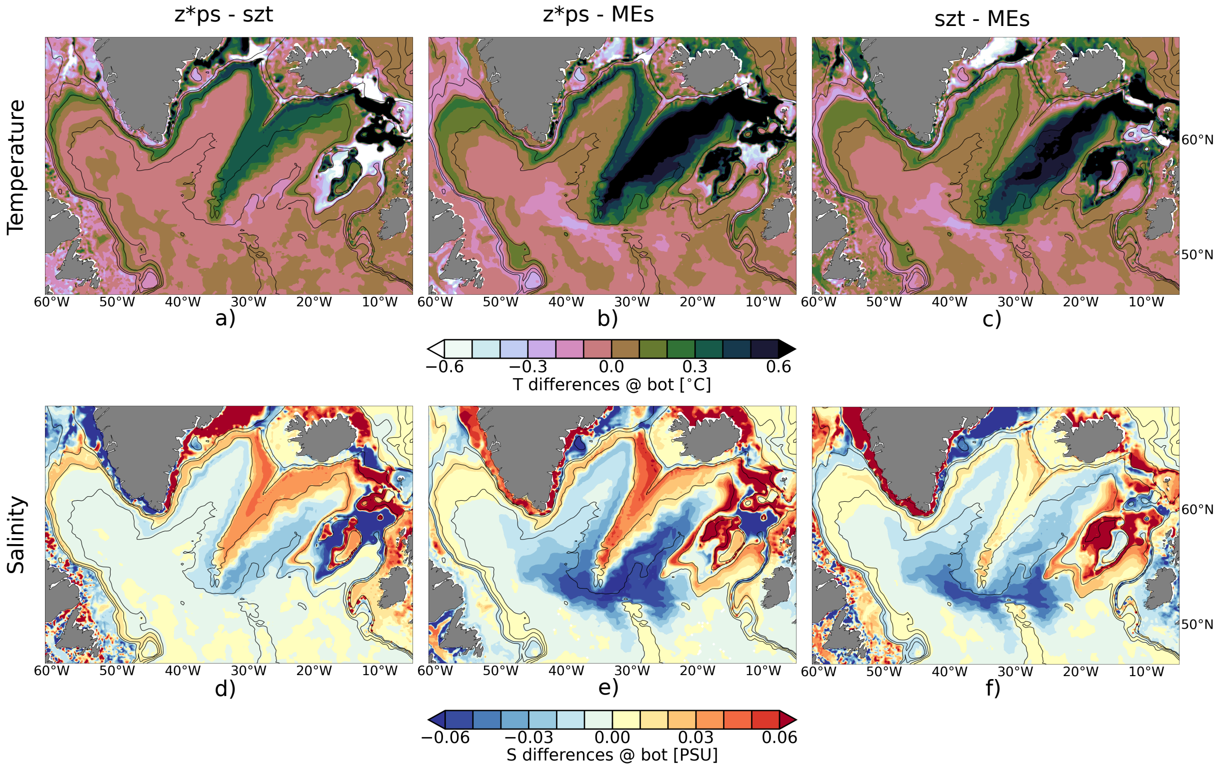

Figure 14. Differences between the control GOSI9-z^*ps model and the GOSI9-szt and GOSI9-MEs models for the bottom temperature (*upper row*) and salinity (*bottom row*). Black thin lines identify the 500 m, 1000 m, 2000 m and 3000 m isobaths.

We continue the analysis presenting in Fig. 15 maps of the volume transport and layer thickness of the overflowing dense waters ($\sigma_\theta \geq 27.84\ kg\, m^{-3}$) as reproduced by the three models.

The ISOW of the GOSI9-MEs simulation is in good agreement with observations, descending along the east flank of the RR and the deep part of the basin and leaving the IB via gaps in the RR or flowing through the CGFZ (see Fig. 1), as shown by the circulation patterns of Fig. 15c and the spreading pathways of the differences for the bottom tracers between GOSI9-MEs and GOSI9-z^*ps models of Fig. 14b and e (the latter are also in very good agreement with the overflow pathways analysis presented in figure 3 of S. M. Lozier et al. (2022)).

To the contrary, in the GOSI9-z^*ps and GOSI9-szt models the IB overflow flows along a narrower part of the east side of the RR, presents a weaker transport (especially in the control model) and leaves the IB only via the RR, with no circulation through the CGFZ (see Fig. 15a and b, Fig. 14a and Tab. 3).

In the IS, the GOSI9-z^*ps model simulates a narrow and thin overflow water mass flowing along the continental slope of Greenland with weak transport and confined below the 2000 m isobath, while in the GOSI9-szt experiment the DSOW flow is much stronger and intersects the $\approx 1000 - 2000\ m$ depth range. The GOSI9-MEs model reproduces a DSOW flowing at depths $\geq 2000\ m$ as the GOSI9-z^*ps model but with a much stronger transport similar to the one of the GOSI9-szt simulation.

In general, the net southward transport reproduced by the GOSI9-szt and GOSI9-z^*ps models in the IS is significantly larger than the one of the GOSI9-MEs simulation (see Fig. 10a). As already suggested by the idealised experiments, this can be partially

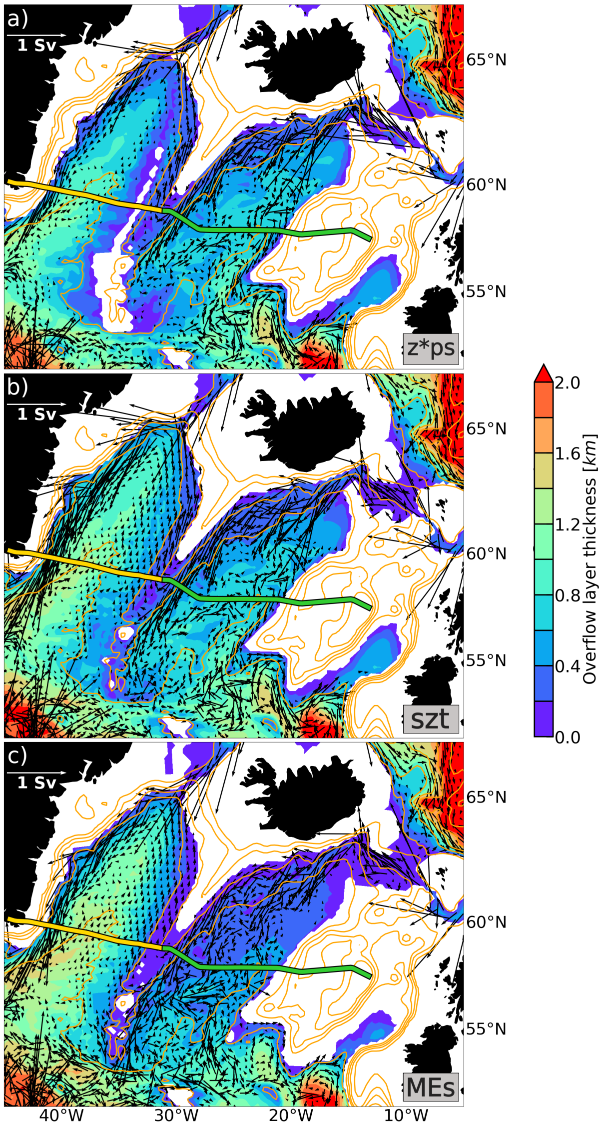

Figure 15. Layer thickness and associated volume transport of overflowing dense waters ($\sigma_\theta \geq 27.84\ kg\,m^{-3}$) for the GOSI9-$z^*$ps (a), GOSI9-$szt$ (b) and GOSI9-MEs (c) models. Thick yellow and green lines show the location of the IS and IB sections, respectively. Thin yellow lines present the 500 m, 1000 m, 1500 m, 2000 m and 3000 m isobaths

.

attributed to the fact that in the GOSI9-MEs model the Ekman bottom transport is better represented, breaking geostrophy and hence increasing the down-slope component of the flow. The net southward transport of the GOSI9-z^*ps model between 27.80-27.85 presented in Fig. 10a is much larger than the ones of the other two models: this is probably a consequence of the fact that in the GOSI9-z^*ps model the deep northward flow entering the IS is very weak, as shown by Fig. 15a.

5.5 The impact of vertical coordinates and model biases on overflows simulations

The tracers biases at the bottom and overflow pathways described in Sec. 5.4, together with the analysis of the upstream and downstream hydrography and transport presented in Sec. 5.2 and Sec. 5.3 indicates the following mechanisms for the impact of model biases and type of vertical coordinates on the overflows properties.

The three models simulate an ISOW crossing the Greenland-Scotland ridge with broadly similar hydrographic and transport characteristics, in reasonable agreement with the observations (see Sec. 5.2). When descending along the continental slope of the IB, the ISOW of the three models mixes with local waters that are generally moderately warmer and saltier than the observations.

Because of the step-like bottom topography, the ISOW of the GOSI9-z^*ps model experiences large spurious mixing while flowing down the IB. As a result, the GOSI9-z^*ps simulation reproduces an IB overflow that is not dense enough ($\sigma_\theta < 27.84\ kg\,m^{-3}$) to penetrate at depth and remains confined in a narrow part of the east side of the RR (Fig. 12b, f and j, Fig. 13b and f and Tab. 3).

In contrast, the smooth representation of the ocean floor typical of the GOSI9-MEs model significantly reduce the undesired numerical mixing during the dense plume descent. As a consequence, when the ISOW of the GOSI9-MEs model entrains the relatively warm and salty waters of the IB, the result is an overflow that is in good agreement with the observations for temperature but is slightly saltier and hence denser than the measurements (Fig. 12d, h and l, Fig. 13d and h and Tab. 3).

The GOSI9-szt simulation represents an intermediate solution, where numerical mixing is partially reduced in comparison to the GOSI9-z^*ps model but is still too large to retain a dense modified ISOW similar to the observations (Fig. 12c, g and k, Fig. 13c and g and Tab. 3). Interestingly, the GOSI9-szt model seems to be able to mitigate the salinity bias affecting the ISOW of the GOSI9-MEs simulation. This is probably a compensation error rather than a model improvement due to the higher numerical mixing affecting the GOSI9-szt model below the 1200 m, as indicated by Fig. 12k and l, Fig. 13g and h and Fig. 14f.

The DSOW simulated by the three models in the proximity of the Greenland-Scotland ridge presents significant positive temperature and salinity biases, that are compensated in terms of buoyancy, resulting in an overflow density very similar to the observations (Fig. 11$a.^*$, $b.^*$, $c.^*$ and $d.^*$ and Tab. 2).

In the GOSI9-z^*ps simulation, the excessive numerical diapycnal mixing seems to seriously affect the properties of the dense descending plume. As a result, a relatively light modified DSOW that does not reach the bottom of the IS is created - see the salty plume with $\sigma_\theta < 27.84\ kg\,m^{-3}$ that spreads at its neutrally buoyant level in Fig. 14j isolating the relatively fresh water mass at the bottom. Consequently, the mid depth flowing modified DSOW mixes with the relatively warm and salty modified ISOW circulating in the IS in the same depth range (see Fig. 15a). This can be observed in the peak in transport shown in Fig. 10a for densities between 27.80 $kg\,m^{-3}$ and 27.85 $kg\,m^{-3}$ and the large positive active tracers biases of Fig. 13 between $1500-2000\ m$ along the continental slope of Greenland.

In the GOSI9-MEs experiment, the cascading DSOW experiences significantly reduced numerical mixing and entrains the relatively cold and salty modified ISOW flowing in the IS at depths between $1500-2500\ m$ - see, for example, the propagation paths of the cold and salty anomalies with respect to GOSI9-z^*ps and GOSI9-szt models presented in Fig. 14b and e and Fig. 14c and f, respectively. As a result, a modified DSOW with an average σ_θ in good agreement with the observations that reaches the bottom of the IS is created, as shown in Fig. 12d and Tab. 3. Because of the hydrographic biases already affecting the DSOW upstream, improvements in temperature at the bottom of the IS in comparison to the other two models are small (Fig. 14b and c), while salinity errors are slightly more pronounced (Fig. 14e and f).

Also in the IS the GOSI9-szt solution represents a hybrid between the GOSI9-z^*ps and GOSI9-MEs simulations - see for example the temperature and salinity anomalies with respect to GOSI9-z^*ps (Fig. 14a and d) and GOSI9-MEs (Fig. 14c and f) simulations. Since numerical mixing is reduced only at depths shallower than 1200 m, the GOSI9-szt model simulates a modified DSOW with $\sigma_\theta > 27.84\ kg\, m^{-3}$, but one that is not dense enough to reach the bottom of the IS, therefore spreading laterally at its neutral buoyancy level and isolating the relatively cold and fresh water of the initial condition as in the GOSI9-z^*ps case (see Fig. 12c, g, and k).

Finally, our results show that the impact of changing the vertical coordinate system seems to extend beyond the boundaries of the localisation area, affecting also the hydrographic properties of the DWBC in the Labrador Sea and along the eastern continental slope of North America as indicated by Fig. 14.

In summary, the following main points result from our analysis:

- The three models present similar temperature and salinity biases that compensate in buoyancy;
- Biases affecting the modified ISOW seem to play an important role in pre-conditioning the overflow biases in the IS;
- The GOSI9-MEs model is able to reduce the spurious mixing and retain the dense overflow signal at depth, as expected. However, as a result tracers biases at the bottom are exacerbated in the GOSI9-MEs simulation, especially for the case of salinity;
- In the GOSI9-z^*ps and GOSI9-szt experiments the large numerical mixing combines with models biases to generate modified ISOW and DSOW water masses that are too warm and not dense enough but at the same time not as saline as the ones of the GOSI9-MEs simulation, especially at the bottom;
- The impact of using local-GVC in the Nordic Seas overflow region extends to the entire subpolar gyre.

6 Conclusions and perspectives

A simple methodology to smoothly blending between different type of quasi-Eulerian generalised vertical coordinates in the horizontal direction is introduced. We refer to it as *localisation* method, since it allows one to change the type of vertical coordinate system in arbitrarily chosen time-invariant localised areas of numerical ocean models. The result is a quasi-Eulerian coordinate system that is hybrid in the horizontal direction, similar to how some coordinates are hybrid in the vertical. One of the main aims of the *localisation* method proposed in this study is to improve the ocean models' representation of the important influence the bottom topography exerts on the oceanic flow.

After detailing the characteristics of the novel method, in this study we test its ability to improve the Nordic Seas overflows representation in a NEMO-based eddy-permitting global ocean configuration. Three state-of-the-art z^*-coordinate, with partial steps (z^*ps), models localising different types of terrain-following vertical coordinates in the proximity of the Greenland-Scotland ridge are compared against a control employing z^*ps levels everywhere. The quasi-Eulerian vertical coordinates tested in the Greenland-Scotland ridge localisation area are the vanishing quasi-sigma (vqs), the hybrid sz-transitioning (szt) or the multi-envelope s (MEs) coordinates.

Two idealised numerical experiments and a realistic 10-years long simulation are conducted. The idealised experiments aim at assessing the ability of the models to accurately compute horizontal pressure forces and reduce spurious diapycnal mixing when simulating dense water cascading down the steep continental slope of the Irminger Sea.

The realistic runs seek to evaluate the models' skill in reproducing observed hydorgraphic and transport properties of the Nordic overflows.

Numerical experiments indicate that the localisation approach proposed in this study can be successfully used to embed terrain-following levels in a global ocean configuration otherwise using quasi-Eulerian geopotential-based vertical coordinates, provided that the localised terrain-following coordinate system chosen is flexible enough to allow a smooth transition between the two (as in the MEs and szt cases, for example). In particular, the vqs approach seems to be not suitable for our localisation methodology, at least in the configuration proposed in this study (i.e., vqs embedded in z^*ps) - the same conclusion should apply to classical σ-coordinates, being a special case of vqs coordinates.

The Nordic overflow test-case shows that localising terrain-following MEs coordinates in the Greenland-Scotland ridge region allows important reduction of spurious cross-isopycnal mixing when modeling bottom intensified buoyancy driven currents, significantly improving the realism of Nordic overflows simulations in comparison to the models using z^*ps or szt coordinates, especially in term of density and transport. The impact of changing vertical grid propagates well beyond the boundaries of the Greenland-Scotland ridge localisation area, extending to the entire subpolar gyre, demonstrating the robustness and efficacy of the localisation method.

Important hydrographic biases similarly affect all the realistic experiments. In the case of models using geopotential-based levels at depth, the large numerical mixing results in a secondary compensating effect that mitigates the models' biases at the bottom, especially for salinity. To the contrary, the ability of the model using local-MEs levels to importantly reduce spurious mixing exacerbates the salinity biases at the bottom. These results indicate that the Nordic region of our eddy-permitting global configuration is affected by biases that can not be mitigated using a vertical grid targeting the local leading processes, especially in the case of salinity. Other studies have reported important salinity biases affecting NEMO-based simulations of the North Atlantic subpolar gyre (e.g., Treguier et al. (2005); Rattan et al. (2010); Marzocchi et al. (2015)). A special North Atlantic process evaluation group (NatlPEG) involving the UK Met Office and National Oceanography Centre is currently investigating possible large scale causes behind those biases.

The localisation method proposed in this paper is general, in the sense that can be easily applied to any region of any quasi-Eulerian model domain. For example, applications to improve the representation of boundary currents and the shelf dynamics in global ocean configurations are currently being tested. Similarly, the localisation method is also being implemented with promising results in a regional set-up to embed MEs coordinates in a model using vqs levels for improving the shelf dynamics.

Finally, possible future developments include using the localisation method to make it easier changing type of vertical grid in AGRIF (Debreu et al., 2008, 2012) nests or combining a local-MEs coordinate system with the Brinkman penalisation approach (Debreu et al., 2020), considering that both methods rely on the definition of envelope(s) of the bottom topography.

Appendix A A Simple algorithm for defining transition areas

Let us consider a model domain with horizontal coordinates x and y. A generic localisation area Λ can be defined by an indicator function $\mathbb{1}_\Lambda(x,y)$,

$$\mathbb{1}_\Lambda(x,y) = \begin{cases} 1 & \text{if } (x,y) \in \Lambda, \\ 0 & \text{otherwise.} \end{cases} \tag{A1}$$

Then, the generic transition area T encircling the localisation area Λ is computed in this study according to the following algorithm:

$B = J + \gamma(J - \mathbb{1}_\Lambda)$ `//` $B(x,y)$ `is 1 if` $(x,y) \in \Lambda$, $1+\gamma$ `if not;`
$W = B$;
$n = 0$;
while $n \leq n_{iter}$ **do**
    $\overline{W} = G \star W$;
    $W = \mathbb{1}_\Lambda + (J - \mathbb{1}_\Lambda) \circ \overline{W}$ `//` $W(x,y)$ `is 1 if` $(x,y) \in \Lambda$, $\overline{W}(x,y)$ `if not;`
    $n{+}{=}1$;
end
$D = |W - B|$;

where $J(x,y) = 1$, $\gamma = 1.0 \times 10^{-10}$ is a tunable coefficient, n is the iterator variable, n_{iter} is the user-defined maximum number of iterations, $G(x_0, y_0, \sigma_G, x, y)$ is a two-dimensional spatial Gaussian filter with σ_G the user-defined width of the filter and $\circ$ describing the Hadamard product (e.g., Horn & Johnson (1985)). The value of a the filtered function $\overline{W}(x,y)$ after the Gaussian low-pass filtering operation $G\star W$ at a point(x_0, y_0) is given by

$$\overline{W}(x_0,y_0) = G \star W = \iint W(x,y)\, G(x_0,y_0,\sigma_G,x,y)\, dx\, dy \tag{A2}$$

$$= \frac{1}{2\pi\sigma_G^2} \iint W(x,y)\, \exp\Big\{ -\frac{(x-x_0)+(y-y_0)}{2\sigma_G^2} \Big\}\, dx\, dy \tag{A3}$$

The transition area T is then defined by the indicator function $\mathbb{1}_T(x,y)$,

$$\mathbb{1}_T(x,y) = \begin{cases} 1 & \text{if } D(x,y) > 0 \\ 0 & \text{otherwise.} \end{cases} \tag{A4}$$

In this work, the transition area is generated using $\sigma_G = 1$ and $n_{iter} = 1$.

Appendix B Quasi-Eulerian coordinates transformations

This section describes the QE GVCs implemented in this study. While here we focus on the details of the analytical coordinate transformations, it is worth mentioning that the NEMO model implements QE GVCs defining discrete model levels with respect to an unperturbed ocean at rest (i.e., $\mathbf{u} = 0$, $\eta = 0$) and then uses the variable volume layer algorithm of Levier et al. (2007) to evolve h_k according to equation 4 with $\alpha_k \propto h_k^0 H^{-1}$.

B1 z^*-coordinate

The NEMO implementation of the z^*-coordinate transformation follows Stacey et al. (1995) and Adcroft & Campin (2004):

$$z = \eta + z^* \frac{H + \eta}{H}, \tag{B1}$$

with $z^*(z = \eta) = 0$ and $z^*(z = -H) = -H$ (see Fig. 3b and Fig. B1a).

B2 vqs-coordinate

The standard NEMO v4.0.4 implementation of vqs coordinates is used in this study (see Fig. 3c and Fig. B1b), which combines modified versions of the QE GVCs originally proposed by Dukhovskoy et al. (2009) and Song & Haidvogel (1994):

$$z = \eta\Big[1 + \frac{h_c}{H_e}\sigma + \Big(1 - \frac{h_c}{H_e}\Big)C(\sigma)\Big] + h_c\sigma + C(\sigma)(H_e - h_c), \tag{B2}$$

where $\sigma(z = \eta) = 0$ and $\sigma(z = -H_e) = -1$, $C(\sigma)$ is the Song & Haidvogel (1994) stretching function, H_e is a smooth envelope bathymetry (positive downward and such that $H_e \geq H$) and h_c is the depth at which the transition from stretched to uniform distributed levels occurs. Equation B2, differently from the original s-coordinates of Song & Haidvogel (1994), ensures that α_k of equation 4 is a function of h_k^0 and the total model depth H_e.

A similar set-up to Colombo (2018) is applied for localising vqs levels in the Nordic overflows area, using $\theta = 6.0$ and $b = 0.7$ and $h_c = 50$.

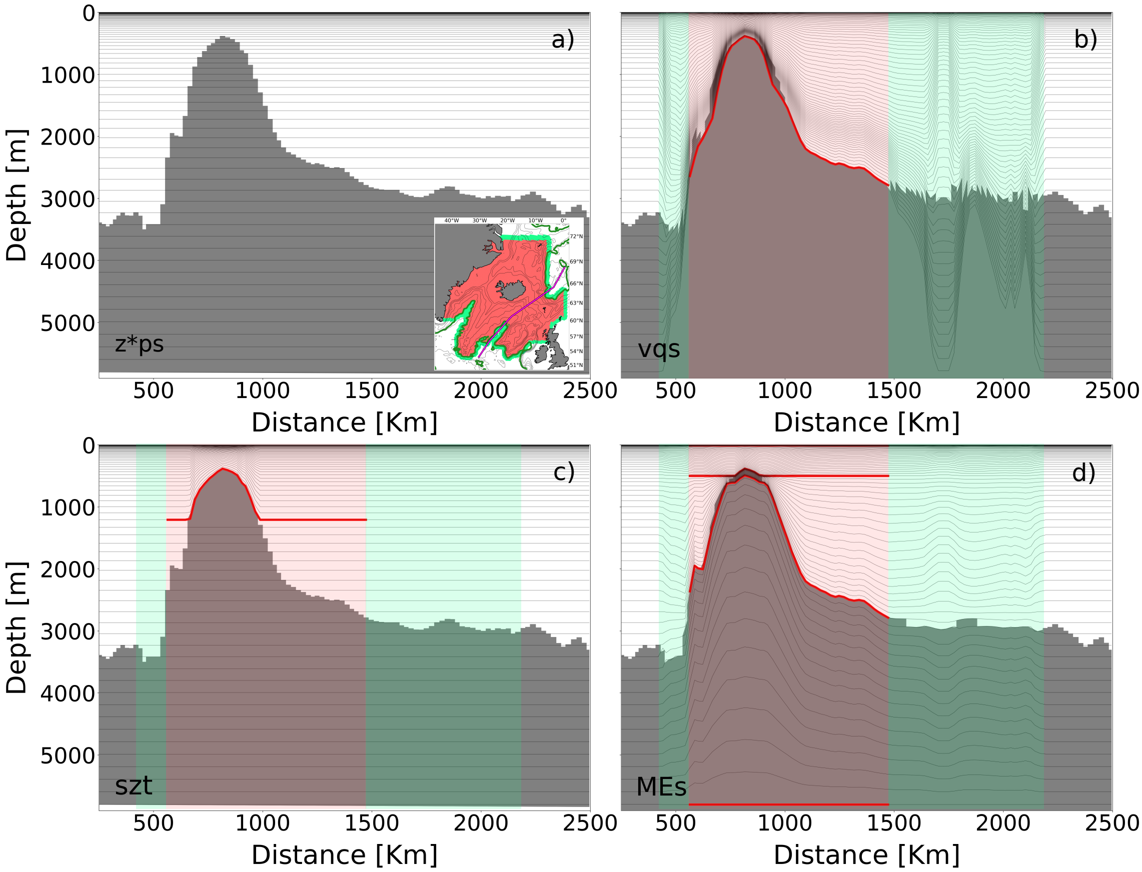

Figure B1. Panel a) shows the model bathymetry cross-section extracted from the GOSI9-z^*ps model, panel b) from the GOSI9-vqs model while panel c) and d) from the GOSI9-szt and GOSI9-MEs models, respectively. In the inset in panel a), the red and green regions represent the Nordic overflows localisation and transition areas used in this study, respectively, the blue line shows the location of the model bathymetry cross-sections presented in the other panels while the green line marks the 2800 m isobath. In panels a) to d) the red lines shows the location of the envelopes used to configure the localised GVCs.

B3 *szt*-coordinate

The szt scheme described in Wise et al. (2021) allows one to combine vqs and z^*ps QE coordinates (see Fig. 3d and Fig. B1c). The szt analytical formulation reads

$$z = \begin{cases} \eta\Big[1 + \frac{\tilde{h}_c}{H_e}\sigma + \Big(1 - \frac{\tilde{h}_c}{H_e}\Big)Z(\sigma)\Big] + \tilde{h}_c\sigma + Z(\sigma)(H_e - \tilde{h}_c) & \text{for } H \leq H_t, \\ \eta + z^* \frac{H+\eta}{H} & \text{for } H > H_t, \end{cases} \tag{B3}$$

where H_t is the depth at which the transition from vqs to $z*$ coordinates occurs, H_e is a smooth envelope bathymetry with maximum depth H_t and $\sigma(z = \eta) = 0$, $\sigma(z = -H_t) = -1$, $z^*(z = \eta) = 0$ and $z^*(z = -H) = -H$. The standard NEMO formulation for vqs-coordinates (B2) is modified by replacing $C(\sigma)$ with $Z(\sigma)$, a stretching function consistent with the one of Madec et al. (1996)), and using the variable $\tilde{h}_c$ defined as

$$\tilde{h}_c = \min\left\{\max\left\{\frac{H_e - H_t}{1 - \frac{H_t}{h_c}}, 0\right\}, h_c\right\}. \tag{B4}$$

When discretising, the smoothness of h_k is retained by ensuring that discrete vqs and z^* levels are distributed along the water column according to a consistent stretching function.

In practise, the following algorithm is used to generate a szt grid. At first, the k_t z^*-level at which the transition will occur is chosen (in the case of this paper, $k_t = 48$). Then, a standard z^*ps vertical grid is generated. After, an envelope bathymetry H_e with maximum depth $H_t = \max\{z_{k_t}\}$ is computed and used to recompute the depth of all the discrete model levels with $k < k_t$.

B4 ME*s*-coordinate

The ME method of Bruciaferri et al. (2018) defines n arbitrary depth surfaces $H_e^i(x, y, t)$ (downward positive) called *envelopes* (with $1 \leq i \leq n$) to divide the ocean model vertical domain into n sub-zones D_i, each one bounded by envelopes H_e^{i-1} at the top and H_e^i at the bottom (with $H_e^0 = -\eta$). Each envelope moves with the free surface according to

$$H_e^i = H_{e_0}^i - \eta\Big(1 - \frac{H_{e_0}^i}{H_b}\Big), \tag{B5}$$

where $H_{e_0}^i(x, y)$ is the depth with respect to an unperturbed ocean at rest and $H_b = H_{e_0}^n \geq H$.

ME s-coordinates are implemented in the Greenland-Scotland ridge local area using four envelopes and the following coordinate transformation (see Fig. 3e and Fig. B1d):

$$z\big|_{D_i} = \begin{cases} C_i(\sigma_i)(H_e^i - H_e^{i-1} - h_c^i) - H_e^{i-1} + h_c^i\sigma_i + \eta\beta_i & \text{if } i \in \{1, 3\}, \\ P_{x,y,i}^3(\sigma_i)\Big(1 + \frac{\eta}{H_b}\Big) & \text{if } i \in \{2, 4\}, \end{cases} \tag{B6}$$

where $\sigma_i(z = -H_e^{i-1}) = 0$ and $\sigma_i(z = -H_e^i) = -1$, $C_i(\sigma_i)$ is a generic stretching function applied in sub-zone D_i and h_c^i is the depth at which the transition from stretched to uniform distributed levels occurs. The term β_i, defined as

$$\beta_i = \frac{h_c^i}{H_b}\sigma_i - \frac{h_c^i}{H_b}C_i(\sigma_i),$$

ensures that α_k of equation 4 is a function of h_k^0 and the total model depth H_b. The function $P^3_{x,y,i}(\sigma_i)$ represents a complete cubic spline whose coefficients are computed ensuring the monotonicity and continuity of the Jacobian of the transformation for the case of an unperturbed ocean at rest (see Bruciaferri et al. (2018) for the details).

In this study we set $h_c^i = 0$ while the Song & Haidvogel (1994) stretching functions $C_1(\sigma_1)$ and $C_3(\sigma_3)$ use $\theta_1 = 1.2$, $b_1 = 0.7$ and $\theta_3 = 2.4$, $b_3 = 0.85$, respectively. The first envelope $H^1_{e_0}$ has depth equal to 10 m, so that the upper sub-zone D_1 can be discretised with a constant high resolution consistent with the global z^*ps grid. Envelope $H^2_{e_0}$ follows a smoothed version of the bottom topography H from a minimum depth of 40 m to a maximum depth of 500 m: in this way, sub-zone D_2 can use nearly terrain-following levels where $40\ m \leq H \leq 500\ m$ to better resolve shelf cascading, while elsewhere can employ z^*-like interfaces to minimise HPG errors; Similarly, the envelope $H^3_{e_0}$ follows the smoothed model bathymetry in areas where $610\ m \leq H \leq 2800\ m$, resulting in terrain-following levels only in areas where the bottom topography is in this depth range to improve overflows simulations. The bottom geopotential envelope $H^4_{e_0}$ targets the depth of last W-level of the global z^*ps grid, so that model levels near the bottom can smoothly transition from the local to the global grid. Envelopes $H^2_{e_0}$ and $H^3_{e_0}$ are smoothed using the iterative algorithm described in Appendix C.

Once the envelopes have been identified based on physical motivations, local ME s-coordinates are discretised assigning to each layers D_i a number of levels which is largely dictated by the number of levels possessed by the global z^*ps grid at a similar depth range. For example, in this study 9 levels are used in layer D_1, 31 in D_2, 20 in D_3 and 15 in D_4.

Appendix C Iterative algorithm for smoothing envelopes surfaces

The iterative algorithm applied in this study to smooth the envelopes of vqs, szt and MEs models relies on the Martinho & Batteen (2006) smoothing procedure to ensure that the local slope parameter r (see Sec. 3.2 for its definition) is smaller than a user defined threshold r_{max}.

Figure C1 summarises the main steps of our iterative algorithm. At first, the envelopes of the three GVCs were smoothed by applying the Martinho & Batteen (2006) method with an $r_{max} = 0.12$. After, for each of the GVCs, a series of idealised HPG tests with a set-up similar to the one described in Sec. 4.1 were run: at each iteration, the envelopes were smoothed with an increasingly more severe r_{max} only in those grid points where HPG errors exceeded 0.05 $m\ s^{-1}$ (see text of steps 4, 5 and 6 of Fig. C1 for the details). This value was chosen following Wise et al. (2021), that showed that optimising the envelopes of a ME system to have HPG error $<\ 0.05\ m\ s^{-1}$ can significantly improve the accuracy of a terrain-following shelf model of the North West European shelf with a lateral resolution of 7 km. In this work, three iterations of the iterative smoothing algorithm were applied to generate the envelopes used to implement the localised GVCs described in Sec. 3.2.

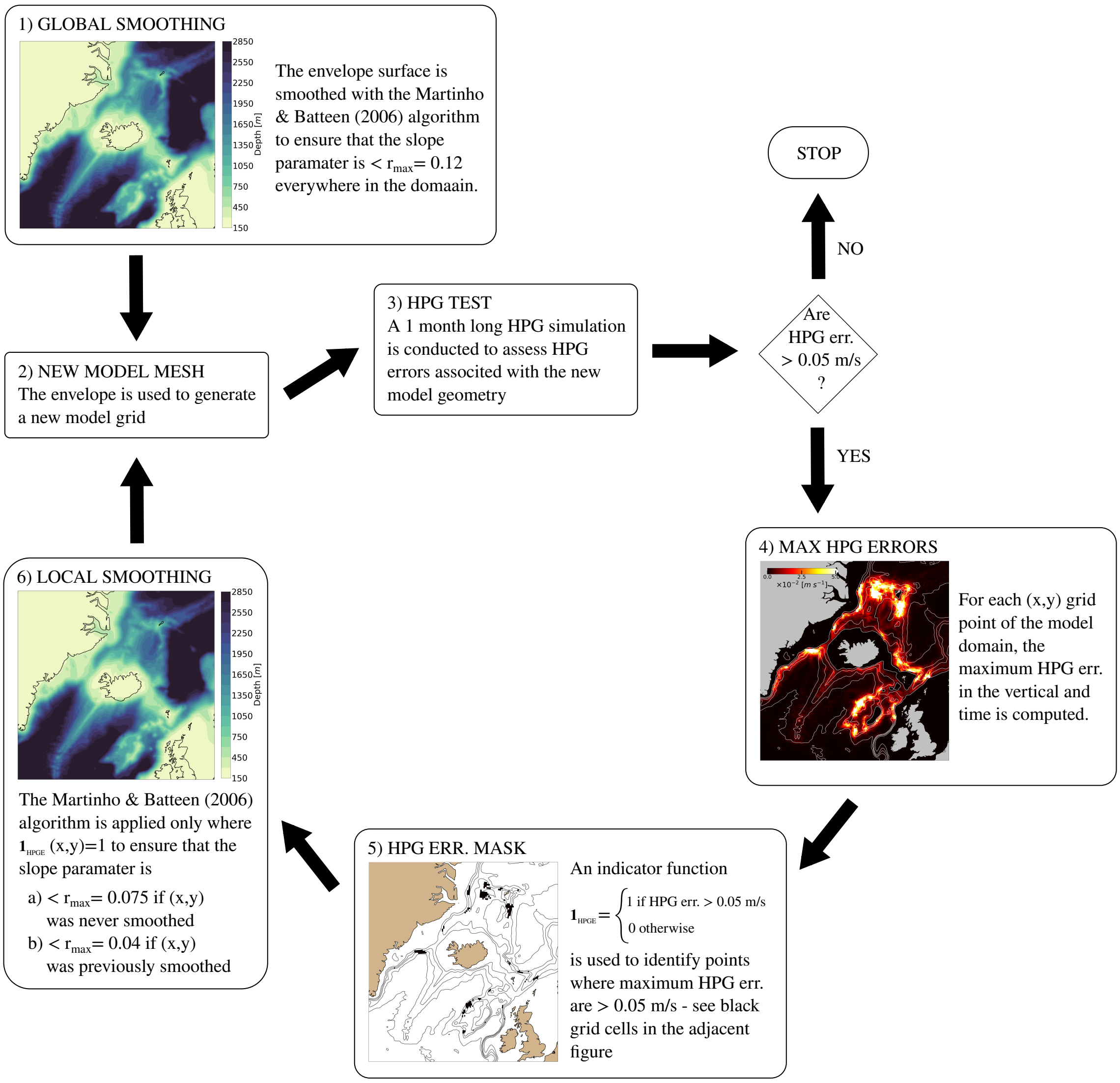

Figure C1. Main steps of the iterative smoothing algorithm applied in this study to smooth the envelopes of vqs, szt and MEs models.

Appendix D List of acronyms

Table D1 is a list of acronyms to assist cross-referencing abbreviations used in the paper.

Acronym	Meaning
Vertical Coordinates	
GVC	Generalised vertical coordinate
QE	quasi-Eulerian
QL	quasi-Lagrangian
ALE	Arbitrary Lagrangian Eulerian
z^*ps	z^*-coordinates with partial steps
vqs	Vanishing quasi-sigma
szt	Hybrid sz-transitioning
MEs	Multi-Envelope s-coordinates
Water masses and currents	
AMOC	Atlantic Meridional Overturning Circulation
DSOW	Denmark Strait Overflow Water
ISOW	Iceland-Scotland Overflow Water
NAW	North Atlantic Water
DWBC	Deep Western Boundary Current
Numerical models	
GOSI9-025	GOSI9 global ocean configuration at 1/4° of horizontal resolution
GOSI9-z^*ps	standard GOSI9-025 configuration using z^*ps everywhere
GOSI9-vqs	GOSI9-025 configuration using vqs levels in the Greenland-Scotland ridge area
GOSI9-szt	GOSI9-025 configuration using szt levels in the Greenland-Scotland ridge area
GOSI9-MEs	GOSI9-025 configuration using MEs levels in the Greenland-Scotland ridge area
Observational datasets	
OSNAP	Overturning in the Subpolar North Atlantic Program
WOA18	World Ocean Atlas 2018
DS	Denmark Strait cross-section
IS	Irminger sea portion of the eastern leg of the OSNAP cross-section
IB	Icelandic basin portion of the eastern leg of the OSNAP cross-section
IFR	Iceland-Faroe ridge cross-section
FSC	Faroe-Shetland channel cross-section
FBC	Faroe-Bank channel cross-section
WTR	Wyville-Thomson ridge cross-section
CFGZ	Charlie-Gibbs Fracture Zone cross-section
Miscellaneous	
NEMO	Nucleus for European Modelling of the Ocean
HPG	Horizontal pressure gradient

Table D1. List of acronyms used in the paper.

Appendix E Open Research

The four models compared in this study are based on the NEMO ocean model code, which is freely available from the NEMO website (`https://www.nemo-ocean.eu`, last access: 19 June 2023). The code to localise quasi-Eulerian general vertical coordinates used in this study is included in the NEMO v4.2 trunk. Additional modifications to the NEMO original code are required for running GOSI9-based configurations. The actual NEMO v4.0.4 source code and the namelists used to run the integrations presented in this manuscript are available at `https://zenodo.org/record/8056285` and `https://zenodo.org/record/8055445`.

The data that comprise the GOSI9-z^*ps, GOSI9-vqs, GOSI9-szt and GOSI9-MEs simulations are of the order of tens of TB. However, the data can be made available by contacting the authors.

The data describing the geometry of the four models and the derived output data used for the analyses and plots included in this manuscript are available at `https://zenodo.org/record/8055023` while the actual code to reproduce the analysis and the plots can be found at `https://github.com/JMMP-Group/loc_gvc-GO_ovf` and `https://github.com/JMMP-Group/nordic-seas-validation`.

Acknowledgments

Funding support for DB, CG and HH was provided by the Joint DECC/Defra Met Office Hadley Centre Climate Programme (GA01101), UK Ministry of Defense and the UK Public Weather Service. JH and MA were supported by the H2020 European Institute of Innovation and Technology (IMMERSE) grant no. 821926. The authors would like to thank Mike Bell, Dave Storkey, Nigel Wood and Jérome Chanut for helpful and constructive discussions, suggestions and advice. Numerical simulations and analysis were carried out on the Cray HPC at the Met Office, UK.

References

Adcroft, A., Anderson, W., Balaji, V., Blanton, C., Bushuk, M., Dufour, C. O., ... Zhang, R. (2019, oct). The GFDL Global Ocean and Sea Ice Model OM4.0: Model Description and Simulation Features. *Journal of Advances in Modeling Earth Systems*, *11*(10), 3167–3211. Retrieved from `https://onlinelibrary.wiley.com/doi/10.1029/2019MS001726` doi: 10.1029/2019MS001726

Adcroft, A., & Campin, J.-M. (2004, jan). Rescaled height coordinates for accurate representation of free-surface flows in ocean circulation models. *Ocean Modelling*, *7*(3-4), 269–284. Retrieved from `http://linkinghub.elsevier.com/retrieve/pii/S1463500303000544` doi: 10.1016/j.ocemod.2003.09.003

Adcroft, A., & Hallberg, R. (2006, jan). On methods for solving the oceanic equations of motion in generalized vertical coordinates. *Ocean Modelling*, *11*(1-2), 224–233. Retrieved from `https://linkinghub.elsevier.com/retrieve/pii/S1463500305000090` doi: 10.1016/j.ocemod.2004.12.007

Beckers, J. M., Gregoire, M., Nihoul, J. C. J., Stanev, E., Staneva, J., & Lancelot, C. (2002). Modelling the Danube-influenced North-western Continental Shelf of the Black Sea. I: Hydrodynamical Processes Simulated by 3-D and Box Models. *Estuarine, Coastal and Shelf Science*, *54*(3), 453–472. Retrieved from `http://www.sciencedirect.com/science/article/pii/S0272771400906589` doi: 10.1006/ecss.2000.0658

Bleck, R. (1978, sep). On the Use of Hybrid Vertical Coordinates in Numerical Weather Prediction Models. *Monthly Weather Review*, *106*(9), 1233–1244. Retrieved from `http://journals.ametsoc.org/doi/10.1175/1520-0493(1978)106%3C1233:OTUOHV%3E2.0.CO;2` doi: 10.1175/1520-0493(1978)106⟨1233:OTUOHV⟩2.0.CO;2

Bleck, R. (2002, jan). An oceanic general circulation model framed in hybrid isopycnic-Cartesian coordinates. *Ocean Modelling*, *4*(1), 55–88. Retrieved from `http://www.sciencedirect.com/science/article/pii/S1463500301000129https://linkinghub.elsevier.com/retrieve/pii/S1463500301000129` doi: 10.1016/S1463-5003(01)00012-9

Boyer, T. P., Garcia, H. E., Locarnini, R. A., Zweng, M. M., Mishonov, A. V., Reagan, J. R., ... Smolyar, I. V. (2018). *World Ocean Atlas 2018* (Tech. Rep.). NOAA National Centers for Environmental Information. Dataset. Retrieved from `https://www.ncei.noaa.gov/archive/accession/NCEI-WOA18`

Bruciaferri, D., Shapiro, G., Stanichny, S., Zatsepin, A., Ezer, T., Wobus, F., ... Hilton, D. (2020, feb). The development of a 3D computational mesh to improve the representation of dynamic processes: The Black Sea test case. *Ocean Modelling*, *146*, 101534. Retrieved from `https://linkinghub.elsevier.com/retrieve/pii/S1463500319301593` doi: 10.1016/j.ocemod.2019.101534

Bruciaferri, D., Shapiro, G. I., & Wobus, F. (2018, oct). A multi-envelope vertical coordinate system for numerical ocean modelling. *Ocean Dynamics*, *68*(10), 1239–1258. Retrieved from `http://link.springer.com/10.1007/s10236-018-1189-x` doi: 10.1007/s10236-018-1189-x

Bruciaferri, D., Tonani, M., Ascione, I., Al Senafi, F., O'Dea, E., Hewitt, H. T., &

Saulter, A. (2022, dec). GULF18, a high-resolution NEMO-based tidal ocean model of the Arabian/Persian Gulf. *Geoscientific Model Development*, *15*(23), 8705–8730. Retrieved from https://gmd.copernicus.org/articles/15/8705/2022/ doi: 10.5194/gmd-15-8705-2022

Burchard, H., Petersen, O., & Petersen, O. (1997, nov). Hybridization between σ- and z-co-ordinates for improving the internal pressure gradient calculation in marine models with steep bottom slopes. *International Journal for Numerical Methods in Fluids*, *25*(9), 1003–1023. Retrieved from https://onlinelibrary.wiley.com/doi/10.1002/(SICI)1097-0363(19971115)25:9%3C1003::AID-FLD600%3E3.0.CO;2-E doi: 10.1002/(SICI)1097-0363(19971115)25:9⟨1003::AID-FLD600⟩3.0.CO;2-E

Colombo, P. (2018). *Modelling dense water flows through sills in large scale realistic ocean models: demonstrating the potential of a hybrid geopotential/terrain-following vertical coordinate* (Doctoral dissertation, Université Grenoble Alpes). Retrieved from http://www.theses.fr/2018GREAU017

Colombo, P., Barnier, B., Penduff, T., Chanut, J., Deshayes, J., Molines, J.-M., … Treguier, A.-M. (2020, jul). Representation of the Denmark Strait overflow in a z-coordinate eddying configuration of the NEMO (v3.6) ocean model: resolution and parameter impacts. *Geoscientific Model Development*, *13*(7), 3347–3371. Retrieved from https://gmd.copernicus.org/articles/13/3347/2020/ doi: 10.5194/gmd-13-3347-2020

Debreu, L., Kevlahan, N.-R., & Marchesiello, P. (2020, jan). Brinkman volume penalization for bathymetry in three-dimensional ocean models. *Ocean Modelling*, *145*, 101530. Retrieved from https://linkinghub.elsevier.com/retrieve/pii/S146350031930174X doi: 10.1016/j.ocemod.2019.101530

Debreu, L., Marchesiello, P., Penven, P., & Cambon, G. (2012, jun). Two-way nesting in split-explicit ocean models: Algorithms, implementation and validation. *Ocean Modelling*, *49-50*, 1–21. Retrieved from https://linkinghub.elsevier.com/retrieve/pii/S1463500312000480 doi: 10.1016/j.ocemod.2012.03.003

Debreu, L., Vouland, C., & Blayo, E. (2008, jan). AGRIF: Adaptive grid refinement in Fortran. *Computers & Geosciences*, *34*(1), 8–13. Retrieved from https://linkinghub.elsevier.com/retrieve/pii/S009830040700115Xhttp://linkinghub.elsevier.com/retrieve/pii/S009830040700115X doi: 10.1016/j.cageo.2007.01.009

Dickson, R. R., & Brown, J. (1994). The production of North Atlantic Deep Water: Sources, rates, and pathways. *Journal of Geophysical Research*, *99*(C6), 12319. Retrieved from http://doi.wiley.com/10.1029/94JC00530 doi: 10.1029/94JC00530

Dickson, R. R., Meincke, J., & Rhines, P. (Eds.). (2008). *ArcticSubarctic Ocean Fluxes*. Dordrecht: Springer Netherlands. Retrieved from http://link.springer.com/10.1007/978-1-4020-6774-7 doi: 10.1007/978-1-4020-6774-7

Dukhovskoy, D. S., Morey, S. L., Martin, P. J., O'Brien, J. J., & Cooper, C. (2009). Application of a vanishing, quasi-sigma, vertical coordinate for simulation of high-speed, deep currents over the Sigsbee Escarpment in the Gulf of Mexico. *Ocean Modelling*, *28*(4), 250–265. Retrieved from http://dx.doi.org/10.1016/j.ocemod.2009.02.009 doi: 10.1016/j.ocemod.2009.02.009

Ezer, T. (2005, jan). Entrainment, diapycnal mixing and transport in three-dimensional bottom gravity current simulations using the MellorYamada turbulence scheme. *Ocean Modelling*, *9*(2), 151–168. Retrieved from http://linkinghub.elsevier.com/retrieve/pii/S1463500304000368 doi: 10.1016/j.ocemod.2004.06.001

Ezer, T. (2006). Topographic influence on overflow dynamics: Idealized numerical simulations and the Faroe Bank Channel overflow. *Journal of Geophysical Research*, *111*(C2), C02002. Retrieved from http://doi.wiley.com/10.1029/

2005JC003195 doi: 10.1029/2005JC003195
Ezer, T. (2016, aug). Revisiting the problem of the Gulf Stream separation: on the representation of topography in ocean models with different types of vertical grids. *Ocean Modelling*, *104*, 15–27. Retrieved from http://linkinghub.elsevier.com/retrieve/pii/S1463500316300397 doi: 10.1016/j.ocemod.2016.05.008
Ezer, T., Arango, H., & Shchepetkin, A. F. (2002). Developments in terrain-following ocean models: Intercomparisons of numerical aspects. *Ocean Modelling*, *4*(3-4), 249–267. doi: 10.1016/S1463-5003(02)00003-3
Ezer, T., & Mellor, G. L. (2004, jan). A generalized coordinate ocean model and a comparison of the bottom boundary layer dynamics in terrain-following and in z-level grids. *Ocean Modelling*, *6*(3-4), 379–403. Retrieved from https://linkinghub.elsevier.com/retrieve/pii/S146350030300026X doi: 10.1016/S1463-5003(03)00026-X
Gibson, A. (2019). *An adaptive vertical coordinate for idealised and global ocean modelling* (Doctoral dissertation, The Australian National University). doi: 10.25911/5f58b0768dafb
Good, S. A., Martin, M. J., & Rayner, N. A. (2013, dec). EN4: Quality controlled ocean temperature and salinity profiles and monthly objective analyses with uncertainty estimates. *Journal of Geophysical Research: Oceans*, *118*(12), 6704–6716. Retrieved from http://doi.wiley.com/10.1002/2013JC009067 doi: 10.1002/2013JC009067
Griffies, S. M. (2004). *Fundamentals of Ocean Climate Models.* Princeton, NJ: Princeton University Press.
Griffies, S. M. (2012). *Elements of the modular ocean model (MOM): 2012 release (GFDL Ocean Group Technical Report No. 7)* (Tech. Rep.). Princeton, USA: NOAA/Geophysical Fluid Dynamics Laboratory.
Griffies, S. M., Adcroft, A., & Hallberg, R. W. (2020, oct). A Primer on the Vertical LagrangianRemap Method in Ocean Models Based on Finite Volume Generalized Vertical Coordinates. *Journal of Advances in Modeling Earth Systems*, *12*(10). Retrieved from https://onlinelibrary.wiley.com/doi/10.1029/2019MS001954 doi: 10.1029/2019MS001954
Griffies, S. M., Böning, C., Bryan, F. O., Chassignet, E. P., Gerdes, R., Hasumi, H., … Webb, D. (2000). Developments in ocean climate modelling. *Journal of Computational Physics*, *2*(3-4), 123–192. doi: 10.1016/S1463-5003(00)00014-7
Griffies, S. M., Gnanadesikan, A., Pacanowski, R. C., Larichev, V. D., Dukowicz, J. K., & Smith, R. D. (1998). Isoneutral Diffusion in a z-Coordinate Ocean Model. *Journal of Physical Oceanography*, *28*(5), 805–830. doi: 10.1175/1520-0485(1998)028⟨0805:IDIAZC⟩2.0.CO;2
Griffies, S. M., Pacanowski, R. C., & Hallberg, R. W. (2000, mar). Spurious Diapycnal Mixing Associated with Advection in a z -Coordinate Ocean Model. *Monthly Weather Review*, *128*(3), 538–564. doi: 10.1175/1520-0493(2000)128⟨0538:SDMAWA⟩2.0.CO;2
Guiavarc'h, C., Storkey, D., Blaker, A., Blockley, E., Megann, A., Hewitt, H., … Ann, B. (2023). GOSI9: UK Global Ocean and Sea Ice configurations. *to be submitted to Geoscientific Model Development*.
Guo, C., Ilicak, M., Bentsen, M., & Fer, I. (2016, aug). Characteristics of the Nordic Seas overflows in a set of Norwegian Earth System Model experiments. *Ocean Modelling*, *104*, 112–128. Retrieved from https://linkinghub.elsevier.com/retrieve/pii/S1463500316300543 doi: 10.1016/j.ocemod.2016.06.004
Haidvogel, D., & Beckmann, A. (1999). *Numerical Ocean Circulation Modeling.* Imperial College Press. doi: 10.2277/0521781825
Haney, R. L. (1991). On the pressure gradient force over steep topography in sigma coordinate ocean models. *Journal of Physical Oceanography*, *21*, 610–619.
Hansen, B., Larsen, K. M. H., Olsen, S. M., Quadfasel, D., Jochumsen, K., &

Østerhus, S. (2018, aug). Overflow of cold water across the IcelandFaroe Ridge through the Western Valley. *Ocean Science*, *14*(4), 871–885. Retrieved from `https://os.copernicus.org/articles/14/871/2018/` doi: 10.5194/os-14-871-2018

Hansen, B., & Østerhus, S. (2000, feb). North AtlanticNordic Seas exchanges. *Progress in Oceanography*, *45*(2), 109–208. Retrieved from `https://linkinghub.elsevier.com/retrieve/pii/S007966119900052X` doi: 10.1016/S0079-6611(99)00052-X

Harada, Y., Kamahori, H., Kobayashi, C., Endo, H., Kobayashi, S., Ota, Y., ... Takahashi, K. (2016). The JRA-55 Reanalysis: Representation of Atmospheric Circulation and Climate Variability. *Journal of the Meteorological Society of Japan. Ser. II*, *94*(3), 269–302. Retrieved from `https://www.jstage.jst.go.jp/article/jmsj/94/3/94_2016-015/_article` doi: 10.2151/jmsj.2016-015

Hirt, C., Amsden, A., & Cook, J. (1974). An arbitrary LagrangianEulerian computing method for all flow speeds. *Journal of Computational Physics*, *14*(3), 227–253.

Hofmeister, R., Burchard, H., & Beckers, J. M. (2010). Non-uniform adaptive vertical grids for 3D numerical ocean models. *Ocean Modelling*, *33*(1-2), 70–86. Retrieved from `http://dx.doi.org/10.1016/j.ocemod.2009.12.003` doi: 10.1016/j.ocemod.2009.12.003

Holliday, N. P., Cunningham, S. A., Johnson, C., Gary, S. F., Griffiths, C., Read, J. F., & Sherwin, T. (2015, sep). Multidecadal variability of potential temperature, salinity, and transport in the eastern subpolar North Atlantic. *Journal of Geophysical Research: Oceans*, *120*(9), 5945–5967. Retrieved from `https://onlinelibrary.wiley.com/doi/abs/10.1002/2015JC010762` doi: 10.1002/2015JC010762

Hopkins, J. E., Holliday, N. P., Rayner, D., Houpert, L., Le Bras, I., Straneo, F., ... Bacon, S. (2019, may). Transport Variability of the Irminger Sea Deep Western Boundary Current From a Mooring Array. *Journal of Geophysical Research: Oceans*, *124*(5), 3246–3278. Retrieved from `https://onlinelibrary.wiley.com/doi/abs/10.1029/2018JC014730` doi: 10.1029/2018JC014730

Horn, R. A., & Johnson, C. R. (1985). *Matrix Analysis*. Cambridge University Press. Retrieved from `https://www.cambridge.org/core/product/identifier/9780511810817/type/book` doi: 10.1017/CBO9780511810817

Hughes, S., Turrell, W., Hansen, B., & Østerhus, S. (2006). Fluxes of Atlantic Water (volume, heat and salt) through the Faroe Shetland Channel calculated using a decade of acoustic Doppler current profiler data (1994–2005). Collaborative Rep. 01/06. *Fisheries Research Services, Marine Laboratory*, *77*.

Ilcak, M., Adcroft, A. J., Griffies, S. M., & Hallberg, R. W. (2012, jan). Spurious dianeutral mixing and the role of momentum closure. *Ocean Modelling*, *45-46*, 37–58. Retrieved from `https://linkinghub.elsevier.com/retrieve/pii/S1463500311001685` doi: 10.1016/j.ocemod.2011.10.003

Johns, W. E., Devana, M., Houk, A., & Zou, S. (2021, aug). Moored Observations of the IcelandScotland Overflow Plume Along the Eastern Flank of the Reykjanes Ridge. *Journal of Geophysical Research: Oceans*, *126*(8). Retrieved from `https://onlinelibrary.wiley.com/doi/10.1029/2021JC017524` doi: 10.1029/2021JC017524

Johnson, H. L., Cessi, P., Marshall, D. P., Schloesser, F., & Spall, M. A. (2019, aug). Recent Contributions of Theory to Our Understanding of the Atlantic Meridional Overturning Circulation. *Journal of Geophysical Research: Oceans*, *124*(8), 5376–5399. Retrieved from `https://onlinelibrary.wiley.com/doi/10.1029/2019JC015330` doi: 10.1029/2019JC015330

Kasahara, A. (1974, jul). Various Vertical Coordinate Systems Used for Numerical Weather Prediction. *Monthly Weather Review*, *102*(7), 509–522. doi: 10.1175/

1520-0493(1974)102⟨0509:VVCSUF⟩2.0.CO;2

Käse, R. H. (2003). Structure and variability of the Denmark Strait Overflow: Model and observations. *Journal of Geophysical Research*, *108*(C6), 3181. Retrieved from `http://doi.wiley.com/10.1029/2002JC001548` doi: 10.1029/2002JC001548

Kieke, D., & Rhein, M. (2006, mar). Variability of the Overflow Water Transport in the Western Subpolar North Atlantic, 195097. *Journal of Physical Oceanography*, *36*(3), 435–456. Retrieved from `http://journals.ametsoc.org/doi/10.1175/JPO2847.1` doi: 10.1175/JPO2847.1

Kobayashi, S., Ota, Y., Harada, Y., Ebita, A., Moriya, M., Onoda, H., ... Takahashi, K. (2015). The JRA-55 Reanalysis: General Specifications and Basic Characteristics. *Journal of the Meteorological Society of Japan. Ser. II*, *93*(1), 5–48. Retrieved from `https://www.jstage.jst.go.jp/article/jmsj/93/1/93_2015-001/_article` doi: 10.2151/jmsj.2015-001

Laanaia, N., Wirth, A., Molines, J. M., Barnier, B., & Verron, J. (2010, jun). On the numerical resolution of the bottom layer in simulations of oceanic gravity currents. *Ocean Science*, *6*(2), 563–572. Retrieved from `http://www.ocean-sci.net/6/563/2010/` doi: 10.5194/os-6-563-2010

Large, W. G., & Yeager, S. G. (2009, aug). The global climatology of an interannually varying airsea flux data set. *Climate Dynamics*, *33*(2-3), 341–364. Retrieved from `http://link.springer.com/10.1007/s00382-008-0441-3` doi: 10.1007/s00382-008-0441-3

Leclair, M., & Madec, G. (2011). z-Coordinate, an Arbitrary Lagrangian-Eulerian coordinate separating high and low frequency motions. *Ocean Modelling*, *37*(3-4), 139–152. Retrieved from `http://linkinghub.elsevier.com/retrieve/pii/S1463500311000126` doi: 10.1016/j.ocemod.2011.02.001

Legg, S., Briegleb, B., Chang, Y., Chassignet, E. P., Danabasoglu, G., Ezer, T., ... Yang, J. (2009, may). Improving Oceanic Overflow Representation in Climate Models: The Gravity Current Entrainment Climate Process Team. *Bulletin of the American Meteorological Society*, *90*(5), 657–670. Retrieved from `http://journals.ametsoc.org/doi/10.1175/2008BAMS2667.1` doi: 10.1175/2008BAMS2667.1

Legg, S., Hallberg, R. W., & Girton, J. B. (2006, jan). Comparison of entrainment in overflows simulated by z-coordinate, isopycnal and non-hydrostatic models. *Ocean Modelling*, *11*(1-2), 69–97. Retrieved from `http://linkinghub.elsevier.com/retrieve/pii/S1463500304001064` doi: 10.1016/j.ocemod.2004.11.006

Lemarié, F., Kurian, J., Shchepetkin, A. F., Jeroen Molemaker, M., Colas, F., & McWilliams, J. C. (2012, jan). Are there inescapable issues prohibiting the use of terrain-following coordinates in climate models? *Ocean Modelling*, *42*, 57–79. doi: 10.1016/j.ocemod.2011.11.007

Levier, B., Treguier, A. M., Madec, G., & Garnier, V. (2007). *Free surface and variable volume in the NEMO code* (Tech. Rep.). Brest, France, MESRSEA IP report WP09-CNRS-STR03-1: IFREMER.

Li, F., Lozier, M. S., Bacon, S., Bower, A., Cunningham, S., de Jong, M., ... Zhou, C. (2023). *Temperature, Salinity and Velocity Data Derived from the OSNAP Array between August 2014 and May 2018* (Tech. Rep.). Georgia Institute of Technology. School of Earth and Atmospheric Sciences. doi: https://doi.org/10.35090/gatech/70328

Lozier, M. S., Bacon, S., Bower, A. S., Cunningham, S. A., Femke de Jong, M., de Steur, L., ... Zika, J. D. (2017, apr). Overturning in the Subpolar North Atlantic Program: A New International Ocean Observing System. *Bulletin of the American Meteorological Society*, *98*(4), 737–752. Retrieved from `https://journals.ametsoc.org/doi/10.1175/BAMS-D-16-0057.1` doi: 10.1175/BAMS-D-16-0057.1

Lozier, M. S., Li, F., Bacon, S., Bahr, F., Bower, A. S., Cunningham, S. A., … Zhao, J. (2019, feb). A sea change in our view of overturning in the subpolar North Atlantic. *Science*, *363*(6426), 516–521. Retrieved from https://www.science.org/doi/10.1126/science.aau6592 doi: 10.1126/science.aau6592

Lozier, S. M., Bower, A. S., Furey, H. H., Drouin, K. L., Xu, X., & Zou, S. (2022, nov). Overflow water pathways in the North Atlantic. *Progress in Oceanography*, *208*, 102874. Retrieved from https://linkinghub.elsevier.com/retrieve/pii/S0079661122001331 doi: 10.1016/j.pocean.2022.102874

Madec, G., Delecluse, P., Crépon, M., & Lott, F. (1996, aug). Large-Scale Preconditioning of Deep-Water Formation in the Northwestern Mediterranean Sea. *Journal of Physical Oceanography*, *26*(8), 1393–1408. doi: 10.1175/1520-0485(1996)026⟨1393:LSPODW⟩2.0.CO;2

Madec, G., & NEMO-team. (2019). NEMO ocean engine. *Scientific Notes of Climate Modelling Center, Institut Pierre-Simon Laplace (IPSL)*(27). doi: 10.5281/zenodo.1464816

Martinho, A. S., & Batteen, M. L. (2006). On reducing the slope parameter in terrain-following numerical ocean models. *Ocean Modelling*, *13*(2), 166–175. doi: 10.1016/j.ocemod.2006.01.003

Marzocchi, A., Hirschi, J. J.-M., Holliday, N. P., Cunningham, S. A., Blaker, A. T., & Coward, A. C. (2015, feb). The North Atlantic subpolar circulation in an eddy-resolving global ocean model. *Journal of Marine Systems*, *142*, 126–143. Retrieved from https://linkinghub.elsevier.com/retrieve/pii/S0924796314002437 doi: 10.1016/j.jmarsys.2014.10.007

Mastropole, D., Pickart, R. S., Valdimarsson, H., Våge, K., Jochumsen, K., & Girton, J. (2017, jan). On the hydrography of Denmark Strait. *Journal of Geophysical Research: Oceans*, *122*(1), 306–321. Retrieved from http://doi.wiley.com/10.1002/2016JC012007 doi: 10.1002/2016JC012007

Megann, A., Chanut, J., & Storkey, D. (2022, nov). Assessment of the z Time-Filtered Arbitrary LagrangianEulerian Coordinate in a Global EddyPermitting Ocean Model. *Journal of Advances in Modeling Earth Systems*, *14*(11). Retrieved from https://agupubs.onlinelibrary.wiley.com/doi/10.1029/2022MS003056 doi: 10.1029/2022MS003056

Megann, A., New, A. L., Blaker, A. T., & Sinha, B. (2010, oct). The Sensitivity of a Coupled Climate Model to Its Ocean Component. *Journal of Climate*, *23*(19), 5126–5150. Retrieved from http://journals.ametsoc.org/doi/10.1175/2010JCLI3394.1 doi: 10.1175/2010JCLI3394.1

Mellor, G. L., Ezer, T., & Oey, L.-Y. (1994). The Pressure Gradient Conundrum of Sigma Coordinate Ocean Models. *Journal of Atmospheric and Oceanic Technology*, *11*(4), 1126–1134. Retrieved from http://journals.ametsoc.org/doi/pdf/10.1175/2517.1%5Cnhttp://journals.ametsoc.org/doi/abs/10.1175/1520-0426%281994%29011%3C1126%3ATPGCOS%3E2.0.CO%3B2%5Cnhttp://dx.doi.org/10.1175/1520-0426(1994)011%3C1126:TPGCOS%3E2.0.CO doi: 10.1175/1520-0426(1994)011⟨1126:TPGCOS⟩2.0.CO;2

Mellor, G. L., Oey, L. Y., & Ezer, T. (1998). Sigma coordinate pressure gradient errors and the seamount Problem. *Journal of Atmospheric and Oceanic Technology*, *15*(5), 1122–1131. doi: 10.1175/1520-0426(1998)015⟨1122:SCPGEA⟩2.0.CO;2

O'Dea, E. J., Arnold, A. K., Edwards, K. P., Furner, R., Hyder, P., Martin, M. J., … Liu, H. (2012). An operational ocean forecast system incorporating NEMO and SST data assimilation for the tidally driven European North-West shelf. *Journal of Operational Oceanography*, *5*(1), 3–17. doi: 10.1080/1755876X.2012.1102012

Østerhus, S., Woodgate, R., Valdimarsson, H., Turrell, B., de Steur, L., Quadfasel, D., … Berx, B. (2019, apr). Arctic Mediterranean exchanges: a consistent volume budget and trends in transports from two decades of observations. *Ocean Science*, *15*(2), 379–399. Retrieved from https://os.copernicus.org/articles/15/379/2019/ doi: 10.5194/os-15-379-2019

Pacanowski, R. C., Gnanadesikan, A., & Olume, V. (1998). Transient Response in a Z -Level Ocean Model That Resolves Topography with Partial Cells. *Monthly Weather Review*, *126*(12), 3248–3270. doi: 10.1175/1520-0493(1998)126⟨3248:TRIAZL⟩2.0.CO;2

Penduff, T., Le Sommer, J., Barnier, B., Treguier, A.-M., Molines, J.-M., & Madec, G. (2007, dec). Influence of numerical schemes on current-topography interactions in 1/4 global ocean simulations. *Ocean Science*, *3*(4), 509–524. Retrieved from https://os.copernicus.org/articles/3/509/2007/ doi: 10.5194/os-3-509-2007

Petersen, M. R., Jacobsen, D. W., Ringler, T. D., Hecht, M. W., & Maltrud, M. E. (2015, feb). Evaluation of the arbitrary LagrangianEulerian vertical coordinate method in the MPAS-Ocean model. *Ocean Modelling*, *86*, 93–113. Retrieved from https://linkinghub.elsevier.com/retrieve/pii/S1463500314001796 doi: 10.1016/j.ocemod.2014.12.004

Phillips, N. A. (1957, apr). A coordinate system having some special advantages for numerical forecasting. *Journal of Meteorology*, *14*(2), 184–185. Retrieved from http://journals.ametsoc.org/doi/10.1175/1520-0469(1957)014%3C0184:ACSHSS%3E2.0.CO;2 doi: 10.1175/1520-0469(1957)014⟨0184:ACSHSS⟩2.0.CO;2

Quadfasel, D. (2018). *Physical oceanography during POSEIDON cruise POS503.* PANGAEA. Retrieved from https://doi.org/10.1594/PANGAEA.890699 doi: 10.1594/PANGAEA.890699

Rattan, S., Myers, P. G., Treguier, A.-M., Theetten, S., Biastoch, A., & Böning, C. (2010, jan). Towards an understanding of Labrador Sea salinity drift in eddy-permitting simulations. *Ocean Modelling*, *35*(1-2), 77–88. Retrieved from https://linkinghub.elsevier.com/retrieve/pii/S1463500310001009 doi: 10.1016/j.ocemod.2010.06.007

Riemenschneider, U., & Legg, S. (2007, jan). Regional simulations of the Faroe Bank Channel overflow in a level model. *Ocean Modelling*, *17*(2), 93–122. Retrieved from https://linkinghub.elsevier.com/retrieve/pii/S146350030700011X doi: 10.1016/j.ocemod.2007.01.003

Saunders, P. M. (1996, jan). The Flux of Dense Cold Overflow Water Southeast of Iceland. *Journal of Physical Oceanography*, *26*(1), 85–95. Retrieved from http://journals.ametsoc.org/doi/10.1175/1520-0485(1996)026%3C0085:TFODCO%3E2.0.CO;2 doi: 10.1175/1520-0485(1996)026⟨0085:TFODCO⟩2.0.CO;2

Schoonover, J., Dewar, W., Wienders, N., Gula, J., McWilliams, J. C., Molemaker, M. J., ... Yeager, S. (2016, jan). North Atlantic Barotropic Vorticity Balances in Numerical Models. *Journal of Physical Oceanography*, *46*(1), 289–303. Retrieved from https://journals.ametsoc.org/view/journals/phoc/46/1/jpo-d-15-0133.1.xml doi: 10.1175/JPO-D-15-0133.1

Seim, K. S., Fer, I., & Berntsen, J. (2010, jan). Regional simulations of the Faroe Bank Channel overflow using a σ-coordinate ocean model. *Ocean Modelling*, *35*(1-2), 31–44. Retrieved from https://linkinghub.elsevier.com/retrieve/pii/S1463500310000843 doi: 10.1016/j.ocemod.2010.06.002

Shchepetkin, A. F., & McWilliams, J. C. (2005, jan). The regional oceanic modeling system (ROMS): a split-explicit, free-surface, topography-following-coordinate oceanic model. *Ocean Modelling*, *9*(4), 347–404. doi: 10.1016/j.ocemod.2004.08.002

Song, Y., & Haidvogel, D. (1994, nov). A Semi-implicit Ocean Circulation Model Using a Generalized Topography-Following Coordinate System. *Journal of Computational Physics*, *115*(1), 228–244. doi: 10.1006/jcph.1994.1189

Stacey, M. W., Pond, S., & Nowak, Z. P. (1995, jun). A Numerical Model of the Circulation in Knight Inlet, British Columbia, Canada. *Journal of Physical Oceanography*, *25*(6), 1037–1062. Retrieved from http://journals.ametsoc.org/doi/10.1175/1520-0485(1995)025%3C1037:ANMOTC%3E2.0.CO;2 doi: 10.1175/1520-0485(1995)025⟨1037:ANMOTC⟩2.0.CO;2

Treguier, A. M., Theetten, S., Chassignet, E. P., Penduff, T., Smith, R., Talley, L., … Böning, C. (2005, may). The North Atlantic Subpolar Gyre in Four High-Resolution Models. *Journal of Physical Oceanography*, *35*(5), 757–774. Retrieved from http://journals.ametsoc.org/doi/10.1175/JPO2720.1 doi: 10.1175/JPO2720.1

Wang, H., Legg, S. A., & Hallberg, R. W. (2015, feb). Representations of the Nordic Seas overflows and their large scale climate impact in coupled models. *Ocean Modelling*, *86*, 76–92. Retrieved from https://linkinghub.elsevier.com/retrieve/pii/S1463500314001802 doi: 10.1016/j.ocemod.2014.12.005

Willebrand, J., Barnier, B., Böning, C., Dieterich, C., Killworth, P. D., Le Provost, C., … New, A. L. (2001, jan). Circulation characteristics in three eddy-permitting models of the North Atlantic. *Progress in Oceanography*, *48*(2-3), 123–161. Retrieved from https://linkinghub.elsevier.com/retrieve/pii/S0079661101000039 doi: 10.1016/S0079-6611(01)00003-9

Winton, M., Hallberg, R., & Gnanadesikan, A. (1998, nov). Simulation of Density-Driven Frictional Downslope Flow in Z -Coordinate Ocean Models. *Journal of Physical Oceanography*, *28*(11), 2163–2174. Retrieved from http://journals.ametsoc.org/doi/10.1175/1520-0485(1998)028%3C2163:SODDFD%3E2.0.CO;2 doi: 10.1175/1520-0485(1998)028⟨2163:SODDFD⟩2.0.CO;2

Wise, A., Harle, J., Bruciaferri, D., O'Dea, E., & Polton, J. (2021, dec). The effect of vertical coordinates on the accuracy of a shelf sea model. *Ocean Modelling*, 101935. Retrieved from https://linkinghub.elsevier.com/retrieve/pii/S1463500321001827 doi: 10.1016/j.ocemod.2021.101935

Xu, X., Bower, A., Furey, H., & Chassignet, E. P. (2018, aug). Variability of the IcelandScotland Overflow Water Transport Through the CharlieGibbs Fracture Zone: Results From an Eddying Simulation and Observations. *Journal of Geophysical Research: Oceans*, *123*(8), 5808–5823. Retrieved from https://onlinelibrary.wiley.com/doi/10.1029/2018JC013895 doi: 10.1029/2018JC013895

Xu, X., Schmitz, W. J., Hurlburt, H. E., Hogan, P. J., & Chassignet, E. P. (2010, dec). Transport of Nordic Seas overflow water into and within the Irminger Sea: An eddyresolving simulation and observations. *Journal of Geophysical Research: Oceans*, *115*(C12). Retrieved from https://onlinelibrary.wiley.com/doi/10.1029/2010JC006351 doi: 10.1029/2010JC006351

Supporting Information for "Localised general vertical coordinates for quasi-Eulerian ocean models: the Nordic overflows test-case"

Diego Bruciaferri[1], Catherine Guiavarc'h[1], Helene T. Hewitt[1], James Harle[2],

Mattia Almansi[2] *, Pierre Mathiot[3]

[1]Met Office Hadley Center, Exeter, UK

[2]National Oceanography Centre, Southampton, UK

[3]Universite Grenoble Alpes, Grenoble, France

Contents of this file

1. Figures S1 to S4

Introduction

*now at B-Open, Rome, Italy

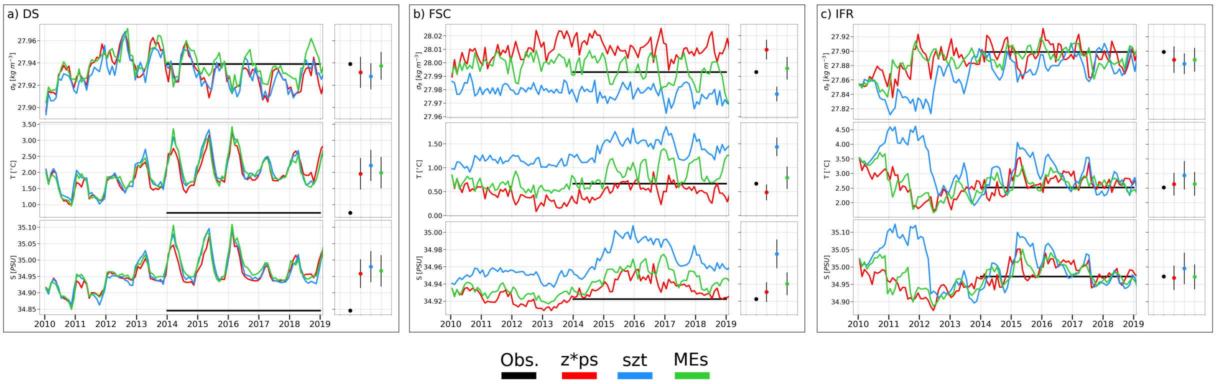

Figure S1. Time-series and mean values of the average potential density anomaly (upper panels), temperature (middle panels) and salinity (bottom panels) of the overflows (water masses with $\sigma_\theta \geq 27.8\ kg\,m^{-3}$) in the Denmark Strait (DS, panel a), Iceland-Faroe-Ridge (IFR, panel b) and Faroe-Bank-Channel (FBC, panel c) cross-sections simulated by the GOSI9-z^*ps (red lines), GOSI9-szt (light blue lines) and GOSI9-MEs (green lines) models against measured (black lines) mean values.

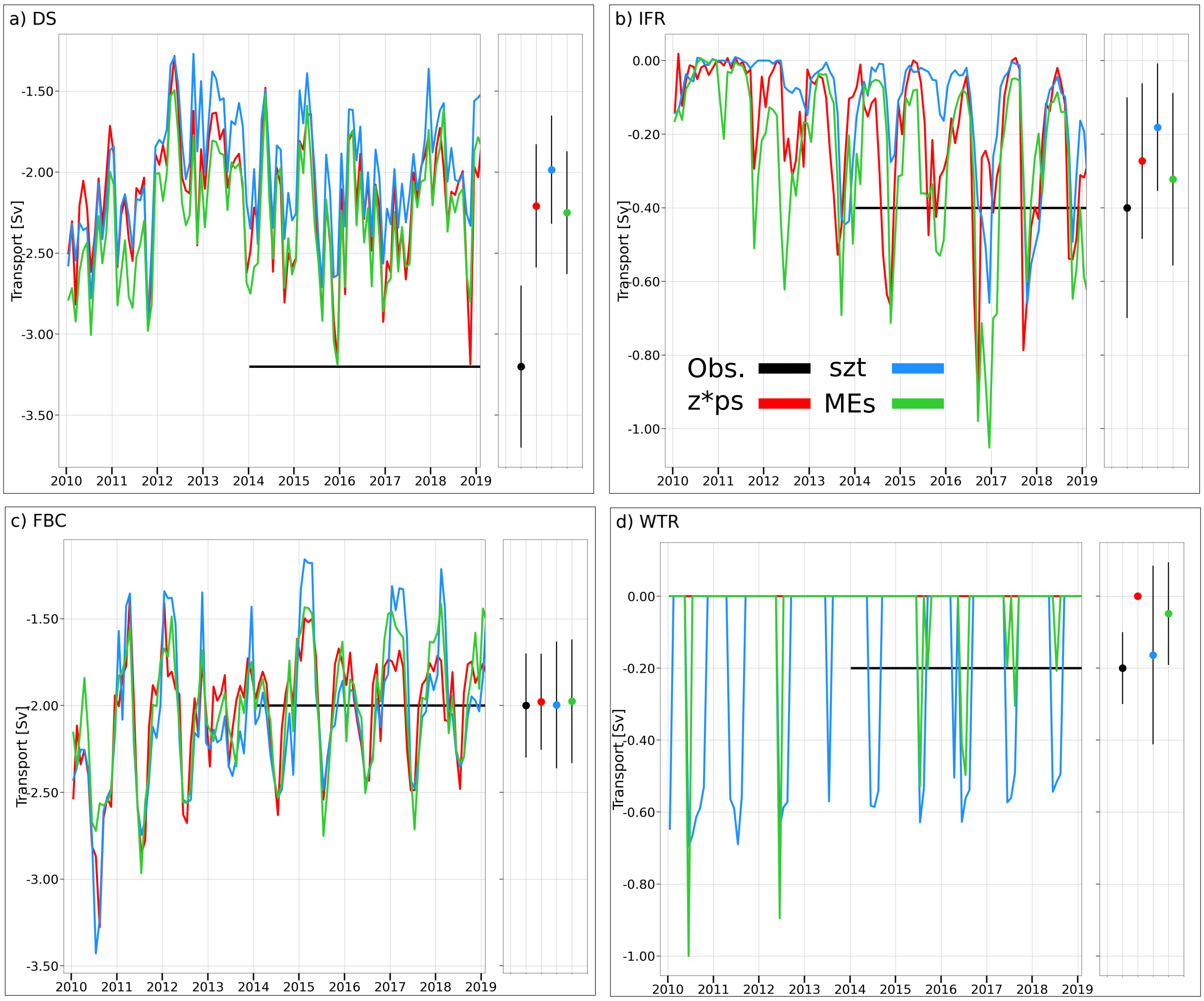

Figure S2. Time-series and mean values of the overflows volume transport (water masses with $\sigma_\theta \geq 27.80\ kg\, m^{-3}$) in the Denmark Strait (DS, panel a), Iceland-Faroe-Ridge (IFR, panel b), Faroe-Bank-Channel (FBC, panel c) and Wyville Thomson Ridge (WTR, panel d) cross-sections simulated by the GOSI9-z^*ps (red lines), GOSI9-szt (light blue lines) and GOSI9-MEs (green lines) models against mean estimates from measurements (black lines).

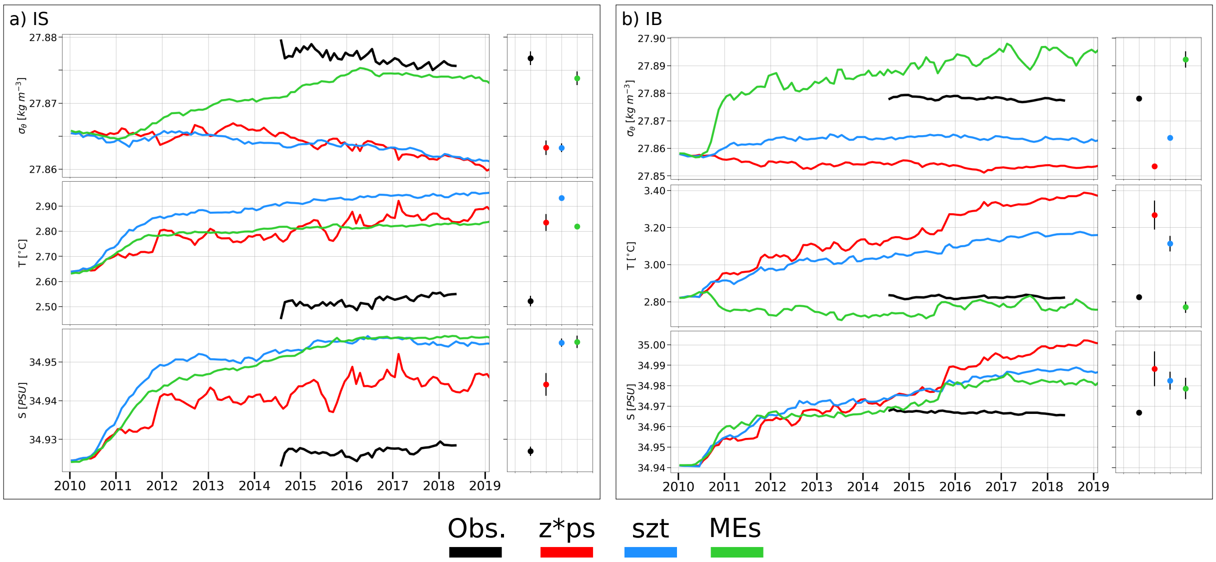

Figure S3. Time-series and mean values of the average potential density anomaly (upper panels), temperature (middle panels) and salinity (bottom panels) of the overflows (water masses with $\sigma_\theta \leq \sigma_\theta^{ovf}$) in the Irminger Sea (IS, panel a) and Icelandic Basin (IB, panel b) cross-sections simulated by the GOSI9-z^*ps (red lines), GOSI9-szt (light blue lines) and GOSI9-MEs (green lines) models against measurements (black lines).

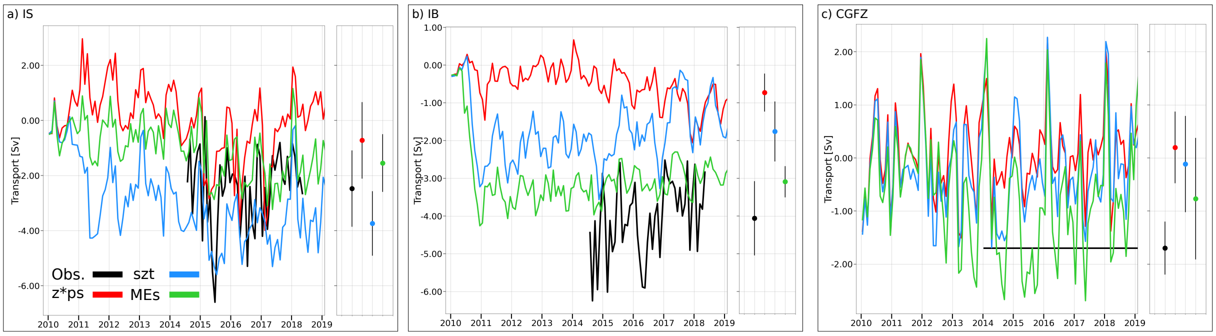

Figure S4. Time-series and mean values of the overflows volume transport (water masses with $\sigma_\theta \geq 27.84\ kg\,m^{-3}$) in the Irminger Sea (IS, panel a) and Icelandic Basin (IB, panel b) legs of the OSNAP East array and in the Charlie-Gibbs Fracture Zone (CGFZ, panel c) cross-section simulated by the GOSI9-z^*ps (red lines), GOSI9-szt (light blue lines) and GOSI9-MEs (green lines) models against measurements (black lines).